

Global Pressure and Temperature Surface Measurements on a NACA 0012 Airfoil in
Oscillatory Compressible Flow at Low Reduced Frequencies

THESIS

Presented in Partial Fulfillment of the Requirements for the Degree Master of Science in
the Graduate School of The Ohio State University

By

Christopher Douglas Jensen

Graduate Program in Aeronautical and Astronautical Engineering

The Ohio State University

2012

Master's Examination Committee:

James W. Gregory, Advisor

Jeffery P. Bons

Report Documentation Page

Form Approved
OMB No. 0704-0188

Public reporting burden for the collection of information is estimated to average 1 hour per response, including the time for reviewing instructions, searching existing data sources, gathering and maintaining the data needed, and completing and reviewing the collection of information. Send comments regarding this burden estimate or any other aspect of this collection of information, including suggestions for reducing this burden, to Washington Headquarters Services, Directorate for Information Operations and Reports, 1215 Jefferson Davis Highway, Suite 1204, Arlington VA 22202-4302. Respondents should be aware that notwithstanding any other provision of law, no person shall be subject to a penalty for failing to comply with a collection of information if it does not display a currently valid OMB control number.

1. REPORT DATE 2012		2. REPORT TYPE		3. DATES COVERED 00-00-2012 to 00-00-2012	
4. TITLE AND SUBTITLE Global Pressure And Temperature Surface Measurements On A NACA 0012 Airfoil In Oscillatory Compressible Flow At Low Reduced Frequencies				5a. CONTRACT NUMBER	
				5b. GRANT NUMBER	
				5c. PROGRAM ELEMENT NUMBER	
6. AUTHOR(S)				5d. PROJECT NUMBER	
				5e. TASK NUMBER	
				5f. WORK UNIT NUMBER	
7. PERFORMING ORGANIZATION NAME(S) AND ADDRESS(ES) The Ohio State University, Enarson Hall 154 12th Ave, Columbus, OH, 43210				8. PERFORMING ORGANIZATION REPORT NUMBER	
9. SPONSORING/MONITORING AGENCY NAME(S) AND ADDRESS(ES)				10. SPONSOR/MONITOR'S ACRONYM(S)	
				11. SPONSOR/MONITOR'S REPORT NUMBER(S)	
12. DISTRIBUTION/AVAILABILITY STATEMENT Approved for public release; distribution unlimited					
13. SUPPLEMENTARY NOTES 1/20					
14. ABSTRACT A co-axial contra-rotating helicopter in forward flight has stall mechanisms that are intrinsically different from those on a traditional helicopter. Traditional helicopters need a cyclic pitch mechanism to balance the rotor lift about each rotation, which leads to dynamic stall from the rapid oscillations in pitch. Co-axial contra-rotating helicopters, which have a fixed pitch about each cycle, encounter a sinusoidal oscillation in Mach number with the mean velocity seen as the rotational velocity while the half amplitude is equal to the forward flight speed. The fluid dynamic mechanism limiting the forward flight speed is entirely different from that of traditional dynamic stall studies. This work sets out to design, create, and study the application of an oscillatory compressible flow field on a NACA 0012 airfoil in order to experimentally model this flow situation.					
15. SUBJECT TERMS					
16. SECURITY CLASSIFICATION OF:			17. LIMITATION OF ABSTRACT Same as Report (SAR)	18. NUMBER OF PAGES 146	19a. NAME OF RESPONSIBLE PERSON
a. REPORT unclassified	b. ABSTRACT unclassified	c. THIS PAGE unclassified			

Copyright by
Christopher Douglas Jensen
2012

Abstract

A co-axial contra-rotating helicopter in forward flight has stall mechanisms that are intrinsically different from those on a traditional helicopter. Traditional helicopters need a cyclic pitch mechanism to balance the rotor lift about each rotation, which leads to dynamic stall from the rapid oscillations in pitch. Co-axial contra-rotating helicopters, which have a fixed pitch about each cycle, encounter a sinusoidal oscillation in Mach number with the mean velocity seen as the rotational velocity while the half amplitude is equal to the forward flight speed. The fluid dynamic mechanism limiting the forward flight speed is entirely different from that of traditional dynamic stall studies. This work sets out to design, create, and study the application of an oscillatory compressible flow field on a NACA 0012 airfoil in order to experimentally model this flow situation. A few different pressure-sensitive paints and imaging techniques were developed for investigation of this oscillatory effect. Ultimately a fast-acting bi-luminophore pressure- and temperature-sensitive paint was chosen for the investigation which uses a polymer-ceramic basecoat and a mixture of luminescent elements. These measurements were made using a two-camera, single-shot, intensity-based pressure-sensitive paint technique. Temperature-corrected pressure measurements were made and accounted for the intrinsic temperature sensitivity of pressure-sensitive paint. This dual-luminophore technique allows for accurate unsteady pressure measurements in a non-uniform and varying

temperature environment; however, due to inadequate unsteady surface pressure tap measurements the pressure results were limited to the steady runs.

This work involved the design and creation of a modification to Ohio State's 6" × 22" Transonic Wind Tunnel to enable oscillations of the freestream Mach number. The test section Mach number in this blowdown facility is dynamically set by varying the choke area downstream of the test section in an oscillatory fashion. The current configuration of the facility can produce Mach number oscillations between 0.44 and 0.64 for a Reynolds number range of 17 – 43 million per meter at oscillation frequencies up to 21 Hz. Unsteady measurements in this oscillating freestream flow have been made on a NACA 0012 airfoil.

Unsteady shock location measurements were made at angles of attack of 9, 10 and 11 degrees and frequencies of 2.1, 9.5, 15.25 and 21 Hz on the NACA 0012 airfoil. Detailed measurements of the shock movement were made with these advanced measurement techniques in order to investigate unsteady effects of the oscillatory freestream flow. Unsteady effects were pronounced for a reduced frequency of 0.037 which is below the typical quasi steady to unsteady threshold of 0.05. Coefficient of pressure measurements for the steady runs were validated with historical data. It was found that the coefficient of lift measurements were in very good agreement, while the coefficient moment had significant errors. Furthermore, the PSP measurements were compared with particle image velocimetry data of other researchers in order to form a comparison of the on- and off-body fluid dynamics at a frequency of 9.5 Hz and angles of attack of 9 and 10 degrees. The single-shot pressure-sensitive paint technique was able to

measure buffeting, which was found to be highly three dimensional over the span of the airfoil. Similar shock location unsteadiness due to buffeting was also measured in the forced oscillation cases at lower Mach numbers than steady runs, causing aperiodic behavior at certain azimuth locations with higher Mach numbers.

Dedication

This document is dedicated to my family and friends.

Acknowledgments

The author would like to take a moment to acknowledge the tremendous support he has received from a variety of sources. My family as a collective has offered unwavering support during my tenure at The Ohio State University. It has truly been a pleasure to work under the advisement and mentorship of James Gregory. Kyle Gompertz who has been my cohort in the development of this unsteady wind tunnel modification, characterization and testing; without whom none of this extraordinary work is possible. Di Peng for his fruitful discussions on PSP, assistance running the tunnel, bi-luminophore PSP development and help painting the various airfoils tested. I would also like to thank Thomas Juliano for his discussions on various testing techniques and assistance editing this paper. Additionally for the support and discussion Jeffery Bons offered on the testing being performed. Thanks goes out to the USAF and ISSI for sponsoring the work performed here at The Ohio State University, including helpful discussions with Steve Palluconi and Jim Crafton. I would also like to acknowledge the support and discourse all of the other researchers at the Aeronautical and Astronautical Research Laboratory have provided over the past four years.

Vita



- 2005.....Diploma, Perrysburg High School
- 2007.....Research Associate, Cornerstone Research
Group, Dayton OH
- 2008-2010Undergraduate Research Associate,
Department of Aeronautical and
Astronautical Engineering, The Ohio State
University
- 2010.....B.S. Aeronautical and Astronautical
Engineering, The Ohio State University
- 2010 to 2011Graduate Teaching Associate, Department
of Mechanical and Aerospace Engineering,
The Ohio State University
- 2010 to 2012Graduate Research Associate, Department
of Mechanical and Aerospace Engineering,
The Ohio State University

Publications

- Jensen, C., Gompertz, K., Peng, D., Gregory, J., and Bons, P.. “Measurement Techniques for Shock Movement Capture on a NACA 0012 in Unsteady Compressible Flow” In: Proceedings of the 42st AIAA Fluid Dynamics Conference and Exhibit. New Orleans, LO. American Institute of Aeronautics and Astronautics. (2012)
- Gompertz, K., Jensen, C., Gregory, J., and Bons, J.. “Compressible Dynamic Stall Mechanisms Due to Airfoil Pitching and Freestream Mach Oscillations” In: Proceedings of the AHS 68th Annual Forum and Technology Display. Fort Worth, TX: American Helicopter Society. (2012)
- Peng, D., Jensen, C., Juliano, T., Gregory, J., Crafton, J., and Palluconi, S.. "Temperature-Compensated Fast Pressure-Sensitive Paint" In: Proceedings of the 50th AIAA Aerospace Sciences Meeting including the New Horizons Forum and Aerospace Exposition. Nashville, TN: American Institute of Aeronautics and Astronautics. (2012)
- Gregory, J., and Jensen, C.. “Smartphone-Based Data Acquisition for an Undergraduate Course on Aircraft Flight Test” In: Proceedings of the 50th AIAA Aerospace Sciences Meeting including the New Horizons Forum and Aerospace Exposition. Nashville, TN: American Institute of Aeronautics and Astronautics. (2012) AIAA-2012-0883

- Gompertz, K., Jensen, C., Kumar, P., Peng, D., Gregory, J., and Bons, J.. "Modification of a Transonic Blowdown Wind Tunnel to Produce Oscillating Freestream Mach Number" AIAA Journal. (2011)
- Juliano, T., Peng, D., Jensen, C., Gregory, J., Liu, T., Montefort, J., Palluconi, S., Crafton, J., and Fonov, S.. "PSP Measurements on an Oscillating NACA 0012 Airfoil in Compressible Flow" In: Proceedings of the 41st AIAA Fluid Dynamics Conference and Exhibit. Honolulu, HI: American Institute of Aeronautics and Astronautics. (2011): AIAA-2011-3728.
- Jensen, C., Gompertz, K., Peng, D., Juliano, T., Kumar, P., Gregory, J., and Bons, J.. "Unsteady Compressible Flow on a NACA 0021 Airfoil." In: Proceedings of the 49th AIAA Aerospace Sciences Meeting including the New Horizons Forum and Aerospace Exposition. Orlando, FL: American Institute of Aeronautics and Astronautics. (2011): AIAA-2011-670.
- Gompertz, K., Kumar, P., Jensen, C., Peng, D., Gregory, J., and Bons, J.. "Modification of a Transonic Blowdown Wind Tunnel to Produce Oscillating Freestream Mach Number." In: Proceedings of the 48th AIAA Aerospace Sciences Meeting. Orlando, FL: American Institute of Aeronautics and Astronautics. (2010): AIAA-2010-1484.

Fields of Study

Major Field: Aeronautical and Astronautical Engineering

Table of Contents

Abstract	ii
Dedication	v
Acknowledgments	vi
Vita	vii
Publications	viii
Fields of Study	ix
List of Tables	xiii
List of Figures	xiv
List of Equations	xx
Nomenclature	xxi
Chapter 1: Introduction	1
Section 1.1: Helicopters in Forward Flight	1
Section 1.2: Fluid Dynamic Background	6
Chapter 2: Freestream Mach Number Oscillation Mechanism Design	10
Section 2.1: Freestream Mach Number Oscillation Introduction	10

Section 2.2: Experimental Facility.....	11
Section 2.3: Sinusoidal Vane Design.....	15
Section 2.4: Freestream Oscillation Mechanism	21
Chapter 3: Unsteady Mach Oscillation Characterization.....	24
Section 3.1: Wind Tunnel Characterization Experimental Setup	24
Section 3.2: Unsteady Tunnel Characterization Results and Discussion	25
Chapter 4: Pressure Sensitive Paint	31
Section 4.1: Pressure Sensitive Paint Introduction	31
Section 4.2: Lifetime- vs. Intensity-Based PSP Techniques	32
Section 4.3: Temperature Compensating Pressure Sensitive Paint	37
Section 4.4: Two Camera vs. Color Camera PSP and TSP Methods	40
Chapter 5: Experimental Setup.....	46
Section 5.1: Experimental Setup Introduction	46
Section 5.2: Pressure and Temperature Sensitive Paint Experimental Setup	47
Section 5.3: Particle Image Velocimetry Experimental Setup.....	50
Chapter 6: Data Processing Techniques	52
Section 6.1: Data Acquisition Board Post-Processing Techniques	52
Section 6.2: Image Registration Techniques	52
Section 6.3: Image Filtering Techniques and Implementation	54

Section 6.4: Pressure and Temperature Calibration.....	60
Section 6.5: Experimental Uncertainty	64
Section 6.6: Shock Location Measurement Techniques.....	65
Chapter 7: Results.....	69
Section 7.1: Static Results.....	69
Section 7.2: Buffeting Results	79
Section 7.3: Dynamic Results.....	82
Chapter 8: Conclusions.....	96
Section 8.1: Summary of Experimental Results	96
Section 8.2: Recommendations for Obtaining Accurate Unsteady Cp Data Using PSP	98
References.....	100
Appendix A: Data Acquisition Post Processing Code.....	105
Appendix B: Image Registration Code.....	109
Appendix C: Averaging Ratio of Red and Green Code.....	114
Appendix D: <i>In situ</i> Calibration and Implementation Code.....	116
Appendix E: Shock Location Capture Code.....	120
Appendix F: Tabulated C_n , C_a , C_l and C_m Data	122

List of Tables

Table 1: R^2 values for the pressure and temperature curve fits for the color and two camera methods.	44
Table 2: Pressure tap locations on the NACA 0012 airfoil	48
Table 3: Unsteady test matrix	82
Table 4: Coefficient of lift, moment and normal force for the steady runs with two standard deviation shown for each PSP measurement.....	122

List of Figures

Figure 1: Schematic diagram of a helicopter in forward flight, illustrating the relative velocity of the rotor blade as a function of its azimuth position.....	2
Figure 2. UH-60 Blackhawk in forward flight ¹	4
Figure 3: Kamov Ka-52 coaxial contra-rotating helicopter ²	5
Figure 4: Sikorsky X2 compound coaxial contra-rotating helicopter ³	5
Figure 5: Schematic diagram of self-sustained shock oscillations ²⁰	8
Figure 6: Schematic diagram of the Aeronautical & Astronautical Research Laboratory 6” × 22” Transonic Wind Tunnel.....	12
Figure 7: Range of test section operating conditions for the 6” × 22” Transonic Wind Tunnel at 280K and a maximum operating pressure of 345kPa.....	14
Figure 8: Experimental ($f = 2.5$ Hz) and theoretical, A^* and Mach number for one period of the flow oscillation with rectangular choked vanes.....	16
Figure 9: Empirical relationship between the test section Mach number and throat area for use in sinusoidal choke vane design.....	18
Figure 10: Vane profile for a Mach Number = $0.105 * \sin(t) + 0.605$	20
Figure 11: Choke vane profile constructed to produce sinusoidal Mach number oscillation	21
Figure 12: Mach oscillation drive train assembly.....	23

Figure 13: Throat Area vs Mach number for sinusoidal, rectangular static and dynamic data as well as Equation 1 and the designed curve fit.....	26
Figure 14: Designed test section Mach number oscillation compared to the test section Mach number, $f=2.5$ Hz ³³	27
Figure 15: One period of normalized hot film data plotted at different frequencies illustrating wave steepening.....	28
Figure 16: (a) Amplitude and (b) Phase Number vs. Mach Number Oscillation Frequency (f) ³³	29
Figure 17: Representative test section Mach number waveforms at different oscillation frequencies ³³	30
Figure 18: Representation of two-gate lifetime PSP measurement technique ³⁷	33
Figure 19: Schematic diagram of the single-shot lifetime-method PSP experimental setup	36
Figure 20: Single-luminophore PSP derived C_p plot (left) and upper surface C_p map (right) for a NACA 0021 under oscillatory flow at $f=2.5$ Hz, $\alpha=10^\circ$, $Re=4.1$ million, and $M=0.61$	39
Figure 21: Comparison of the raw temperature-corrected contours of C_p for the Color Camera, Left, and the Two Camera technique, right, on a NACA 0012 at $f=9.5$ Hz, $\alpha=9^\circ$, $Re=3.9$ million, and $M=0.57$, flow from top to bottom	41
Figure 22: Emission spectra for the color camera technique at A) different pressures and constant temperature and B) different temperatures and constant pressures, with the respective green and red band-pass optical filters shown ⁴⁷	43

Figure 23: Emission spectra for the two-camera technique at A) different pressures and constant temperature and B) different temperatures and constant pressures, with the respective green and red band-pass optical filters shown ⁴⁷	43
Figure 24: Temperature calibration curve for the color-camera method	44
Figure 25: Temperature calibration curve for the two-camera method	45
Figure 26: Diagram of the NACA 0012 airfoil model tested	48
Figure 27: Block diagram of the PSP data acquisition setup, viewing down the longitudinal axis of the wind tunnel.....	50
Figure 28: Representative standard deviation of a wind-off image (axes in pixels), locating the fiducial marker, pressure taps and airfoil edges.....	53
Figure 29: Unfiltered C_p map of the upper surface NACA 0012 at $M = 0.46$, $Re = 3.65 \times 10^6$ and $\alpha = 9^\circ$, flow from left to right	55
Figure 30: Mean top hat filtered, with a radius of 8 pixels, C_p map of the upper surface NACA 0012 at $M = 0.46$, $Re = 3.65 \times 10^6$ and $\alpha = 9^\circ$	56
Figure 31: Wiener top hat filtered, 30 pixels in the span wise and 10 pixels in the chord wise direction, C_p map of the upper surface NACA 0012 at $M = 0.46$, $Re = 3.65 \times 10^6$ and $\alpha = 9^\circ$	57
Figure 32: Median top hat filtered, 30 pixels in the span wise and 10 pixels in the chord wise direction, C_p map of the upper surface NACA 0012 at $M = 0.46$, $Re = 3.65 \times 10^6$ and $\alpha = 9^\circ$	58
Figure 33: C_p profile plot of the unfiltered and three filtering methods of a NACA 0012 at $M=0.46$, $Re=3.65 \times 10^6$ and $\alpha=9^\circ$ at the spanwise location of 350 pixels	59

Figure 34: First 25% x/c C_p profile plot of the unfiltered and three filtering methods of a NACA 0012 at $M=0.46$, $Re=3.65 \times 10^6$ and $\alpha=9^\circ$ at the spanwise location of 350 pixels	60
Figure 35: PSP <i>in situ</i> surface fit calibration for pressure vs. green and red intensity ratios	62
Figure 36: Schematic diagram of bi-luminophore pressure- and temperature-sensitive paint <i>in situ</i> pressure calibration	63
Figure 37: Three C_p profiles from calibrated PSP data of the NACA 0012 airfoil at $M = 0.6$, $\alpha = 9^\circ$ and $Re = 3.8$ million shown with a C_p profile of a NACA 0012 $M = 0.6$, $\alpha = 9^\circ$ and $Re = 3$ million	64
Figure 38: Example upper surface C_p profile and derivative of the C_p with respect to x/c	67
Figure 39: A representative suction surface C_p distributions of a NACA 0012 at $\alpha = 9^\circ$, $M = 0.55$ and $Re = 3.6$ million, flow is from left to right. The black line is where the shock location was searched for	68
Figure 40: Contour of ensemble-averaged Mach number for one phase of a Mach oscillation period with $M = 0.6$, $\alpha = 9^\circ$ and $f = 9.5$ Hz. The black line is where the shock location was searched for ³²	68
Figure 41: Three representative PSP C_p profiles of the NACA 0012 airfoil at $\alpha = 9^\circ$, $M = 0.46$ and $Re = 3.5$ million with pressure taps shown	72
Figure 42: Three representative PSP C_p profiles of the NACA 0012 airfoil at $\alpha = 10^\circ$, $M = 0.45$ and $Re = 3.4$ million with pressure taps shown	72

Figure 43: Three representative PSP C_p profiles of the NACA 0012 airfoil at $\alpha = 11^\circ$, $M = 0.45$ and $Re = 3.4$ million with pressure taps shown.....	73
Figure 44: Three representative PSP C_p profiles of the NACA 0012 airfoil at $\alpha = 9^\circ$, $M = 0.55$ and $Re = 3.7$ million with pressure taps shown	73
Figure 45: Three representative PSP C_p profiles of the NACA 0012 airfoil at $\alpha = 10^\circ$, $M = 0.55$ and $Re = 3.7$ million with pressure taps shown.....	74
Figure 46: Three representative PSP C_p profiles of the NACA 0012 airfoil at $\alpha = 11^\circ$, $M = 0.55$ and $Re = 3.8$ million with pressure taps shown.....	74
Figure 47: Three representative PSP C_p profiles of the NACA 0012 airfoil at $\alpha = 9^\circ$, $M = 0.61$ and $Re = 4.1$ million with pressure taps shown	75
Figure 48: Three representative PSP C_p profiles of the NACA 0012 airfoil at $\alpha = 10^\circ$, $M = 0.61$ and $Re = 4.3$ million with pressure taps shown.....	75
Figure 49: Dark image divided by wind-off, showing the large susceptibility to varying background illumination at the trailing edge	77
Figure 50: Coefficient of lift vs. Mach number for $\alpha = 9, 10$ and 11° , for both PSP and historical data	78
Figure 51: Coefficient of moment vs. Mach number for $\alpha = 9, 10$ and 11° , for both PSP and historical data	79
Figure 52: 9 upper surface C_p maps of the NACA 0012 airfoil at $\alpha = 10^\circ$, $M = 0.61$ and $Re = 4.2$ million for $0\% < x/c < 60\%$ and $20\% < z/b < 80\%$ during a steady run in the buffeting regime.....	81
Figure 53: Mach number vs. Phase for the 4 frequencies at $\alpha = 9^\circ$	84

Figure 54: Mach number vs. Phase for the 4 frequencies at $\alpha = 10^\circ$	84
Figure 55: Mach number vs. Phase for the 4 frequencies at $\alpha = 11^\circ$	85
Figure 56: Mach number vs. Shock Location for the 4 frequencies at $\alpha = 9^\circ$, with hand drawn schematic directional loops of the oscillations starting at $\Psi = 0^\circ$	87
Figure 57: Mach number vs. Shock Location for the 4 frequencies at $\alpha = 10^\circ$	87
Figure 58: Mach number vs. Shock Location for the 4 frequencies at $\alpha = 11^\circ$	88
Figure 59: Shock Location vs. Phase for the 4 frequencies at $\alpha = 9^\circ$	88
Figure 60: Shock Location vs. Phase for the 4 frequencies at $\alpha = 10^\circ$	89
Figure 61: Shock Location vs. Phase for the 4 frequencies at $\alpha = 11^\circ$	89
Figure 62: Four representative phase locked images, $\Psi = 93^\circ$, of PIV and PSP results at 9.5 Hz, $\alpha = 9^\circ$ and $M = 0.59$ showing a steady shock location ⁴⁸	91
Figure 63: Four representative phase locked images, $\Psi = 90^\circ$, of PIV and PSP results at 9.5 Hz, $\alpha = 10^\circ$ and $M = 0.59$ showing an unsteady shock location ⁴⁸	92
Figure 64: Contours of ensemble-averaged Mach number for 12 phases of a Mach oscillation period with $\alpha = 9^\circ$ and $f = 9.5$ Hz ³²	93
Figure 65: Mach number vs. Shock location for PSP, TSP and PIV at $f = 9.5$ Hz and $\alpha = 9^\circ$	94

List of Equations

Equation 1: Mach – area relation	15
Equation 2: Empirical relationship between Mach number and throat area	18
Equation 3: Ideal Mach number oscillation	19
Equation 4: Designed Mach number oscillation	21
Equation 5: Reduced frequency equation	22
Equation 6: Wave propagation speed	27
Equation 7: The luminescent emission response	32
Equation 8: Stern-Volmer equation	32
Equation 9: Shock location equation	66
Equation 10: Coefficient of pressure	70
Equation 11: Normal force coefficient equation.....	70
Equation 12: Axial force coefficient equation	70
Equation 13: Sectional coefficient of lift equation	70
Equation 14: Sectional coefficient of drag equation.....	70
Equation 15: Sectional coefficient of moment equation about the quarter chord.....	71

Nomenclature

A	= Stern-Volmer coefficient	C_m	= sectional moment coefficient (Equation 15)
A_t	= test section area (m ²)	C_p	= coefficient of pressure (Equation 10)
A^*	= choke area (m ²)	f	= oscillation frequency (Hz)
B	= Stern-Volmer coefficient (Equation 6)	G	= green band-pass filtered camera channel
b	= airfoil span (m)	$G1$	= gate 1 of the camera shutter
C	= wave propagation speed (Equation 6)	$G2$	= gate 2 of the camera shutter
c	= airfoil chord (m)	I	= intensity
C_a	= sectional axial force coefficient (Equation 12)	k	= reduced frequency (Equation 5)
CCD	= charge-coupled device	L	= luminescence
C_d	= sectional coefficient of drag (Equation 14)	M	= Mach number
C_n	= sectional normal force coefficient (Equation 11)	P	= pressure
C_l	= sectional lift coefficient (Equation 13)	PIV	= particle image velocimetry
		PSP	= pressure sensitive paint
		R	= red band-pass filtered camera channel

Re = Reynolds number based on
airfoil chord

RGB = red green blue

SNR = signal to noise ratio

t = time (seconds)

T = temperature (K)

T' = period of oscillation

TSP = temperature sensitive paint

x = streamwise direction (m)

y = wall normal direction (m)

z = spanwise direction (m)

α = angle of attack ($^{\circ}$)

γ = ratio of specific heats

τ = luminescent lifetime

ϕ = phase angle (rad)

Ψ = rotor azimuth ($^{\circ}$)

θ = Phase (rad)

Subscripts

o = total

ref = reference or wind off condition

l = lower surface

s = static

M = Mach number

u = upper surface

Chapter 1: Introduction

Section 1.1: Helicopters in Forward Flight

When a traditional helicopter is in forward flight the rotor blade experiences a difference in relative velocities between the advancing and retreating blades, as illustrated in Figure 1. Therefore, a cyclic rotor pitch adjustment is imposed to balance the lift distribution about the rotor azimuth (Ψ), such that the angle of attack is low on the advancing blade and high on the retreating blade. Traditional helicopters are limited in their forward flight speed by dynamic stall or shock-induced stall. Dynamic stall is caused by the rapidly changing angle of attack (α) between the advancing and retreating rotor blades from the need to balance the lift distribution. During high-speed flight, maneuver, and at high altitude, this rapid pitching motion to post stall angles of attack and oscillatory relative flow field causes dynamic stall. Figure 2 illustrates a traditional UH-60 Blackhawk helicopter in forward flight.

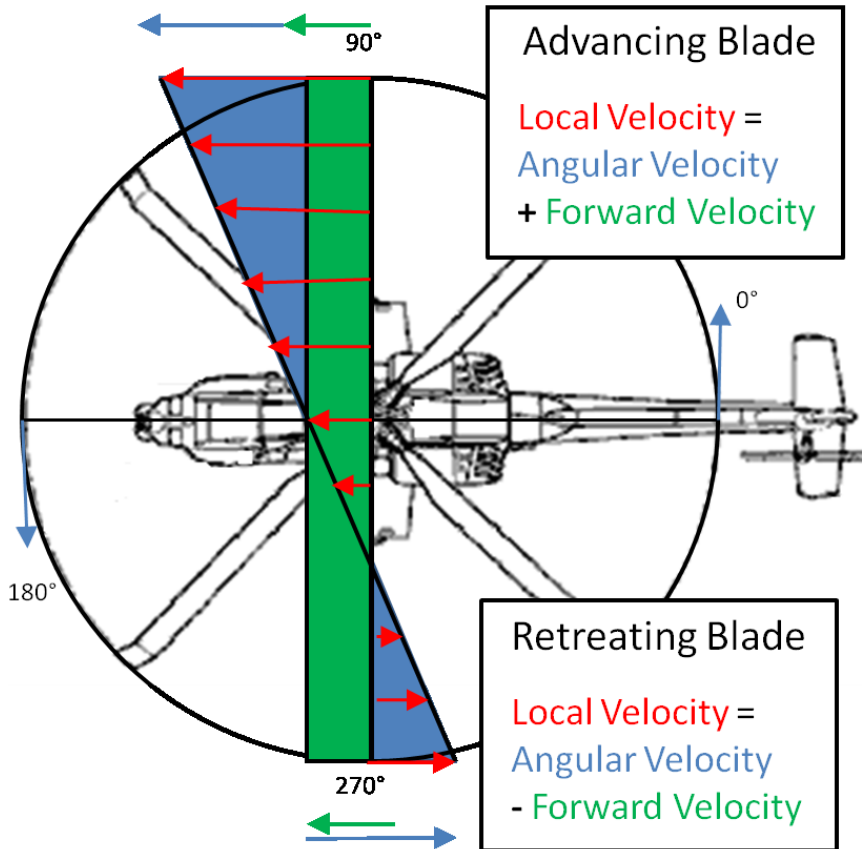


Figure 1: Schematic diagram of a helicopter in forward flight, illustrating the relative velocity of the rotor blade as a function of its azimuth position

Due to this dynamic stall limitation, non-traditional helicopter configurations have arisen from the need to fly faster or more efficiently. One method to avoid the asymmetry of lift is the use of contra-rotating blades; examples include the Kamov Ka-52, and more recently the Sikorsky X2, as seen in Figure 3 and Figure 4 respectively. With these contra-rotating configurations it is no longer necessary to have a tail rotor. Additionally, cyclic pitch mechanisms are not necessary to balance the aircraft's lift about the rotor azimuth for co-axial helicopters. Therefore, the rotor angle of attack is fixed throughout its revolution.

The only phenomena limiting the forward flight speed of coaxial contra-rotating helicopters are shock-induced stall, power available, vibratory loading and the aerodynamic drag performance of the helicopter. In order to engineer rotor designs that expand the operating envelope of these rotorcraft, it is imperative to investigate the flow mechanisms that lead to shock-induced stall on an airfoil subject to a time-varying compressibility condition. This leads to a need for advanced measurement techniques which have the ability to track the motion of standing shock waves with greater resolution than traditional pressure taps. In particular, there is a limited amount of knowledge about the impact of unsteady oscillatory compressible flow effects on shock-induced stall that is typical of contra-rotating helicopter operations in maneuver or high-speed forward flight.



Figure 2. UH-60 Blackhawk in forward flight¹



Figure 3: Kamov Ka-52 coaxial contra-rotating helicopter²



Figure 4: Sikorsky X2 compound coaxial contra-rotating helicopter³

Section 1.2: Fluid Dynamic Background

Numerous investigations have focused on the mechanisms of dynamic stall, for example McCroskey et al., McAlister et al. and Tijdeman and Seebass;⁴⁻⁸ Typically these studies have been performed in the low-speed, incompressible regime ($M < 0.1$).⁹⁻¹¹ These investigations have focused on the leading-edge vortex that is shed from the airfoil which leads to lift and moment dynamic stall, while employing mechanisms that vary either airfoil pitch or freestream velocity. Saxena utilized hot wires, surface pressure measurements and surface hot film gages along with silk tufts to conduct a comprehensive on- and off-body study of a NACA 0012 airfoil in an oscillating airstream.¹² These measurement techniques were used to investigate relatively high reduced frequencies (k^*) of 0.18 to 0.9 and a chord Reynolds number of 250,000. The thrust of the investigation was on the effects of angle of attack on the steadiness of the flow field, concluding that the flow was quasi steady above and below the critical (or stall) angle of attack. However it was found that near the onset of stall the airfoil was more prone to perturbances and oscillated between stalled and attached flow over the airfoil with the flow oscillation. At angles below the static stall angle, trip strips had no effect on the outcome and it was concluded that Reynolds number and transition effects had no effect on the flow phenomenon.

Selerowicz, Szumowski and Meier in two separate studies investigated forced background flow oscillations, $0.65 < M < 0.75$, at the buffeting frequency and angle of attack of a NACA 0012 airfoil using interferometry and pressure taps.^{13, 14} However, with

only 14 Kulite pressure transducers installed on the upper surface of the airfoil, their ability to capture shock location was intrinsically limited in resolution. The interferometry technique in their study was utilized to study the separation location for different oscillation frequencies, but was not applied to the shock location.

Fernie, Babinsky and Bruce conducted numerous investigations into the effects of unsteady freestream oscillations on the dynamic shock structure on a NACA0012 airfoil at low angles of attack.¹⁵⁻¹⁹ When operated at transonic speeds and moderately high frequencies (of the order of 50 Hz), they found that there were differences in the shock strength and speed, depending on whether the freestream Mach number was increasing or decreasing. Evidently, a decelerating freestream caused a stronger shock to move forward on the airfoil surface more rapidly than an accelerating freestream over the same change in Mach number. Fernie and Babinsky's work utilized Kulite pressure transducers and high speed spark Schlieren images to study this fluid dynamic phenomenon. However misalignments in the tunnel sidewalls and or camera setup would cause differences between tunnel runs at the same operating conditions. Therefore the pressure taps data at every 5% of the chord (c) were utilized for quantitative results resulting in error bars of $\pm 2.5\% x/c$.

At a certain regime of steady Mach numbers and angles of attack, airfoils encounter a self induced phenomenon known as buffeting where the standing shock wave undergoes oscillations in the chordwise direction of the airfoil, as seen in a schematic diagram from Lee, Figure 5.²⁰ Buffeting has been described by Crouch et al. as large scale oscillations that can limit the flight envelope of aircraft due to fluid-structure interactions and are encountered by a global instability in the flow field that is self

sustaining.²¹ The fluctuations in coefficient of pressure (C_p) have been measured on the order of 0.5 due to the fluctuation in the shock location over the given pressure tap with an oscillation period of ~ 14 ms.²⁰

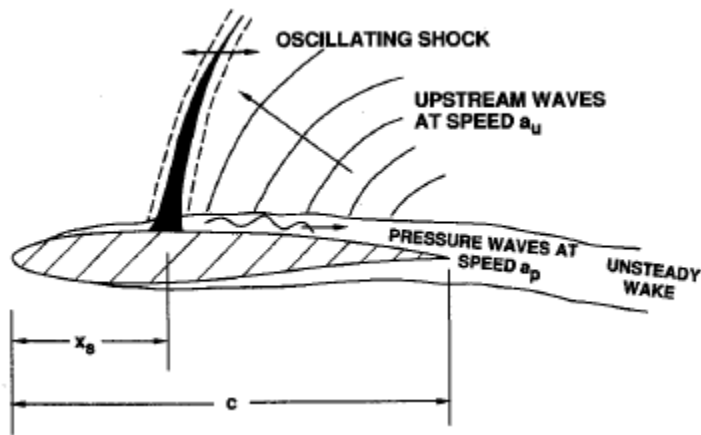


Figure 5: Schematic diagram of self-sustained shock oscillations²⁰

In order to develop a full, accurate understanding of this dynamic stall phenomenon, the problem must be investigated with precise high speed instrumentation in conditions that adequately model the time-varying compressibility effects. The purpose of this investigation is to experimentally model unsteady compressible flow and study the complex compressibility effects on shock movement at low reduced frequencies, compressible Mach numbers, and high Reynolds numbers.

Wind tunnel testing and computational fluid dynamics (CFD) have both become integral tools in the design, testing, and evaluation of airfoils. Static, or time-invariant, tests are ordinarily conducted, which has become commonplace in the aerodynamic community. Static testing is significantly easier to model than dynamic testing and

requires substantially less computational time for CFD. However with the advancement in computational power, high fidelity CFD models and wind tunnel measurement techniques alike are now possible. These methods can be applied to perform comprehensive unsteady testing and evaluation of airfoils. The most productive approach is one that combines experimental and numerical modeling.²² Therefore, despite the scarcity of high-Reynolds number, compressible, dynamic wind tunnels, such facilities are necessary to completely understand the relevant flow physics and validate the CFD modeling. For these reasons The Ohio State University upgraded the 6" x 22" Transonic Wind Tunnel to create unsteady compressible flow field as discussed in Chapter 2.

Chapter 2: Freestream Mach Number Oscillation Mechanism Design

Section 2.1: Freestream Mach Number Oscillation Introduction

A freestream oscillation mechanism is required to create an unsteady flow field for testing. There has been some fundamental work in this area of research in the incompressible regime. Shih and Ho used a low speed unsteady water tunnel to investigate the evolving vorticity field about an NACA 0012 at the incompressible static stall angle ($\alpha = 12^\circ$) in an unsteady sinusoidal freestream flow.²³ They were able to see an increase in lift that was co-located with a vortex being shed from the airfoil surface using two axis load cells and flow visualization. They utilized a vertical mounted water tunnel whose freestream speed was precisely controlled by attaching a stepper motor to a flow control gate downstream of the test section. In this manner different velocity profiles were achieved such as saw-tooth and sinusoidal waveforms. Saxena performed similar low speed oscillating flow experiments on a NACA 0012.¹² This experimental setup at Illinois Institute of Technology oscillated a set of 4 flat plates at the aft end of the 3-30 m/s wind tunnel to create the required flow conditions. Favier et al. created a more unusual mechanism by oscillating the airfoil in the streamwise direction and additionally in pitch.⁹ Other methods for oscillating the freestream flow include the use of a splitter plate, rotating the blockage flow downstream or upstream of the test section and

oscillating the model relative to the freestream.²⁴ However the majority of compressible flow facilities utilize one or more vanes rotated downstream of the test section.^{13-15, 25, 26} The 6" × 22" Transonic Wind Tunnel has recently been modified to enable freestream Mach oscillations in order to simulate compressible dynamic stall.

Section 2.2: Experimental Facility

Ohio State's 6" × 22" Transonic Wind Tunnel was designed specifically for the testing of airfoils. Starting in 1976 the 6" × 22" Transonic Wind Tunnel was utilized as the prime facility for The General Aviation Airfoil Design and Analysis Service. During this period of time a plethora of airfoils were tested and developed at The Ohio State University for the aeronautical community, see Figure 6.^{27, 28}

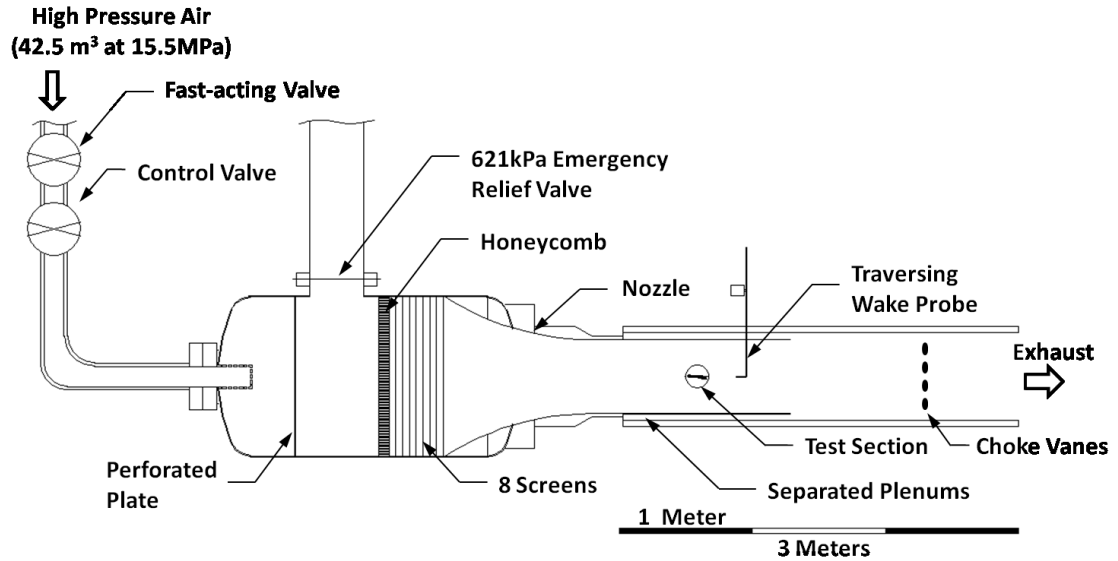


Figure 6: Schematic diagram of the Aeronautical & Astronautical Research Laboratory 6'' × 22'' Transonic Wind Tunnel

The wind tunnel was designed as a low-turbulence facility with the primary goal of matching freestream flight conditions. To accomplish this objective, the settling chamber is equipped with a perforated plate, honeycomb section and then five screens of 60 mesh to lower the turbulence to acceptable levels, less than 0.5% under steady flow conditions.²⁹ A subsonic nozzle with a contraction ratio of 15:1 provides excellent flow uniformity in the 1.1 m long, 6'' × 22'' test section. The 56 cm (22 in.) high solid sidewalls hold the airfoil. The 15 cm (6 in.) spanwise floor and ceiling walls are perforated with 3.2 mm-diameter straight holes, yielding an effective porosity of 6 percent.³⁰ These isolation cavities or plenums are open to the flow only at the downstream end of the test section and aid in producing a high-quality flow in the test section by reducing Mach wave reflections in transonic flow.

The tunnel is fed by two 21.25 m³ tanks pressurized up to 15.5 MPa with conventional air dryers used to maintain gas purity with a dew point of -40°C. The high pressure air is controlled by two valves. The first is a control valve which sets the total pressure and Reynolds number. The second is a fast-acting valve used to start and stop the flow. Mach number is controlled independently of Reynolds number by adjusting the throat area downstream of the test section. The Mach number is uniquely set by the throat area, independent of stagnation pressure, as long as choked flow is maintained. The minimum Reynolds number, at a given Mach number, is set by the stagnation pressure needed to choke the flow while the maximum is set by a structural pressure limitation of the tunnel. These two parameters (Re and M) can be independently varied over a considerable range, as shown in Figure 7. The run duration is typically 10 seconds with 15 minutes between runs, however run durations up to 45 seconds are possible in this blowdown facility.

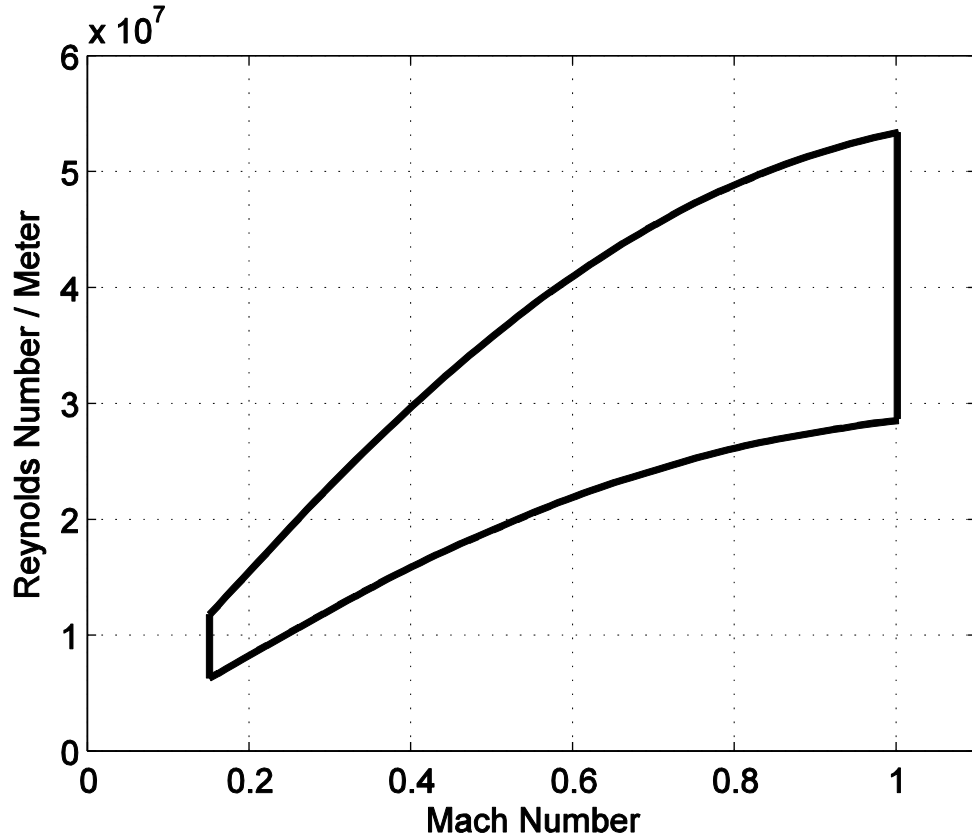


Figure 7: Range of test section operating conditions for the 6'' × 22'' Transonic Wind Tunnel at 280K and a maximum operating pressure of 345kPa

The Mach number in the test section is determined by the Mach – area equation seen in Equation 1. Where A^* is the cross sectional area at the choke point and A_t is the cross sectional area in the test section. Similar to other wind tunnel facilities as discussed in Section 2.1, the freestream Mach oscillation was created by varying the throat area downstream of the test section periodically.

Equation 1: Mach – area relation

$$\frac{A^*}{A_t} = M \left[\left(\frac{2}{\gamma + 1} \right) \left(1 + \frac{\gamma - 1}{2} M^2 \right) \right]^{\frac{\gamma + 1}{2(1 - \gamma)}}$$

Section 2.3: Sinusoidal Vane Design

A rectangular vane set was initially implemented in the wind tunnel.²⁹ Even though the resulting Mach number variation was expected to contain higher harmonics, this geometry was selected for ease of manufacturing and implementation. The results from the rectangular vanes were analyzed to aid in the design of new sinusoidal Mach number oscillation vanes. Each of the four rectangular vanes had a length of 6.35 cm and a width of 3.81 cm. The rectangular vane set was implemented in the tunnel down-stream of the test section as seen in Figure 6 labeled “choke vanes.” The tunnel was then run at a modest Mach oscillation frequency (f) of 2.5 Hz. The total (p_o) and static pressures (p_s) were measured in the test section in order to characterize the resulting Mach oscillation. Figure 8 shows the measured and theoretical test section Mach number as derived from Equation 1, using the Mach - area relation. Similarly, the actual throat area (A^*) is calculated by solving Equation 1 with the experimentally-measured test section Mach number and test section area.

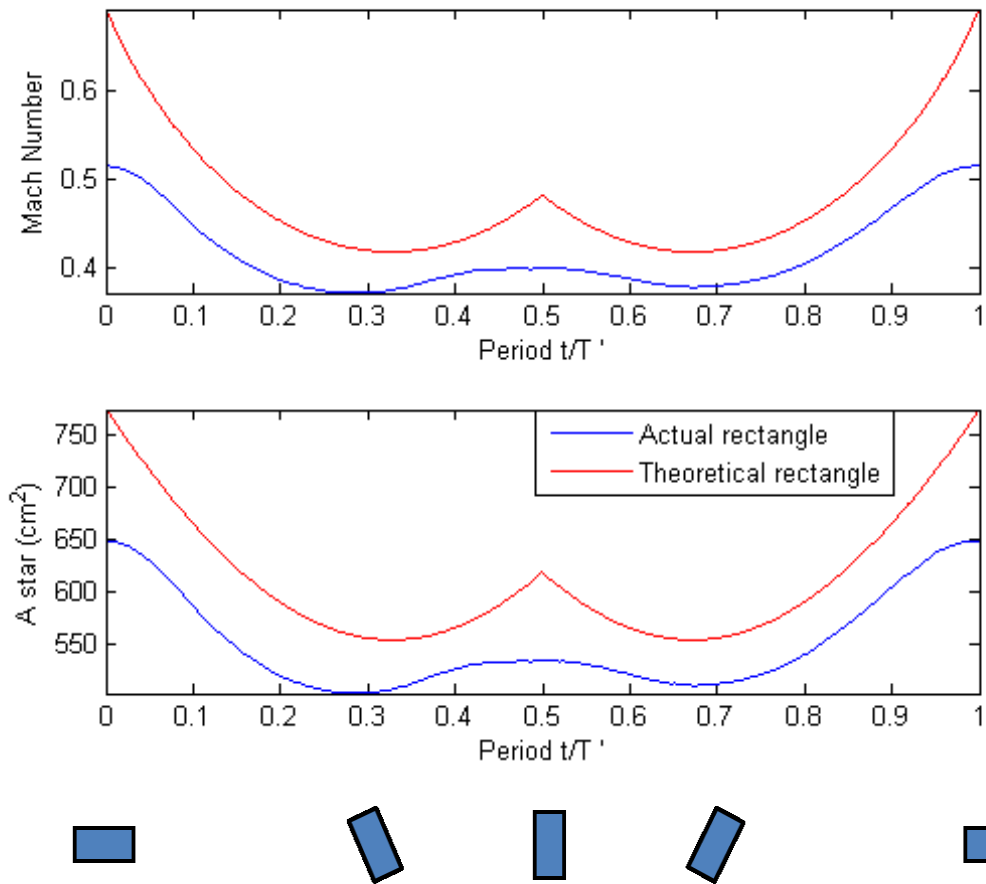


Figure 8: Experimental ($f = 2.5$ Hz) and theoretical, A^* and Mach number for one period of the flow oscillation with rectangular choked vanes

Figure 8 illustrates that the measured Mach number follows the general trend anticipated from the Mach - area relation (Equation 1), but with rounding of sharp corners in the waveform. This attenuation of higher frequencies is due to the low-pass filter characteristics of the wind tunnel, which are discussed in more detail in Section 3.2. The difference between the measured and theoretical Mach number results is largest when the axes of the rectangular vanes are parallel with the wind tunnel axis (0 and 90 degrees). As the boundary layer increases along the walls of the tunnel the displacement

thickness is found in order to calculate the effective cross sectional area at the test section and throat location. The throat area has a larger displacement thickness due to the throat location being downstream of the test section, the effective area ratio, A^*/A_t , is reduced giving a proportionally lower Mach number as seen in Equation 1. The actual, or experimentally measured, Mach number is lower from the theoretical values due to these viscous effects, as the boundary layer along the tunnel walls grow from the test section to the throat.

Due to difficult to account for boundary layer and viscous effects in the tunnel and on the Mach oscillation vanes, an empirical relationship between M and A^* was defined. The viscous effects that cause deviation between theory and experiment are difficult to measure; thus, an empirical relationship between Mach number and vane area is used for subsequent vane designs. Figure 9 shows the rectangular choke vane static results obtained with the vanes rigidly fixed in the 0 and 90 degree orientations. Results from the dynamic oscillation (Figure 8) are also indicated in Figure 9, after low-pass filtering to remove the higher harmonics. The static results correlate well to the dynamic $f = 2.5$ Hz data. A second order polynomial fit (see Equation 2) was applied to the experimental data of Figure 9 to determine the empirical relationship between the test section Mach number and throat area. In addition to the data points plotted, $M = 0$ and 1 were also constrained as full and zero blockage area, respectively.

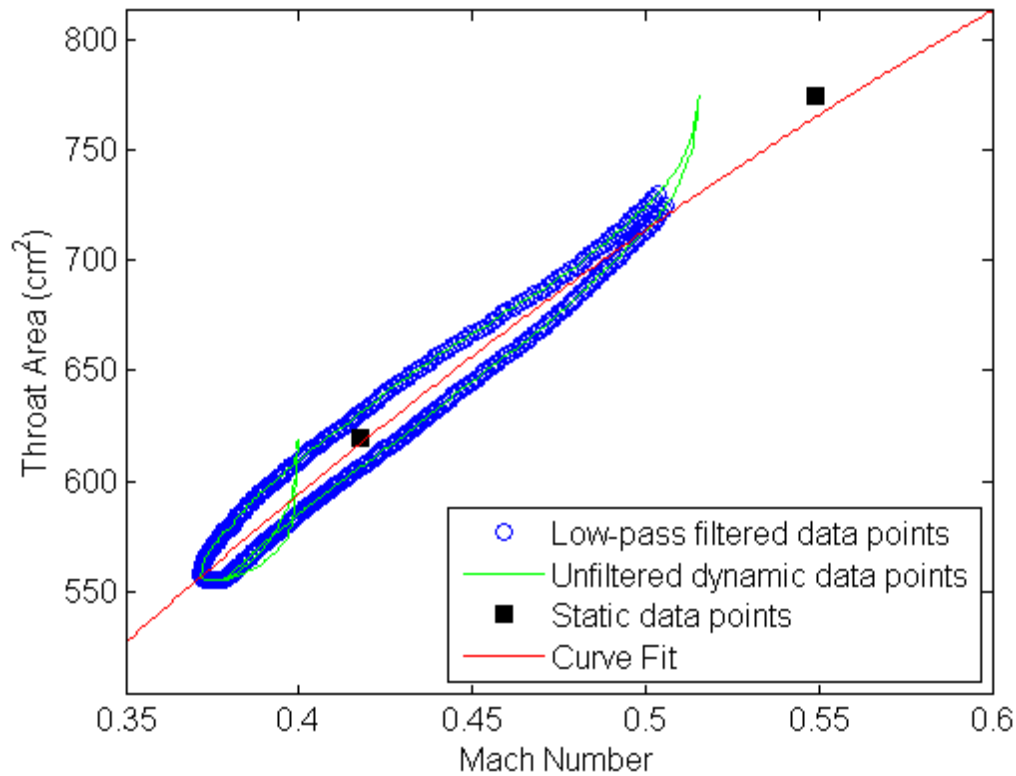


Figure 9: Empirical relationship between the test section Mach number and throat area for use in sinusoidal choke vane design

Equation 2: Empirical relationship between Mach number and throat area.

$$A^* = -11.35 M^2 + 41.65 M + 0.4907$$

This empirical relationship was then used to design an elliptical vane set that would produce a sinusoidal oscillation in Mach number. The vanes are designed with a symmetric profile in order to avoid eccentric loading; therefore, two periods of the Mach waveform are created for each complete rotation of the vanes. The vane radius was designed using the empirical relationship between the test section Mach number and the

throat area defined in Equation 2 and the following equation for the desired Mach number:

Equation 3: Ideal Mach number oscillation.

$$M(t) = 0.105 * \sin(t) + 0.605$$

The resulting choke vane design for this Mach wave is shown in Figure 10. The resulting design turned out to be much too aggressive and vanes ended up peanut shaped because the amplitude of the sine wave was too steep. Obviously the minimum area is not fluid dynamically possible to obtain using this area ratio Mach curve. The mean Mach number and amplitude were reduced in order to more closely resemble that of the rectangular vanes. This allowed for a feasible vane shape using the A^* - Mach curve fit, as well as higher confidence in the curve fit due to the similar Mach number range of the elliptical and rectangular vane set. Figure 9 shows the Mach number and A^* for one rotation of the designed vanes.

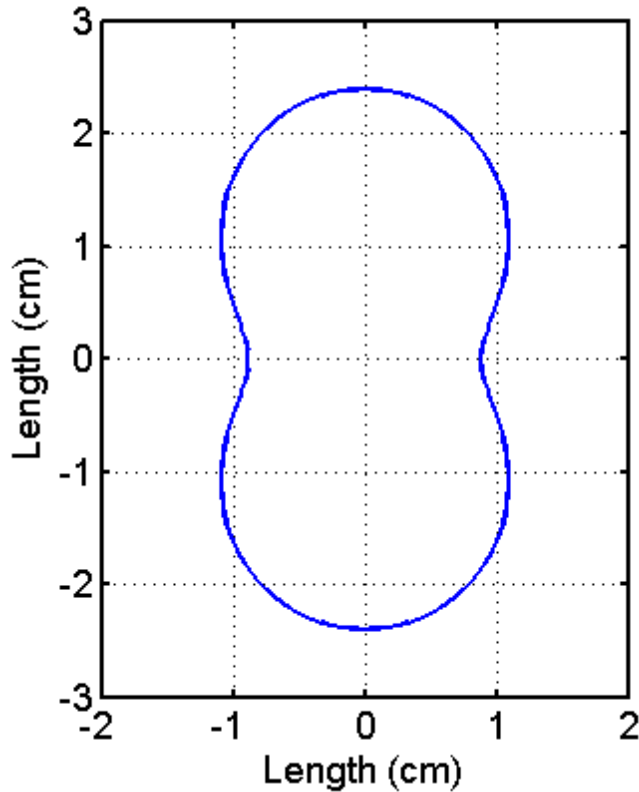


Figure 10: Vane profile for a Mach Number = $0.105 * \sin(t) + 0.605$

The Mach oscillation was redesigned based on the new Mach number oscillation seen in Equation 4. The A^* is again found from inputting this Mach number equation into the A^* - Mach polynomial curve fit. The necessary blockage area to obtain A^* is divided between the four vanes and wrapped around the axis of rotation. This results in the constructed and tested vane geometry of Figure 11. The set of vanes were manufactured to a tolerance of 0.127 mm and installed in the wind tunnel for the current investigation.

Equation 4: Designed Mach number oscillation.

$$M(t) = 0.063 * \sin(t) + 0.45$$

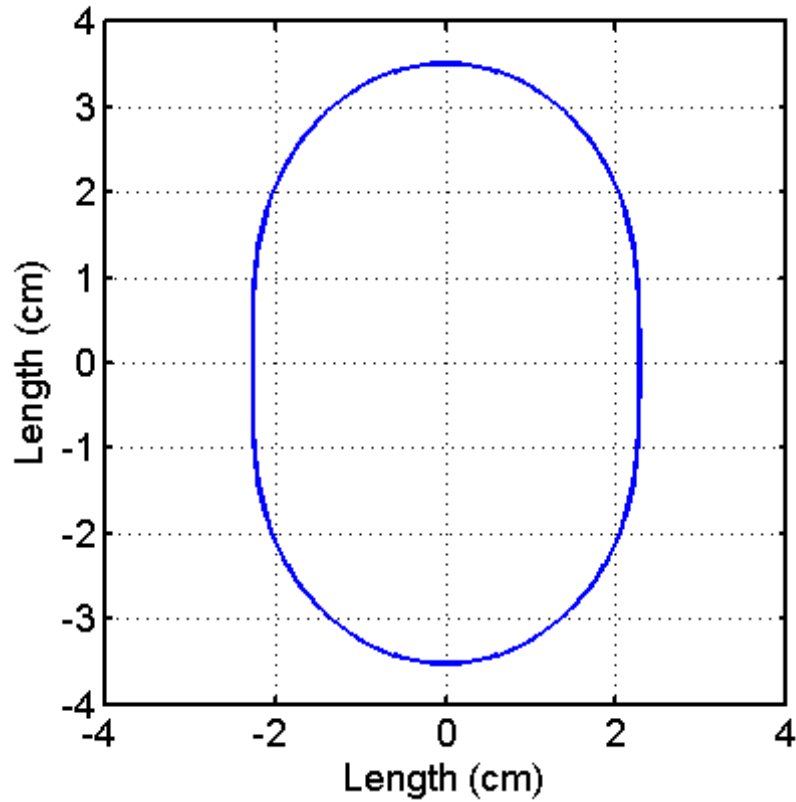


Figure 11: Choke vane profile constructed to produce sinusoidal Mach number oscillation

Section 2.4: Freestream Oscillation Mechanism

The transonic wind tunnel has been modified to oscillate the flow using a variable-area throat downstream of the test section. The throat location can be seen in

Figure 6, labeled as the choke vanes. The choke vanes are connected to a 5-HP variable frequency A/C motor through a drive mechanism (Figure 12). This drive mechanism consists of a sprocket mounted to each vane with a chain linking them to the motor. The choke vanes are counter rotating to minimize harsh unsteady vertical loading on the tunnel. An optical encoder is mounted to one vane shaft in order to record the rotational frequency of the choke vanes. This includes a 500 per revolution and a once per revolution signal which is necessary to calculate the phase, compare waveforms, and produce a triggering mechanism for the particle image velocimetry, pressure- and temperature-sensitive paint experimental setups. In the current geared configuration, the A/C motor can produce flow oscillatory frequencies up to 21 Hz. This oscillatory frequency is important in its relation to the reduced frequency (k), as seen in Equation 5. For $f = 21$ Hz, $M = 0.52$ and $c = 0.127$ m, $k = 0.05$, which is traditionally defined as the end of quasi steady and beginning of unsteady flow.³¹

Equation 5: Reduced frequency equation.

$$k = \frac{fc}{2V}$$

Optical Encoder

5 HP Variable
Frequency A/C
Motor

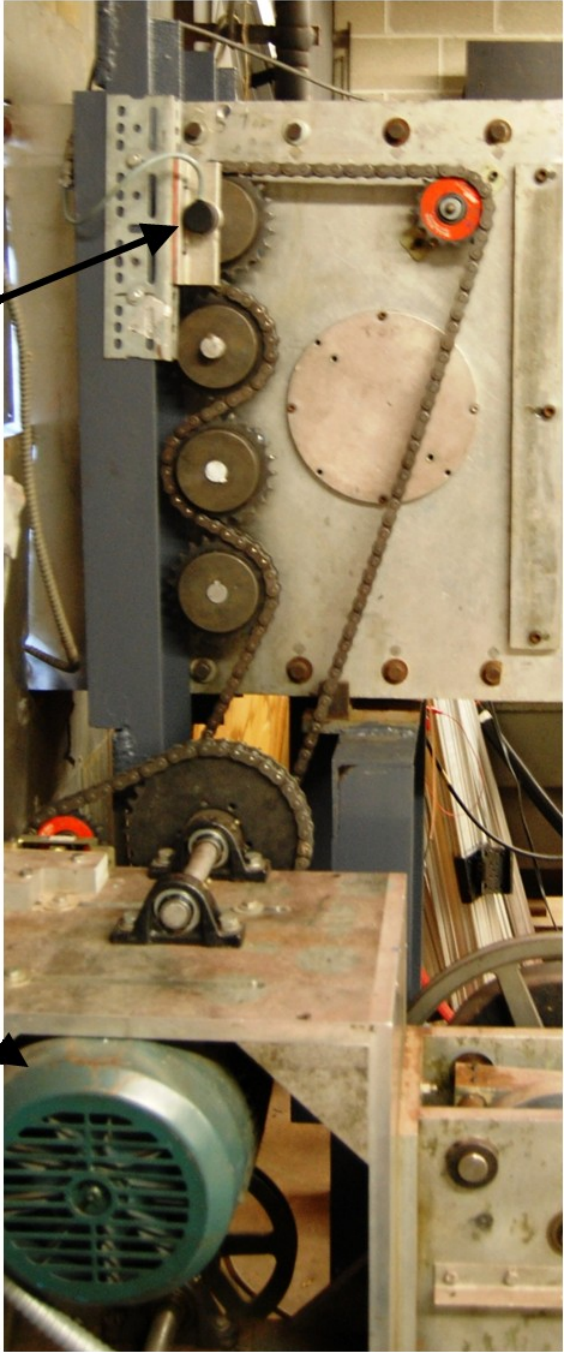


Figure 12: Mach oscillation drive train assembly

Chapter 3: Unsteady Mach Oscillation Characterization

Section 3.1: Wind Tunnel Characterization Experimental Setup

A TSI model 1231-60W hot film was the main measurement instrument used for the initial characterization tests. The hot film was used to investigate the effects of changing Mach oscillation frequencies on the waveform shape and phase shift. The hot film is surface mounted on a conical probe which is centered in the test section. A thin platinum film strip of 0.127 mm width is wrapped around the conical probe tip, and the tip is aligned to point upstream. The hot-film signal was sampled at 2 kHz and low-pass filtered at 1 kHz to attenuate noise and prevent aliasing.

Measurements were made of the magnitude and phase relationship of the oscillating flow through the wind tunnel at unsteady Mach numbers ranging between $0.44 < M < 0.65$ and at various Mach number oscillation frequencies (f) up to 21 Hz. During a 30-second run, the total temperature, T_o , typically decreases 15 K, corresponding to a 7.5 m/s decrease in the speed of sound (a). Due to large tubing effects on the pressure tap lines and low sampling frequencies of the pressure transducers used in this initial setup, the maximum oscillation frequency used was 2.1 Hz. These low frequency Mach oscillation data from pressure transducers were utilized to perform an *in situ* calibration of the hot film by throttling back the oscillation frequency to 2.1 Hz at the beginning and

end of each run. The combined uncertainty in measured Mach number is ± 0.005 at a nominal Mach number of 0.51.³²

Section 3.2: Unsteady Tunnel Characterization Results and Discussion

The sinusoidal vanes for the geometry seen in Figure 11 were manufactured to a geometrical tolerance of 0.127 mm and installed in the wind tunnel. A series of wind tunnel runs were completed to analyze their performance. During characterization the vanes were oscillated at frequencies ranging from 2.5 to 21 Hz. The sinusoidal choke vanes were found to produce a periodic Mach oscillation from 0.44 to 0.64 with no airfoil in the test section. The maximum Mach number was shifted up from the designed Equation 4 value by $\Delta M = 0.127$ and the minimum by $\Delta M = 0.053$. The sinusoidal data is seen to be closer to that of the $A^*/A (M)$ equation, Equation 1, in Figure 13. The Mach oscillation waveform is seen (Figure 14) to be bottom heavy due to the difference between the instantaneous angular radius and the maximum thickness for the given angular position. The Mach number also had a bulk shift of the mean Mach number from this instantaneous angular radius mean $M=0.54$ to the experimentally measured $M=0.515$, as seen by the horizontal lines in Figure 14. Therefore the 1-D analytical Mach number accounts for the majority of these discrepancies in instantaneous cross sectional area by including area changes due to boundary layer thickness at the test section and choke area, as discussed by Gompertz et al.³³ The experimentally measured Mach number is still lower than the 1-D analytical solution, effectively stating that the throat area of the tunnel

is smaller than predicted. It is postulated that this added throat blockage area is due to unsteady wakes of the rotating vanes or non-uniform boundary layer growth on the vanes. Figure 14 shows that the rectangular vanes experienced additional blockage possible due to larger wakes shedding from the discontinuous rectangular vanes. The experimentally measured Mach oscillation waveform is also slightly bottom heavy, with the $f = 2.5$ Hz mean Mach number 4.5% lower than the peak to peak median. Figure 14 shows both the 1-D analytical designed Mach oscillation as well as the Mach wave achieved in the test section for the sinusoidal vane set at a frequency of 2.5 Hz.

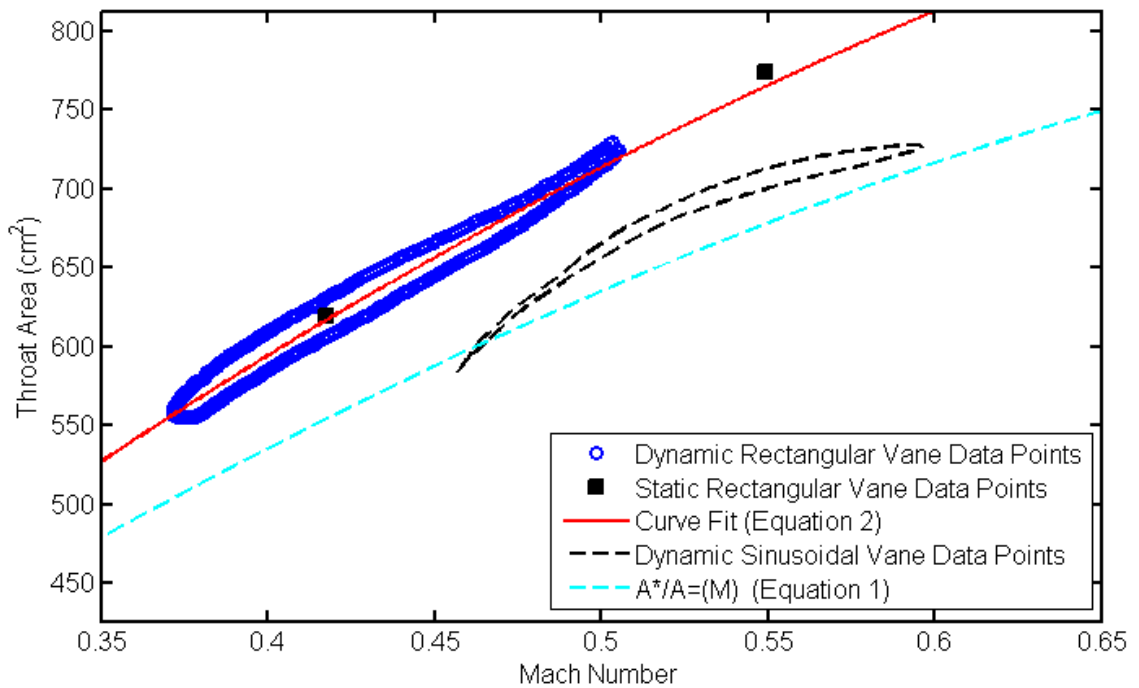


Figure 13: Throat Area vs Mach number for sinusoidal, rectangular static and dynamic data as well as Equation 1 and the designed curve fit

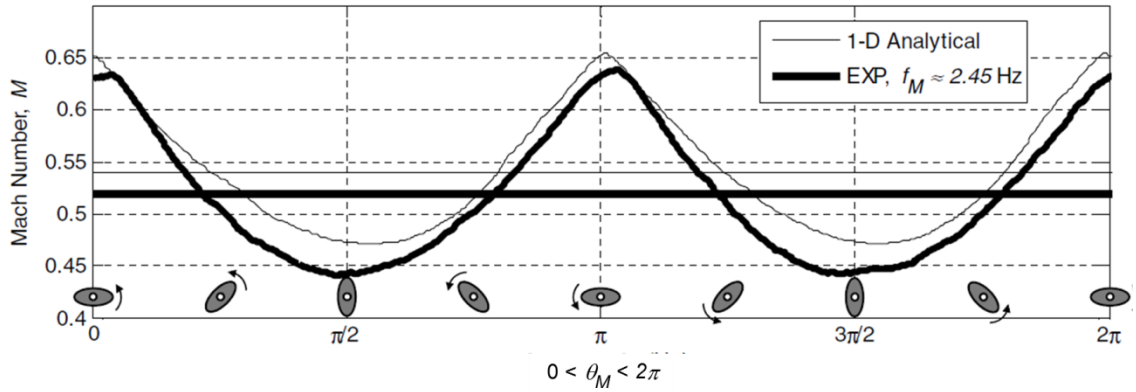


Figure 14: Designed test section Mach number oscillation compared to the test section Mach number, $f = 2.5 \text{ Hz}$ ³³

Equation 6 is the 1-D wave propagation speed. This is significant for this tunnel because it is operated in the compressible Mach regime and the test section is 1.75 m upstream from the choke vanes. As the Mach number increases, the flow requires a longer amount of time to propagate up the tunnel. The rectangular vane data seen in Figure 9 shows this hysteresis effect as the data does not collapse on itself for the upward and downward slope of Mach number. Therefore, by the time the Mach wave reaches the test section, the wave will be shifted with the higher Mach number flow lagging the lower speed flow.

Equation 6: Wave propagation speed.

$$C = a(1 - M)$$

A phase shift and wave steepening effect is observed as the period of the wave decreases while the propagation speed remains the same. Figure 15 shows how the waveform

changes with different frequencies, the Mach oscillation waves are shifted in phase to align at the maximum Mach number. It was also a prerequisite to normalize the Mach number due to the amplitude attenuation at the higher frequencies. The waveform shape is seen to change from a bottom heavy shape seen with the $f=2.5$ Hz oscillation to a more symmetrical sine wave in the $f=16$ Hz oscillation. The wave steepening from the propagation speed can be seen in Figure 15, with the minimum normalized Mach number moving to an earlier position in the period as the frequency is increased.

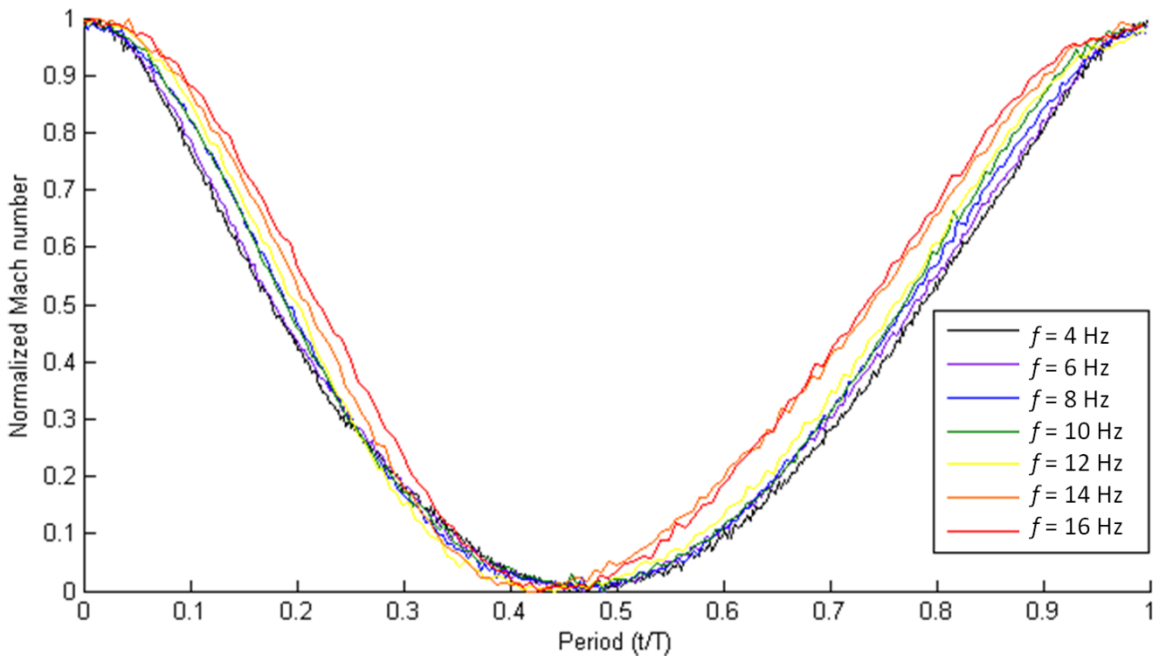


Figure 15: One period of normalized hot film data plotted at different frequencies illustrating wave steepening

The Mach number oscillation was further tested at frequencies up to 21 Hz. The hot wire study was able to characterize the Mach number oscillation amplitude and phase delay for this range of frequencies. The amplitude and phase shift bode plots of Mach

number oscillation are shown in Figure 16. The oscillation amplitude is attenuated significantly at high oscillation frequencies. Bode plots indicate that the -3 dB roll-off point is at approximately 8 Hz for an empty test section. The phase shift is a linear function of Mach number oscillation frequency, for a given mean Mach number, which indicates that the wavespeed is approximately constant. Figure 17 illustrates the phase shift and amplitude attenuation for four representative Mach oscillation waveforms at different frequencies.

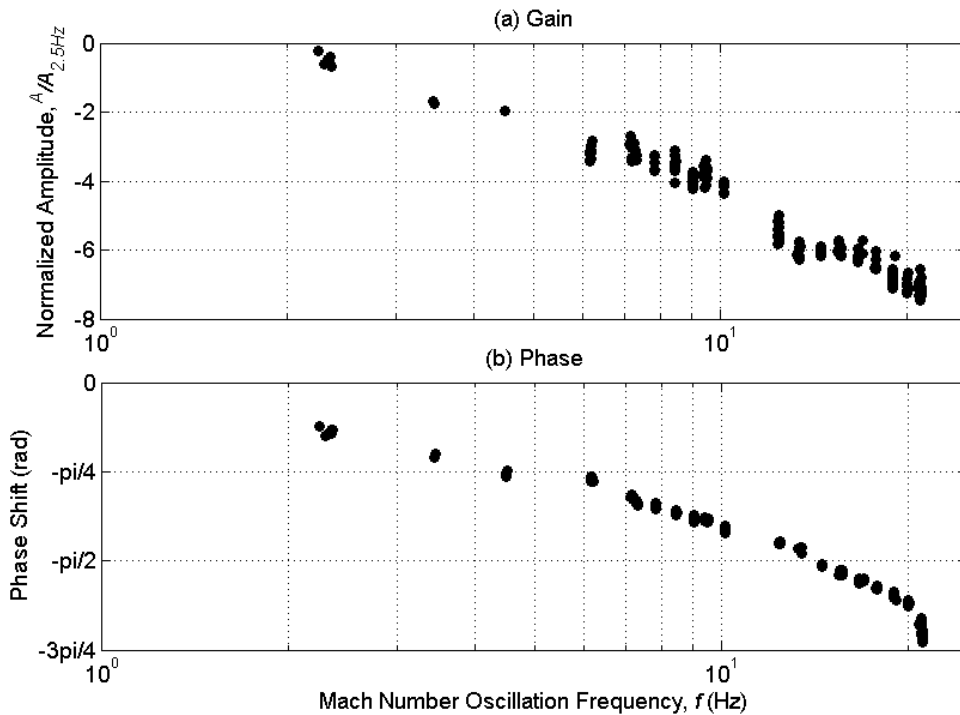


Figure 16: (a) Amplitude and (b) Phase Number vs. Mach Number Oscillation Frequency (f)³³

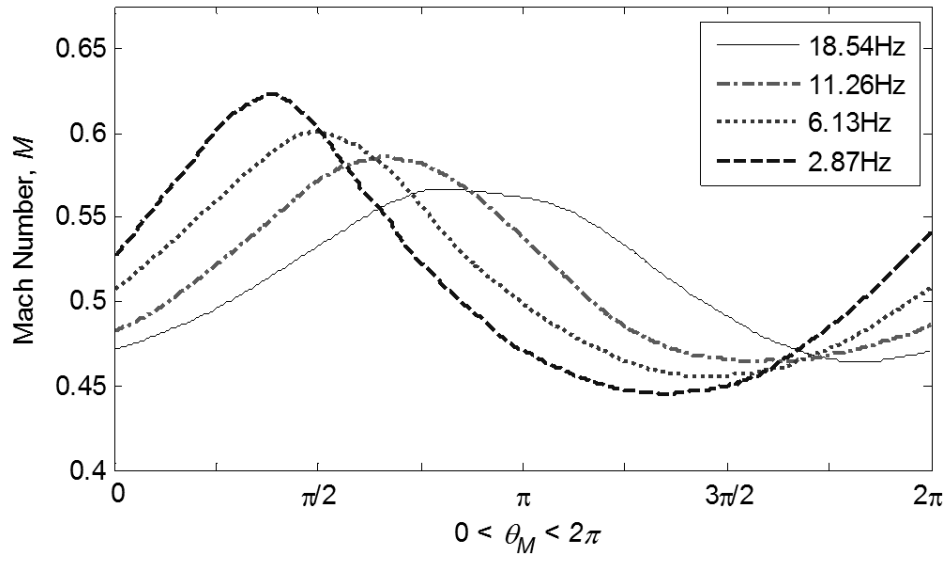


Figure 17: Representative test section Mach number waveforms at different oscillation frequencies³³

Chapter 4: Pressure Sensitive Paint

Section 4.1: Pressure Sensitive Paint Introduction

Pressure-sensitive paint (PSP) is an experimental technique based on the quenching mechanisms of luminescence molecules. Compared with conventional techniques like pressure taps, it offers a unique capability for high frequency, non-contact, full-field measurements of surface pressure on a complex aerodynamic model with higher spatial resolution at a lower cost. PSP has to be excited by a light source to trigger the luminescence response, which is the paint down-converting the excitation illumination to a longer wavelength. The intensity of this emitted light is inversely proportional to the amount of oxygen in the air and is also a function of the surface temperature of the model; as the luminescent intensity (I) of the phosphor is determined by the thermal and oxygen quenching mechanisms of the PSP. Temperature-sensitive paint (TSP) is insensitive to oxygen concentration, so its luminescent intensity is only a function of the model temperature.

Section 4.2: Lifetime- vs. Intensity-Based PSP Techniques

Lifetime- and intensity-method are the two major methods of recording the luminescent emission response from the PSP. The first method is lifetime-based, where the PSP is exposed to a pulsed excitation light. A double shutter scientific camera then images the luminescent intensity during the excitation illumination and the corresponding lifetime decay (τ) of the paint, which is shown as Equation 7 and illustrated in Figure 18.³⁴⁻³⁶ The lifetime-method for PSP is based on the fact that the luminescence decay lifetime is inversely proportional to the local oxygen concentration, which is directly related to the air pressure according to Henry's law. This relation is shown as the Stern-Volmer equation, Equation 8, where τ_{ref} and p_{ref} are the luminescent lifetime and air pressure at a reference condition, respectively. The Stern-Volmer coefficients A and B, which are temperature-dependent due to thermal-quenching, are experimentally determined by calibration.

Equation 7: The luminescent emission response.

$$I(t) = Ae^{-\frac{t}{\tau}}$$

Equation 8: Stern-Volmer equation.

$$\frac{\tau_{\text{ref}}}{\tau} = A(T) + B(T) \frac{p}{p_{\text{ref}}}$$

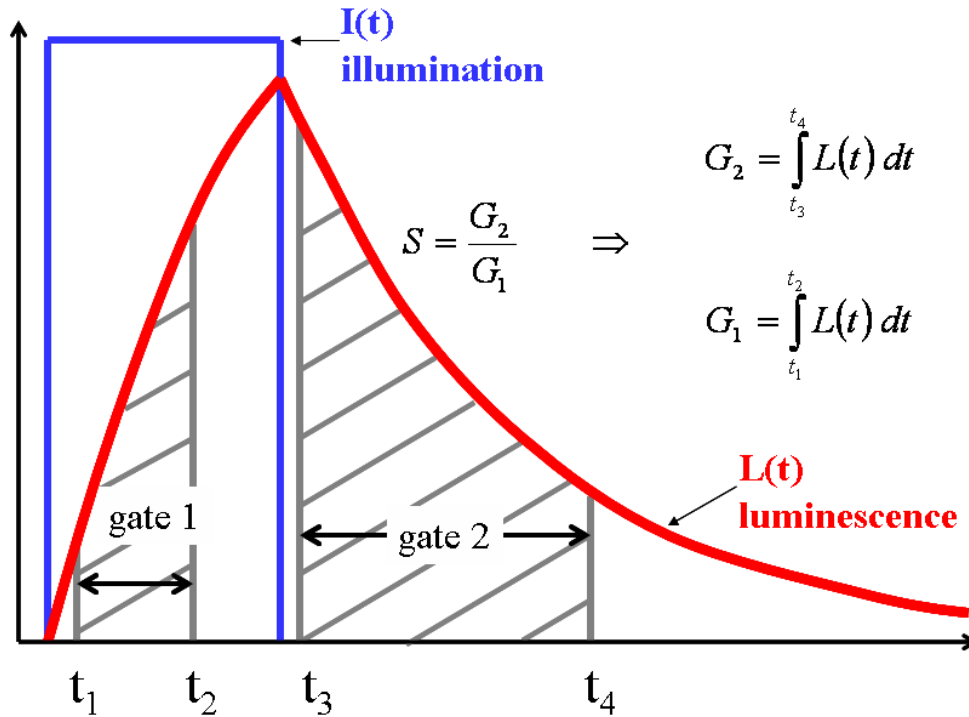


Figure 18: Representation of two-gate lifetime PSP measurement technique³⁷

Lifetime-based PSP measurement approaches include phase-sensitive detection and multi-gate integration techniques. A typical schematic of the two-gate lifetime approach is shown in Figure 18.³⁷ In the lifetime-based technique, paint excitation is provided by a modulated light source such as a pulsed laser or LED flash lamps. Generally, paint emission intensities are acquired and integrated over two distinct gates, where the first gate occurs during the illumination pulse and the second is centered on the decay of the fluorescence. In this application, however, two nearly contiguous gates are used, based on the double shutter mode of a charge-coupled device (CCD) camera. The first gate (G1) captures the signal in the illumination pulse, while the second gate (G2) captures the lifetime decay. The integrated signal of the first gate is relatively insensitive to pressure, thus serving as a reference, while the second gate signal is sensitive to

pressure changes according to the Stern-Volmer equation. The ratio of G1 and G2 is able to provide surface pressure information after calibration. In practice, the timing of these gates to optimize the pressure sensitivity of the lifetime PSP method and signal-to-noise ratio (SNR) is found at equal intensities of G1 and G2. The major advantage of the lifetime approach is the minimization of illumination errors by self referencing G2 with G1 for both the wind-on and wind-off images.

Theoretically, the lifetime of the paint at uniform pressure and temperature should be constant at each point on the surface. However, it has been shown by Goss et al. that this is not the case.^{38, 39} This spatial variation may be due to non-uniform illumination field or variations in luminophore concentration. While the source of this noise remains unclear, it has been demonstrated that a wind-off ratio can be used to minimize this noise in both the lifetime and intensity methods. In addition to illumination errors the temperature sensitivity of PSP is a source of uncertainty (see Section 6.5).

When the lifetime-based method is applied using a single-shot technique, it is capable of eliminating the excitation variations, model movements and model deformations due to the technique being self-referenced. In this method, a high-power laser is selected as the illumination source, for the purpose of improving signal to noise ratio during data acquisition. Due to the pulse-to-pulse non-uniformity of laser illumination it is always necessary to utilize the lifetime mode, where both the pressure and reference images are obtained on the same decay curve from a single laser pulse. This single-shot lifetime PSP method was applied by Kumar for surface pressure measurements on rotating surfaces with unsteady pressure fluctuations.⁴⁰ It is also suitable for unsteady applications with large pressure gradients and model movements,

such as oscillating airfoils in compressible flow. Additionally the single-shot lifetime-method was utilized in the 6" × 22" Transonic Wind Tunnel for the initial Mach oscillation PSP study by Jensen et al., the schematic diagram of the setup can be seen in Figure 19.⁴¹ This study utilized a fast-response porous polymer paint which was first developed by Scroggin et al..⁴² This paint is a polymer/ceramic based PSP which was designed specifically to improve the diffusivity of the binder material, thus allowing faster response times. Its kinetic characteristics were studied in detail by Gregory et al.; it has a flat response time greater than 5 kHz, which is sufficient to study the flow field on airfoils with oscillating freestream frequencies less than 21 Hz.^{43, 44} PtTFPP, a typical platinum porphyrin-based luminophore, was used as the PSP sensor in the initial unsteady PSP study by Jensen et al. and as the pressure channel of the bi-luminophore paint during the later NACA 0012 steady and unsteady experiemnts.⁴⁵

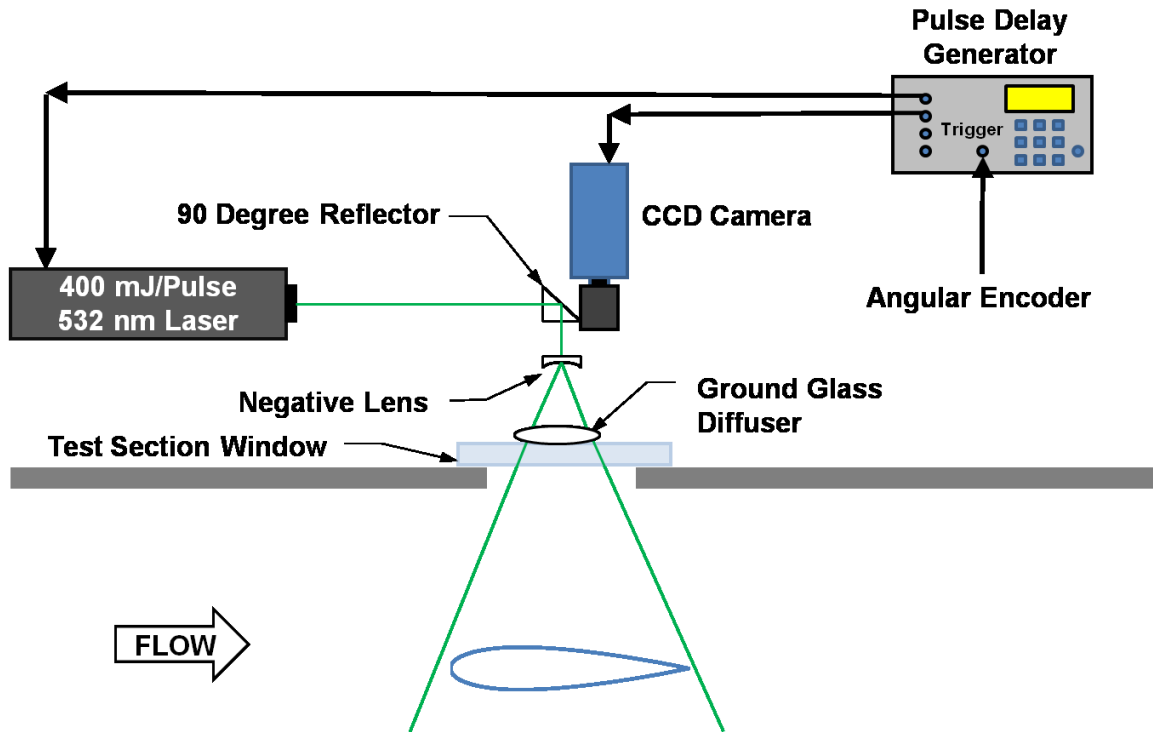


Figure 19: Schematic diagram of the single-shot lifetime-method PSP experimental setup

The other major PSP method is called the intensity-based method, wherein the illumination source is continuously on and the camera records the intensity of paint. This requires the illumination source to be very consistent. It has the advantage of being a much simpler technique and does not require a double shutter mode camera. The phase locked triggering of the camera shutter is still onerous yet simpler when compared to that of the lifetime-method, due to the lifetime-based method requiring specific timing between the illumination pulse and both camera shutters. The drawback of the intensity-based method is that continuous and consistent illumination provided by LED's is not as powerful as with a pulsed laser. In the past this has caused the need for phase averaging to boost the SNR of the paint to acceptable levels. In recent years, however, illumination

sources have become powerful enough to acquire all of the data needed in a single shot, similar to the method described with the lifetime method. Initial experiments on a NACA 0021 utilized the lifetime method with 400 mJ per pulse of energy. However, the Nd:YAG-532 nm laser as an illumination source is not compatible with the bi-luminophore paint because it overlaps with the emission spectrum of the temperature channel. Therefore, a set of three LEDs were utilized to provide 18 W of continuous 405-nm-wavelength illumination on the airfoil surface. This advance in LED illumination power effectively enables the pressure and temperature sensitive paint to make single-shot measurements. The single-shot intensity-method was chosen for experimental setup for its ability to instantaneously acquire the unsteady temperature and pressure map.

Section 4.3: Temperature Compensating Pressure Sensitive Paint

The single-shot pressure-sensitive paint technique is new compared to the more common phase-averaging PSP technique.⁴⁰ The advantage of the single-shot PSP for unsteady measurements is the ability to capture all the data within a few microseconds. Transient effects that would normally be averaged out under the phase-averaging technique are captured with the single-shot technique. Jensen et al. tested the validity of this method in a changing temperature environment.⁴¹ A NACA 0021 airfoil was tested in the 6" × 22" Transonic Wind Tunnel in oscillatory flow to evaluate this PSP technique for making unsteady pressure measurements and to begin study of the transient shock characteristics in quasi-steady flow. The airfoil was tested at a Mach oscillation

frequency of 2.45 Hz. An example coefficient of pressure (C_p) profile plot and upper surface C_p contour map can be seen in Figure 20. Due to the wind tunnel being a blowdown facility, the stagnation temperature drops throughout the run, typically 15 K during a 25 second run. These temperature effects on the PSP can be seen as a false rise in the C_p of the airfoil at the trailing edge and the spanwise non-uniformity in the upper surface C_p map, as shown by a theoretical black dashed line in Figure 20. The false rise is due to a temperature change from the wind-on to the wind-off images and is intrinsic to the PSP's temperature sensitivity. An *in situ* calibration is able to compensate for variations in bulk temperature shifts; however spanwise and chordwise variations in temperature will still be prevalent sources of error in the data. The chordwise temperature variation can be seen most dramatically at the aft end of the airfoil, where it is the thinnest and has the largest gradients in temperature. Additionally the spanwise variations are due to the model conducting heat through the tunnel sidewalls due to different endplate shapes on the airfoil model.

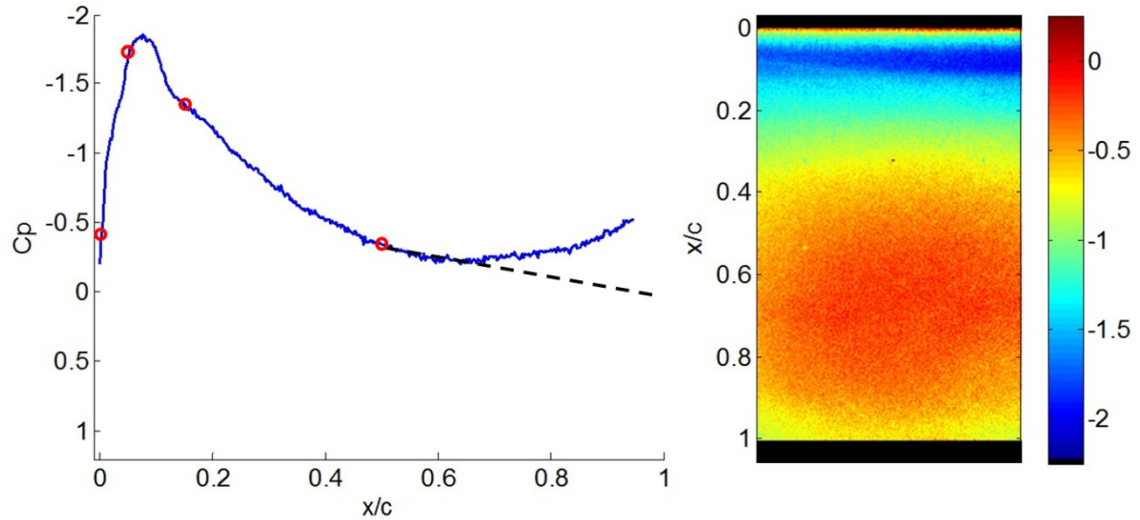


Figure 20: Single-luminophore PSP derived C_p plot (left) and upper surface C_p map (right) for a NACA 0021 under oscillatory flow at $f=2.5$ Hz, $\alpha=10^\circ$, $Re=4.1$ million, and $M=0.61$

In this lifetime-based test the PSP was calibrated via an *in situ* method using the pressure taps at x/c of 15 and 50% on the upper surface. Only two pressure taps are needed because the pressure calibration is assumed to be linear over this small pressure range. Furthermore, the accuracy of the calibration over the first half of the airfoil is illustrated by how well the third and fourth pressure taps agree with the calibrated PSP, as seen by the red circles in Figure 20 (left). This *in situ* calibration is necessary to account for the temperature drop throughout the operation of the blowdown wind tunnel. However, this technique only provides a bulk correction for temperature effects across the solid aluminum airfoil. This effect is shown in Figure 20, where the slope of C_p changes past x/c of 70%. Even with the poor calibration at the trailing edge, this figure illustrates the detail PSP can offer in spatial resolution and the detail in which a relatively weak standing shock wave can be resolved.

Due to these large variations in temperature throughout the tunnel run a temperature correction method is needed in order to make accurate PSP measurements, which is discussed further in Section 6.4. The method used a bi-luminophore pressure- and temperature-sensitive paint. A typical pressure sensor and temperature sensor were combined into one paint formulation and were separated spectrally with regards to their emission signals. This bi-luminophore method allows for the addition of a reference channel that is only sensitive to temperature to account for the pressure channel's temperature-sensitivity. Thus, an accurate PSP measurement is obtained while also acquiring the temperature map for the model if needed. Various other authors have attempted similar bi-luminophore techniques as summarized in Peng et al.^{46, 47} Alternative temperature correction techniques have used infra-red cameras and bifurcated airfoils painted half with each TSP and PSP.

Section 4.4: Two Camera vs. Color Camera PSP and TSP Methods

Two different camera methods were evaluated for this temperature compensated PSP measurement. A standard color camera with a built-in red green blue (RGB) Bayer filter over the individual pixels was initially employed.^{46, 47} By only having one camera this technique was very easy to implement optically. It was found that the Bayer filter on the camera, an Alta U2000C, had significant filter overlap between the color channels, which added pressure sensitivity to the temperature channel. It was also challenging to

create a bi-luminophore paint formulation that had similar intensities for both the pressure and temperature channels at all operating conditions.

The two camera method was therefore investigated, compromising the ease of optical setup for that of flexibility to optimize the intensity of each camera individually by means of pixel binning and aperture settings. Additionally individual filters could be chosen for each black and white PCO-1600 camera in order to minimize the bleed through of each color channel and give better optical spectral separation. For these reasons the two-camera method was chosen for this experiment. A direct comparison of the unfiltered contours of C_p measured with the two methods can be seen in Figure 21. The two-camera method is seen to have less noise and thus a better signal to noise ratio.

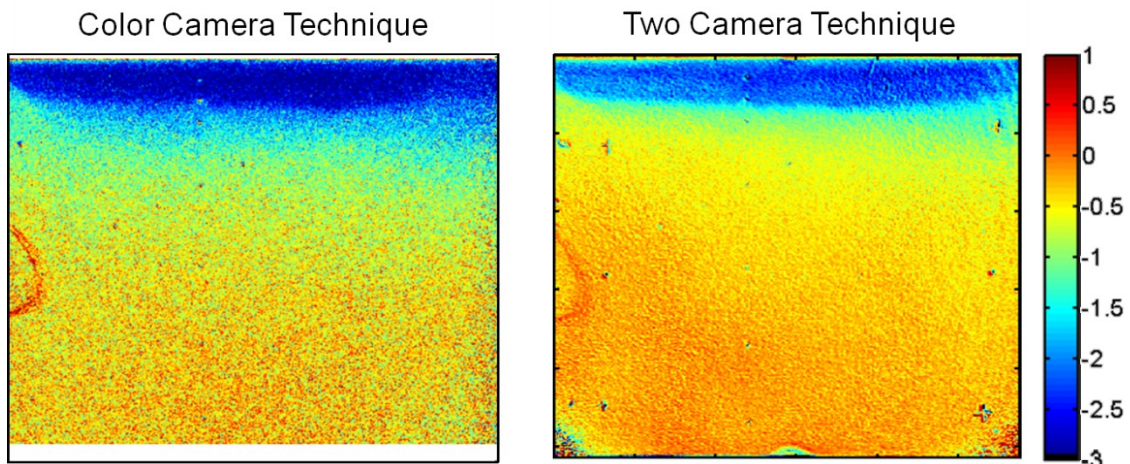


Figure 21: Comparison of the raw temperature-corrected contours of C_p for the Color Camera, Left, and the Two Camera technique, right, on a NACA 0012 at $f=9.5$ Hz, $\alpha=9^\circ$, $Re=3.9$ million, and $M=0.57$, flow from top to bottom

The two methods were compared quantitatively as follows. The intensity ratio of the green channel was recorded for both the two-camera and color-camera methods for a

matrix of pressures and temperatures. The calibration was performed in a specially built calibration chamber designed to hold pressure and temperature in a range from 0 to 241 KPa and -8 to 50° C, respectively. An Ocean Optics USB4000 spectrometer was used to illustrate TSP's insensitivity to pressure as well as the spectral separation between the two channels, as seen in Figure 22 and Figure 23, from Peng et al..⁴⁷ The color and two-camera filters were overlaid onto the spectroscopy data. It can be seen that the green filter of the color camera also collects some of the pressure data at 700 to 750 nm wavelengths; this gives false pressure sensitivity to the TSP measurement. Figure 24 and Figure 25 show the temperature vs. green intensity for the color- and two-camera methods, respectively, with a reference temperature of 20°C. A second order polynomial was fit to the presented data and characterized by the coefficient of determination, R^2 . In the color camera data it is apparent that the temperature channel is acquiring some of the luminescence signal from the PSP thus showing some pressure sensitivity due to the poor quality of the Bayer filter. Surface fits were performed for the pressure channel with their respective R^2 values presented in Table 1.

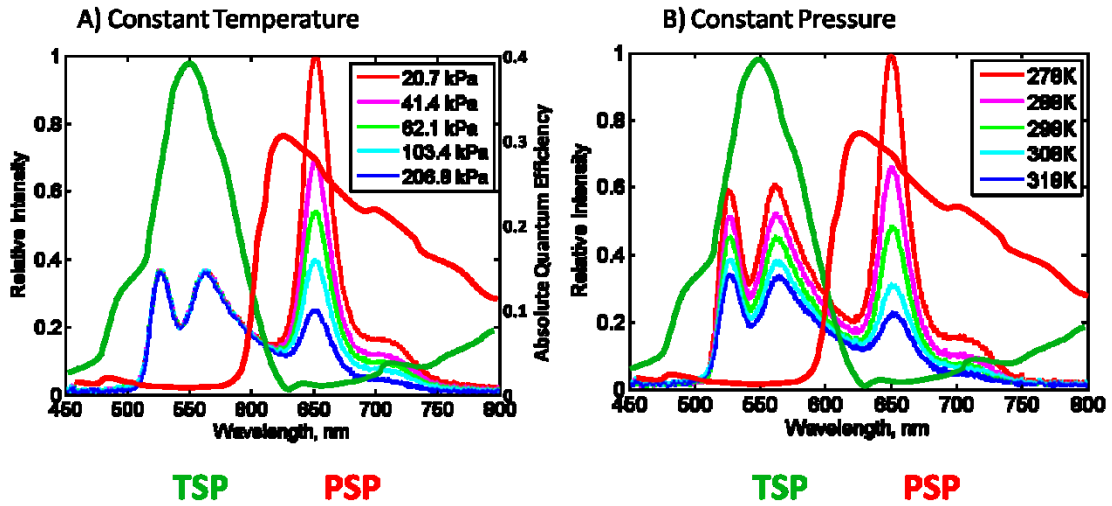


Figure 22: Emission spectra for the color camera technique at A) different pressures and constant temperature and B) different temperatures and constant pressures, with the respective green and red band-pass optical filters shown⁴⁷

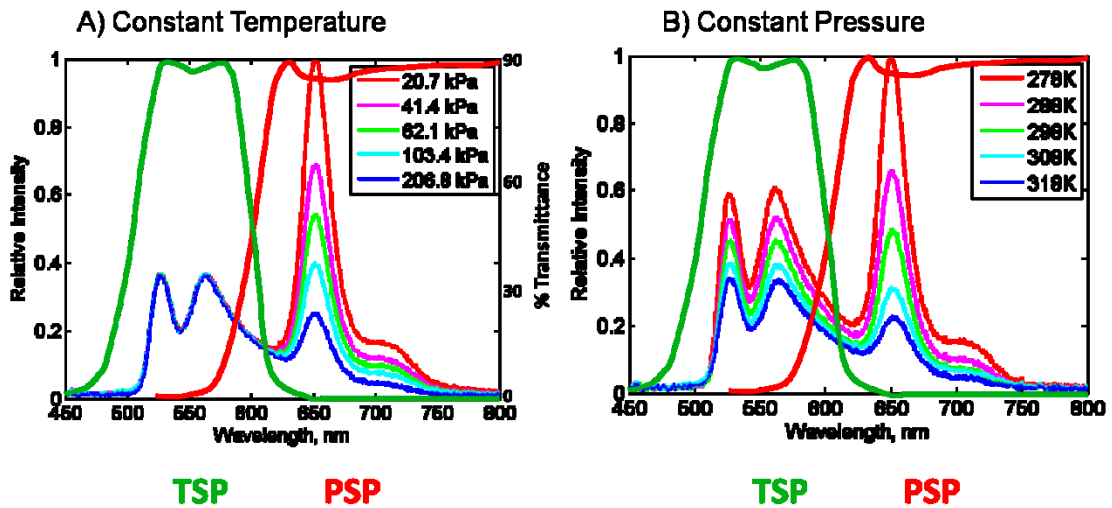


Figure 23: Emission spectra for the two-camera technique at A) different pressures and constant temperature and B) different temperatures and constant pressures, with the respective green and red band-pass optical filters shown⁴⁷

Table 1: R^2 values for the pressure and temperature curve fits for the color and two camera methods.

	Two Camera	Color Camera
Temperature R^2	0.998	0.978
Pressure R^2	0.991	0.980

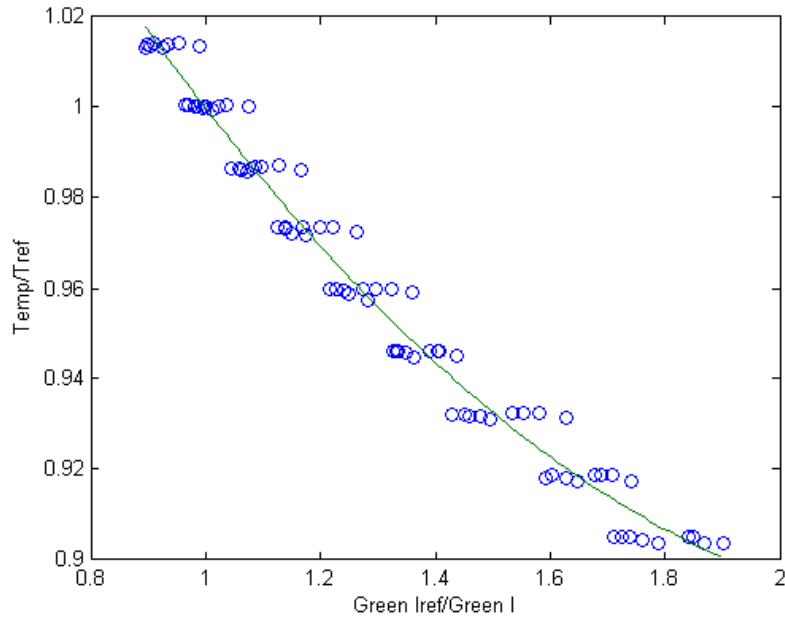


Figure 24: Temperature calibration curve for the color-camera method

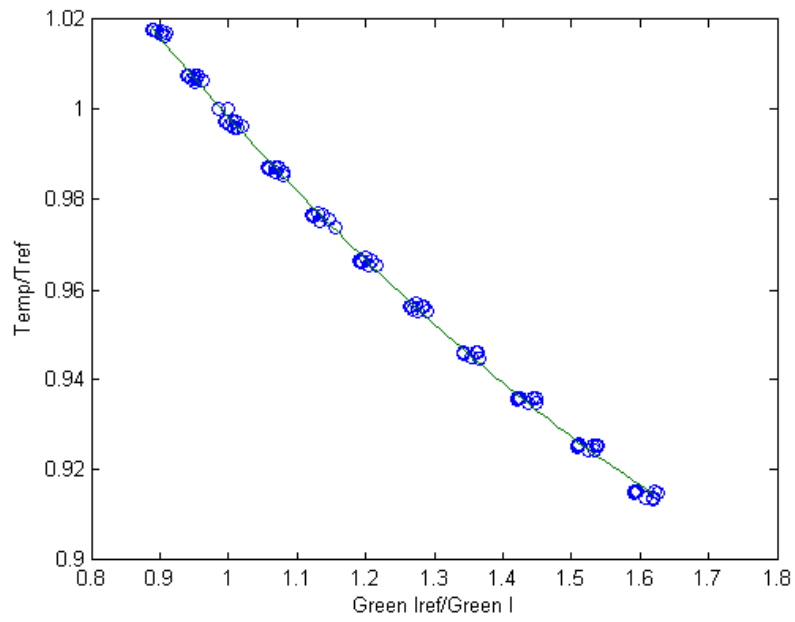


Figure 25: Temperature calibration curve for the two-camera method

Chapter 5: Experimental Setup

Section 5.1: Experimental Setup Introduction

Three different experimental setups were employed in this work, the initial characterization of the wind tunnel, model surface pressure- and temperature-sensitive paint measurements, and off-body particle image velocimetry measurements.

The same equipment was used to measure tunnel conditions for all three setups. The wind tunnel is equipped with two 350 kPa absolute pressure transducers which are attached to a total and a static pressure port. Both have a calibration uncertainty of ± 690 Pa and a frequency response greater than 300 Hz. The total pressure probe located in center of the stagnation tank is connected to the pressure transducer via a 0.75-m-long 6.4mm-diameter tube. This pressure line adds a phase lag to the total pressure signal which distorts the signal at frequencies above 5 Hz. For this reason, the total pressure measurement was phase shifted to align with the static pressure in order to calculate the tunnel's Mach number. A Type K thermocouple located in the stagnation tank was used to measure the total temperature. Isentropic relations were then used to calculate the static temperature and sonic velocity in the test section.

Section 5.2: Pressure and Temperature Sensitive Paint Experimental Setup

The airfoil is a NACA 0012 with a chord of 12.7 cm (5 in) and a 15 cm (6 in) span, as seen in Figure 26. It is equipped with 10 pressure taps of 1.27 mm inner diameter along the upper surface and two on the lower surface at coordinates listed in Table 2. The tap locations were selected by the author specifically for PSP calibration. These taps were connected to a Pressure Systems, Inc. 9016 pressure brick of 16 differential pressure transducers with a range of ± 310 KPa, an accuracy of ± 210 Pa, a measured frequency response greater than 50 Hz and a phase delay of 7 ms due to acoustic effects caused by 25.4 cm of 1.27 mm inner diameter tubing. These pressure taps were used to perform an *in situ* calibration of the PSP. Additionally, two Te Technology, Inc. MP-2444 thermistors were located at $x/c = 0.20, 0.85$ and $z/b = 0.933$ and 0.933 , respectively, and were similarly used for an *in situ* calibration of the TSP. The thermistors were mounted flush to the surface of the airfoil, had a diameter of 0.89 mm and a range of -20 to 100°C.

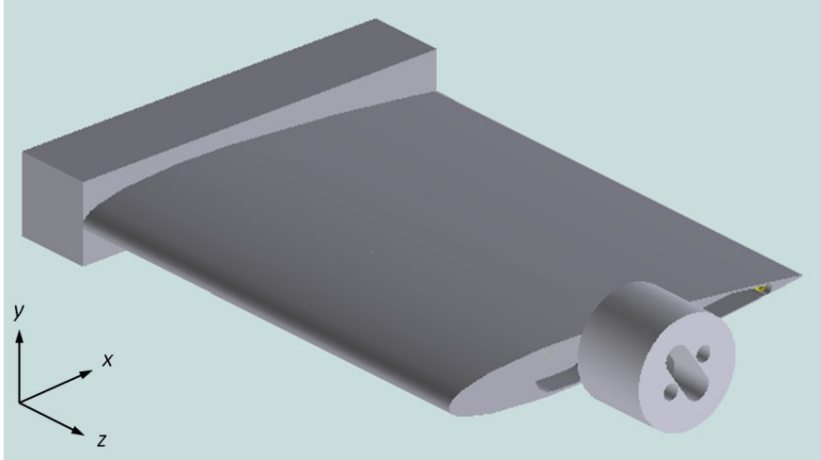


Figure 26: Diagram of the NACA 0012 airfoil model tested

Table 2: Pressure tap locations on the NACA 0012 airfoil

Upper Surface										
$x/c =$	0.050	0.100	0.150	0.250	0.300	0.350	0.400	0.500	0.700	0.900
$z/b =$	0.583	0.583	0.583	0.500	0.583	0.667	0.750	0.583	0.583	0.583
Lower Surface										
$x/c =$	0.100	0.500								
$z/b =$	0.583	0.583								

A 500-counts-per-revolution optical encoder was utilized to phase lock the PSP images to the vane oscillation. This was accomplished through the use of a National Instruments PCI-6602 counter board. The counter board read the once- and 500-per-revolution signals and then sent a variable phase delay trigger pulse to both cameras. This was done to ensure accurate phase separation for the images while minimizing the run duration. The total temperature, TTL trigger pulses, once per revolution, 500 per revolution, thermistors, total and static pressures data were then recorded by a National Instruments PCI-6251 multifunction data acquisition board to a computer at a frequency of 4 kHz for post processing.

A fast-response, two-color porous polymer paint was selected for this experiment, which was recently developed by Peng et al..⁴⁷ This paint is a polymer/ceramic based PSP, which was designed specifically to improve the diffusivity of the binder material, thus allowing faster response times. PtTFPP, a typical platinum porphyrin based luminophore, was used as the pressure sensor in this experiment. Perylene and a laser dye were added as the temperature sensor. The laser dye shifts the temperature signal to a shorter wavelength for improved spectral separation between the PSP and TSP, which allows for the use of optical filters to split the data acquisition into red and green signals. The intensity-based method utilizes a continuous illumination source of 405-nm-wavelength light-emitting diodes. The signals from pressure and temperature channels are well separated in spectrum and can be recorded simultaneously either by a color-camera or a two-camera system. By co-locating fast responding pressure and temperature sensors it becomes possible to make high fidelity spatial measurements of the airfoil surface pressure and temperature.

The two camera technique uses a beam splitter to allow for both the temperature and pressure cameras to have the same optical view through the limited optical access on top of the tunnel. Each camera utilized an optical filter to record the red and green illumination intensities. The 405 nm excitation light was provided by LED arrays through the side windows of the wind tunnel. The schematic diagram of the two camera setup can be seen in Figure 27. The red channel utilized a 590 nm long-pass filter while the green channel used a 515 – 600 nm band-pass filter to separate the signals.

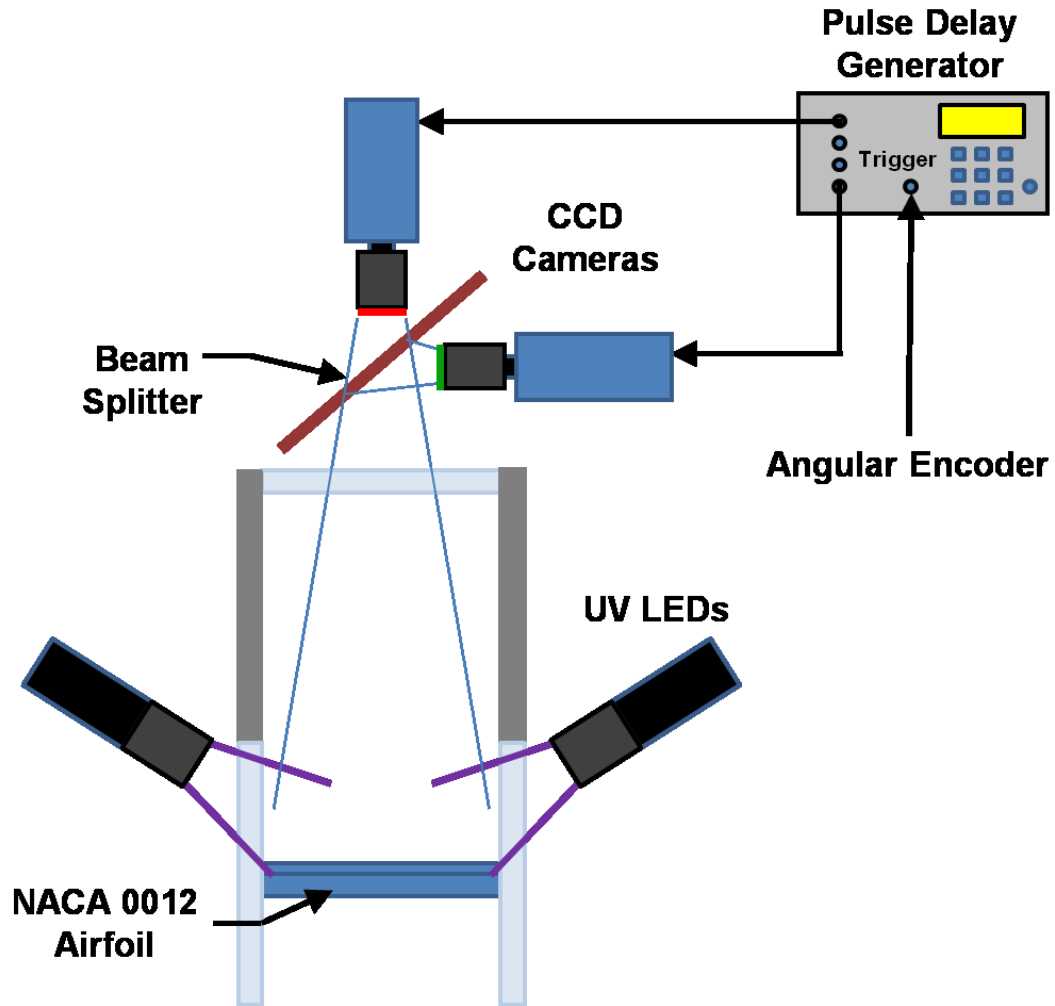


Figure 27: Block diagram of the PSP data acquisition setup, viewing down the longitudinal axis of the wind tunnel.

Section 5.3: Particle Image Velocimetry Experimental Setup

Two-dimensional velocity data were acquired for the NACA 0012 airfoil using a single camera positioned beside the test section by Gompertz.⁴⁸ The PIV setup and data collection was performed by Kyle Gompertz, not the author, and is used as a comparison

to the PSP and TSP data. The camera field of view extends from approximately 15% x/c upstream of the airfoil leading edge to 30% x/c , to observe transient shock-boundary layer interaction. The particle image velocimetry (PIV) illumination was provided by a 200 mJ / pulse, 532 nm wavelength double-pulsed Nd:YAG laser with a maximum rate of 15 Hz. The laser beam was expanded into a light sheet through a cylindrical negative lens and entered the test section from the top window. The camera imaged the laser sheets through the side window of the tunnel test section with a band-pass filter to only record the laser light.

The two consecutive laser sheets were adjusted and measured to be 1mm thick in the x-y plane at the airfoil midspan location, $z/b = 0.5$. The time separation between laser sheet pulses was varied from 0.8 – 1.2 μs to limit the maximum particle displacement to 7 pixels depending on the maximum time-averaged velocity in the data window. The flow was seeded with Di-Ethyl-Hexyl-Sebacate (DEHS) particles of submicron diameter. As described in Section 5.2, an optical encoder on the choke vane was used to trigger phase-locked data acquisition at 12 discrete phases of the Mach number oscillation period. Data was recorded at $f = 9.5$ Hz, $\alpha = 9$ and 10° . Approximately 100 PIV image pairs were acquired for each phase, which is sufficient to represent the phase-averaged velocity.^{32, 48}

Chapter 6: Data Processing Techniques

Section 6.1: Data Acquisition Board Post-Processing Techniques

The information recorded from the data acquisition board was saved to a computer hard drive for post-processing. The first step of the process is to low pass filter the pressure and temperature data. These values along with the angular encoder signal were then averaged over the same duration as the camera shutters were open. This effectively created point measurements for which to check the a priori calibration of the PSP and TSP and use for an *in situ* calibration. In addition, these data were also used in calculating the traditional aerodynamic condition data: Mach number, Reynolds number, q , P_o , P_s , and T_o . The PSP and TSP images are registered, median filtered and calibrated as discussed in Sections 6.2 through 6.4 respectively.

Section 6.2: Image Registration Techniques

The PSP and TSP images must be registered to the same field in order to take the appropriate ratios and obtain reliable data. The wind-on and wind-off images for both the green and red channels must be aligned in this way. Additionally all of the images in the

run must be properly aligned to obtain meaningful measurements throughout the run. This was accomplished by first locating the fiducial marker locations. Due to the large number of images, 200 to 1000 per run, these steps were automated and the code can be seen in Appendix B. The fiducial markers, including the pressure taps and airfoil leading and trailing edges were located by taking the local standard deviation of each wind-on and off image, as seen in Figure 28. A two-dimensional cross correlation was performed between the first wind-off standard deviation image and every other image in the run. This forced all of the images for each run to align with one another. The images were then rotated to a right angle and cropped to only show the airfoil surface.

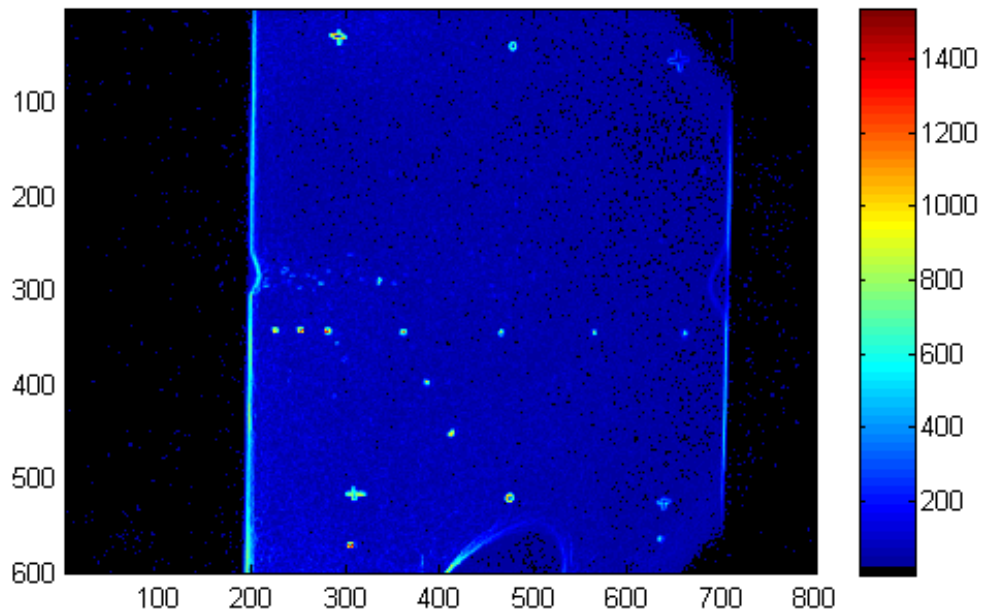


Figure 28: Representative standard deviation of a wind-off image (axes in pixels), locating the fiducial marker, pressure taps and airfoil edges

Section 6.3: Image Filtering Techniques and Implementation

Filtering is a typical data processing technique in pressure sensitive paint; however, there are tradeoffs between different filter types which will be described in this section. By applying a top hat filter over the image surface one is essentially low-pass filtering the data with the goal of removing the erroneous white noise while maintaining the data quality. To illustrate this process a nominal PSP image was selected from a steady run at $M = 0.46$, $Re = 3.65 \times 10^6$ and $\alpha = 9^\circ$, as seen in Figure 29. This image was chosen due to the relatively weak standing shock on the leading edge of the airfoil.

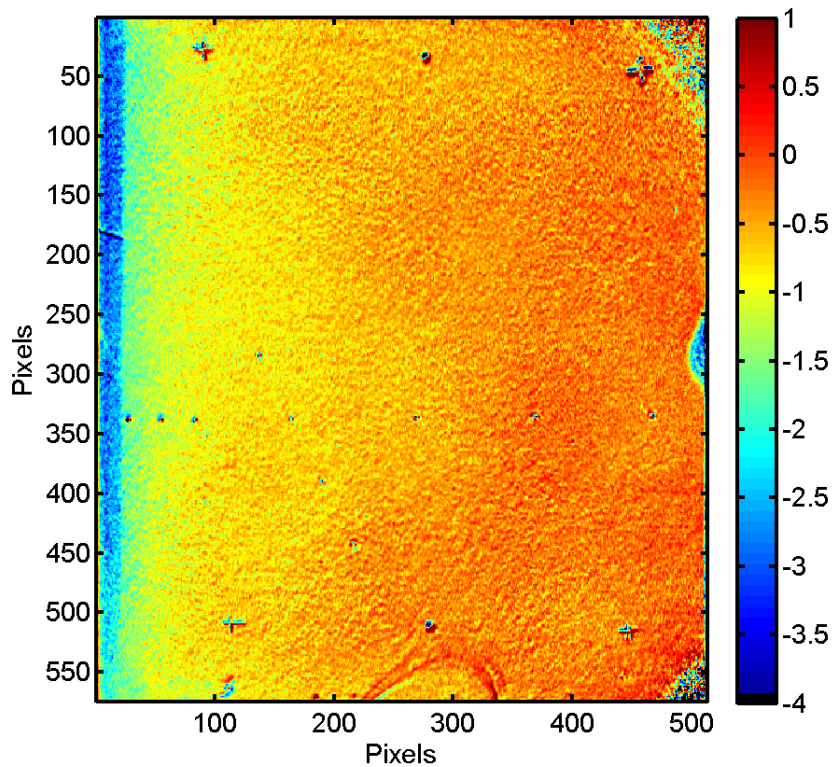


Figure 29: Unfiltered C_p map of the upper surface NACA 0012 at $M = 0.46$, $Re = 3.65 \times 10^6$ and $\alpha = 9^\circ$, flow from left to right

Three standard digital filters were applied in the post-processing of the PSP images to evaluate the performance of each filter, mean, Wiener, and median. The mean filter as seen in Figure 30 used a disk top hat filter with a radius of 8 pixels. The Wiener and median filters seen as Figure 31 and Figure 32 respectively used a rectangular filter pattern of 30 pixels in the spanwise direction and 10 pixels in the chordwise direction. The filter was shorter in the chordwise direction due to the higher changes in pressure as compared to that of the spanwise direction.

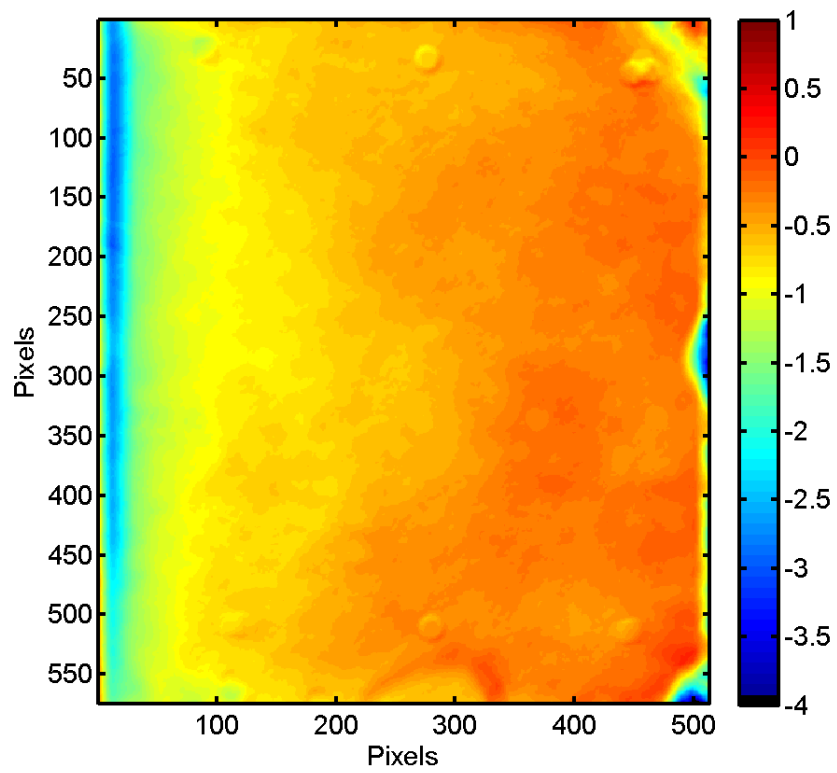


Figure 30: Mean top hat filtered, with a radius of 8 pixels, C_p map of the upper surface NACA 0012 at $M = 0.46$, $Re = 3.65 \times 10^6$ and $\alpha = 9^\circ$

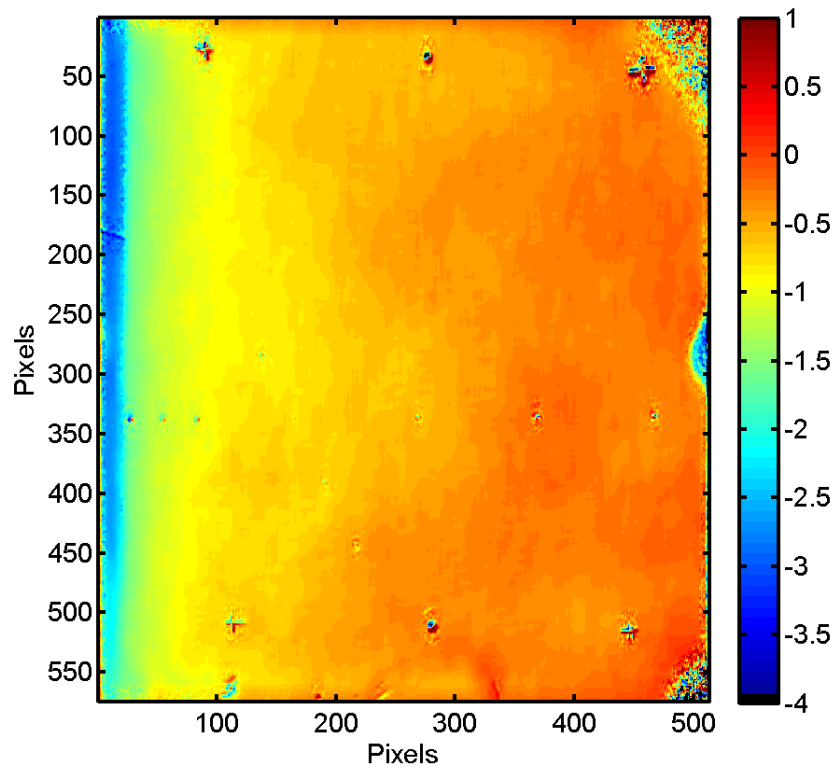


Figure 31: Wiener top hat filtered, 30 pixels in the span wise and 10 pixels in the chord wise direction, C_p map of the upper surface NACA 0012 at $M = 0.46$, $Re = 3.65 \times 10^6$ and $\alpha = 9^\circ$

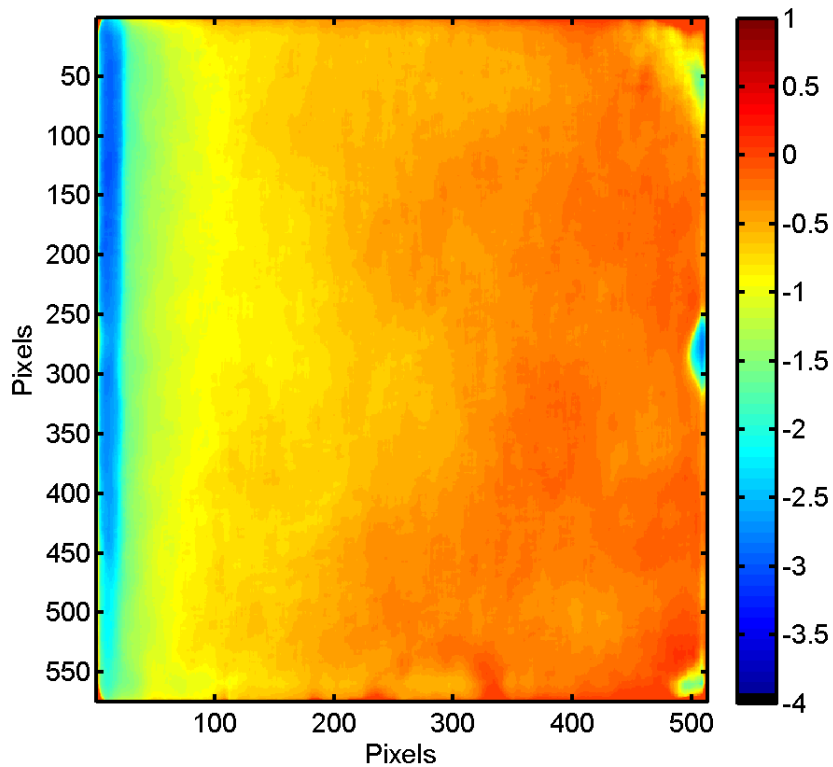


Figure 32: Median top hat filtered, 30 pixels in the span wise and 10 pixels in the chord wise direction, C_p map of the upper surface NACA 0012 at $M = 0.46$, $Re = 3.65 \times 10^6$ and $\alpha = 9^\circ$

These raw and filtered images were then compared directly for one C_p slice at the spanwise location of 350 pixels or $z/b = 0.608$, just below the majority of the pressure taps at $z/b = 0.583$. Figure 33 shows the full chord for all of the filters while Figure 34 is zoomed in on the first 25% of the NACA 0012. It becomes apparent that all three filters remove a majority of the high frequency noise. However, the median filter preserves the shock gradient at the leading edge and reduces the white noise most effectively. Furthermore, median filters are standard practice for non-parametric data analysis where a normal distribution cannot be assumed.⁴⁹ Thus with varying sample sizes, an unknown

normal distribution, and the ability to preserve abrupt features such as shocks while eliminating high frequency noise, the median filter was chosen as the image processing filter for this experimental data set. With the setup used there were 5.14 pixels per percent x/c .

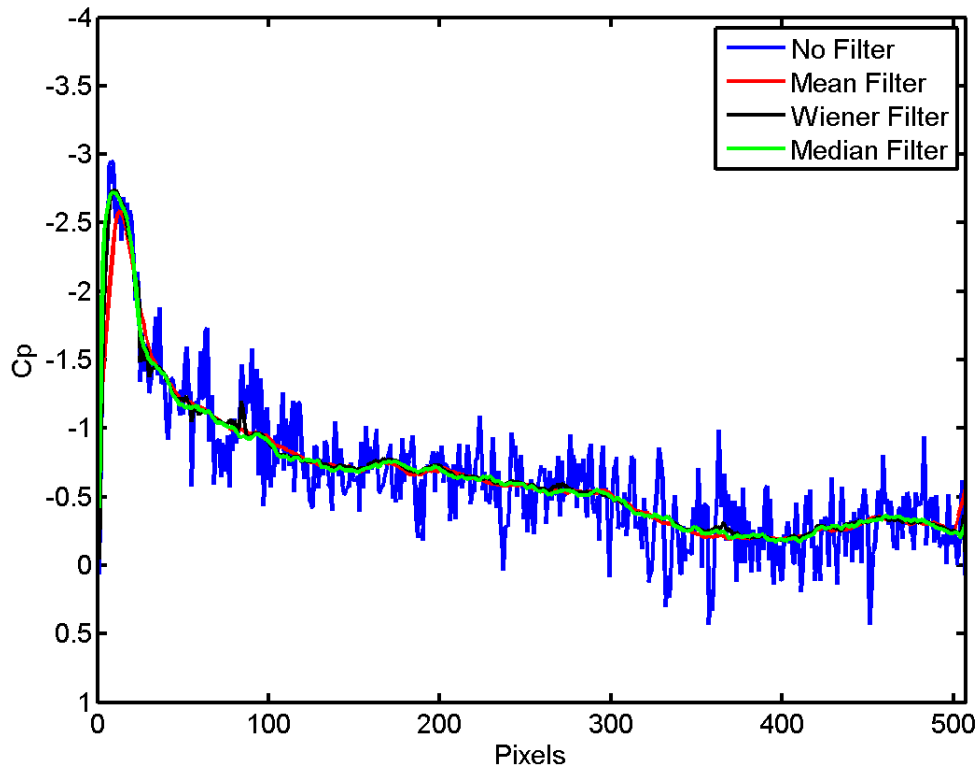


Figure 33: C_p profile plot of the unfiltered and three filtering methods of a NACA 0012 at $M=0.46$, $Re=3.65 \times 10^6$ and $\alpha=9^\circ$ at the spanwise location of 350 pixels

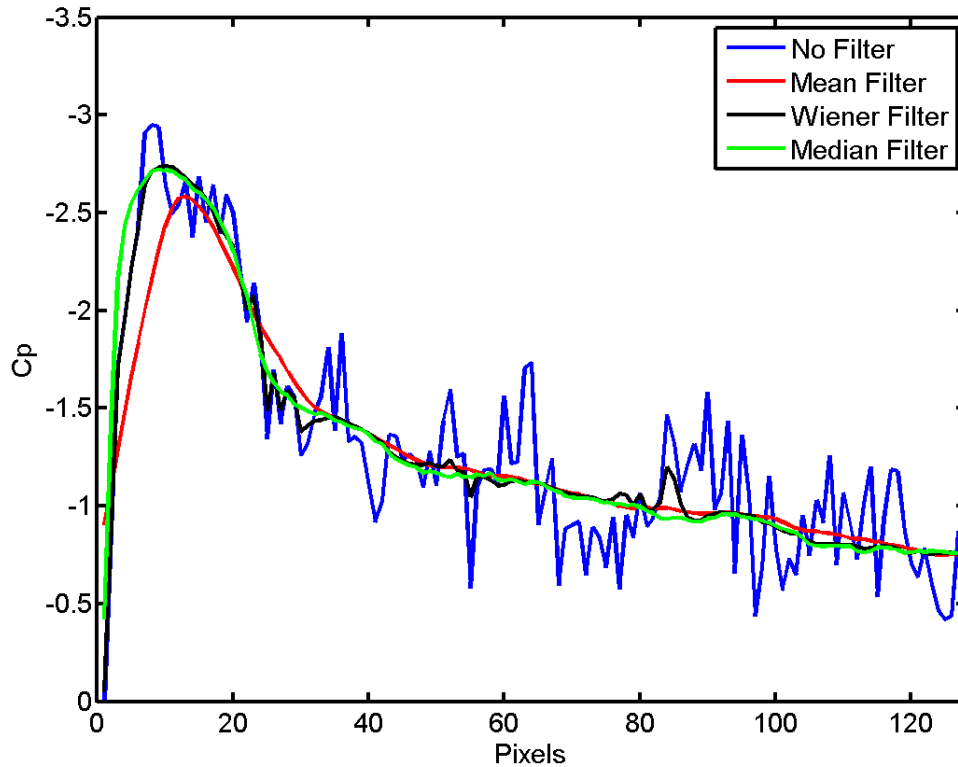


Figure 34: First 25% x/c C_p profile plot of the unfiltered and three filtering methods of a NACA 0012 at $M=0.46$, $Re=3.65 \times 10^6$ and $\alpha=9^\circ$ at the spanwise location of 350 pixels

Section 6.4: Pressure and Temperature Calibration

A priori and *in situ* calibrations are the two major methods of calibration for pressure sensitive paint. The *a priori* method utilizes a pressure and temperature calibration chamber to record the emission intensity of the PSP and TSP at known, steady pressures and temperatures. These intensities are then divided by the reference condition to calculate the intensity ratio for each point in pressure and temperature. This method

was attempted for this experimental setup, although changes in the reference condition carried large impacts into the results. The reference condition in the *a priori* method is assumed to be at a uniform pressure and temperature, which is not valid after even one run. As cold, expanded air flows through the tunnel, the airfoil and 2.54-cm-thick aluminum side walls cool which is slowly dissipated back to the atmosphere. This causes the airfoil to have a temperature gradient during the wind-off image as the thin trailing edge cools and warms more rapidly than the thicker leading edge. Additionally the sides of the airfoil model are different as seen in Figure 26, which causes a spanwise gradient in temperature. This heat transfer between runs negates the assumption of uniform temperature over the reference image.

For a bi-luminophore PSP, the *in situ* method is implemented by defining the calibration of PSP intensity ratio based on the surface pressure taps. However a typical *in situ* calibration was not possible in this test due to the attenuation and phase shift in the pressure tap lines during the unsteady Mach oscillation runs. For this reason the PSP data could not be calibrated for the high frequency Mach oscillation runs and was only used to investigate the shock location.

A surface fit calibration method was devised to compensate for the transient temperature field. This *in situ* method utilizes pressure tap data, of the steady runs, to create a surface fit calibration for pressure with respect to the green and red channel intensity ratios. This surface fit calibration method allows for one calibration for each run that accounts for both variations in pressure and temperature. Whereas, with single-luminophore pressure-sensitive paints the calibration changes with variations in temperature, requiring a new fit for each image. An example surface fit calibration can be

seen in Figure 35. While Figure 36 shows how the calibration is implemented to remove the temperature sensitivity from the PSP measurement. This calibration is implemented to find the coefficient of pressure for a representative steady run as seen in Figure 37. Historic data is also presented for comparison and is discussed fully in Section 7.1.

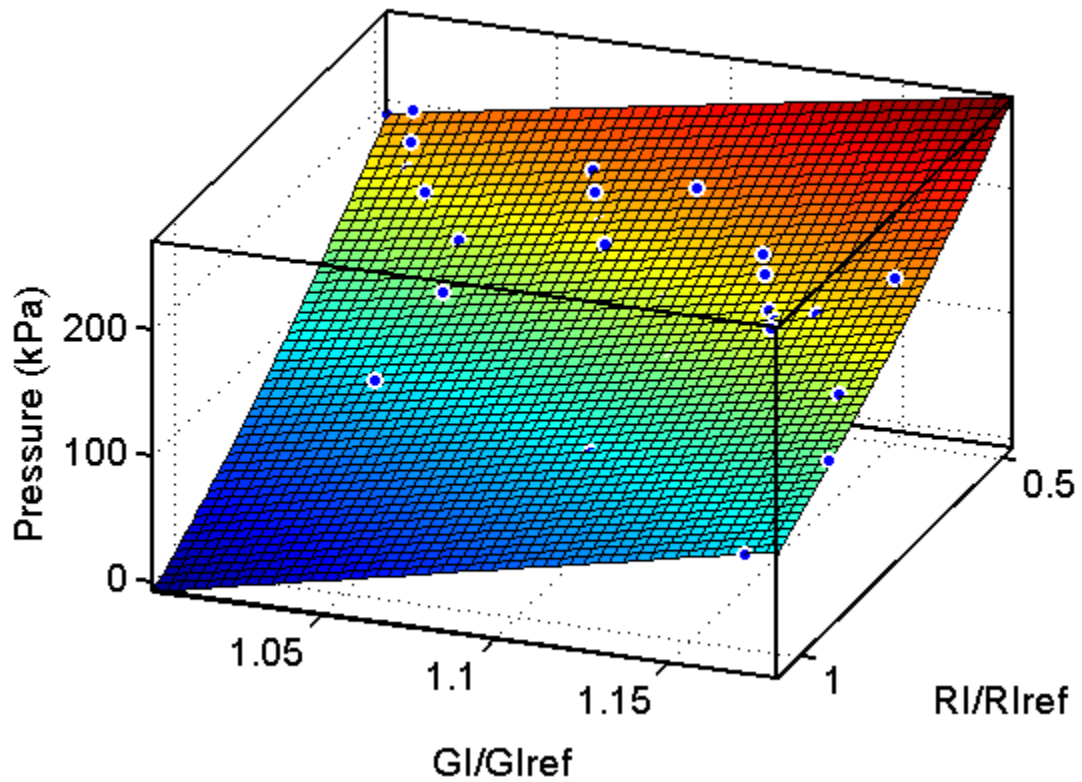


Figure 35: PSP *in situ* surface fit calibration for pressure vs. green and red intensity ratios

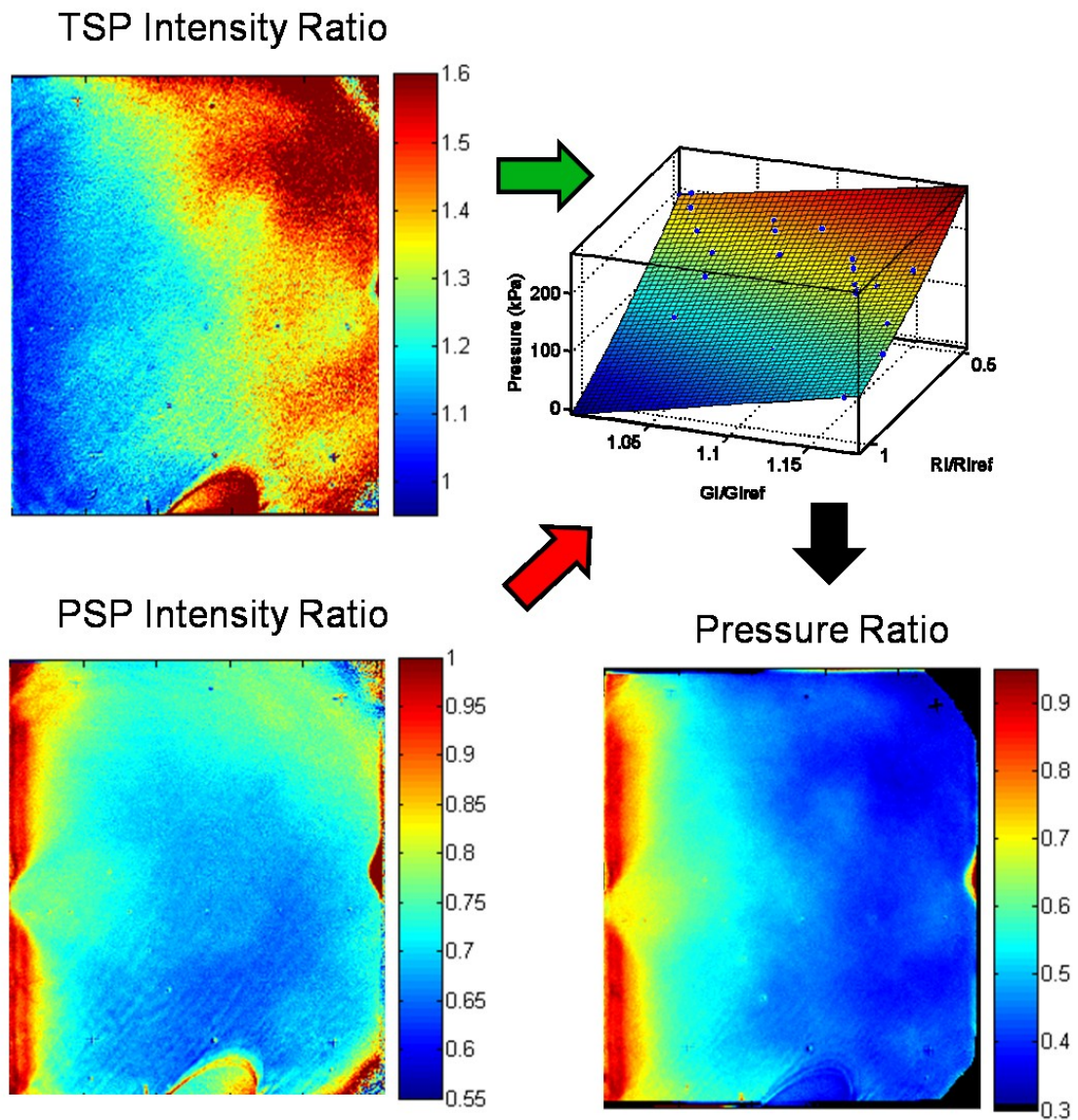


Figure 36: Schematic diagram of bi-luminophore pressure- and temperature-sensitive paint *in situ* pressure calibration

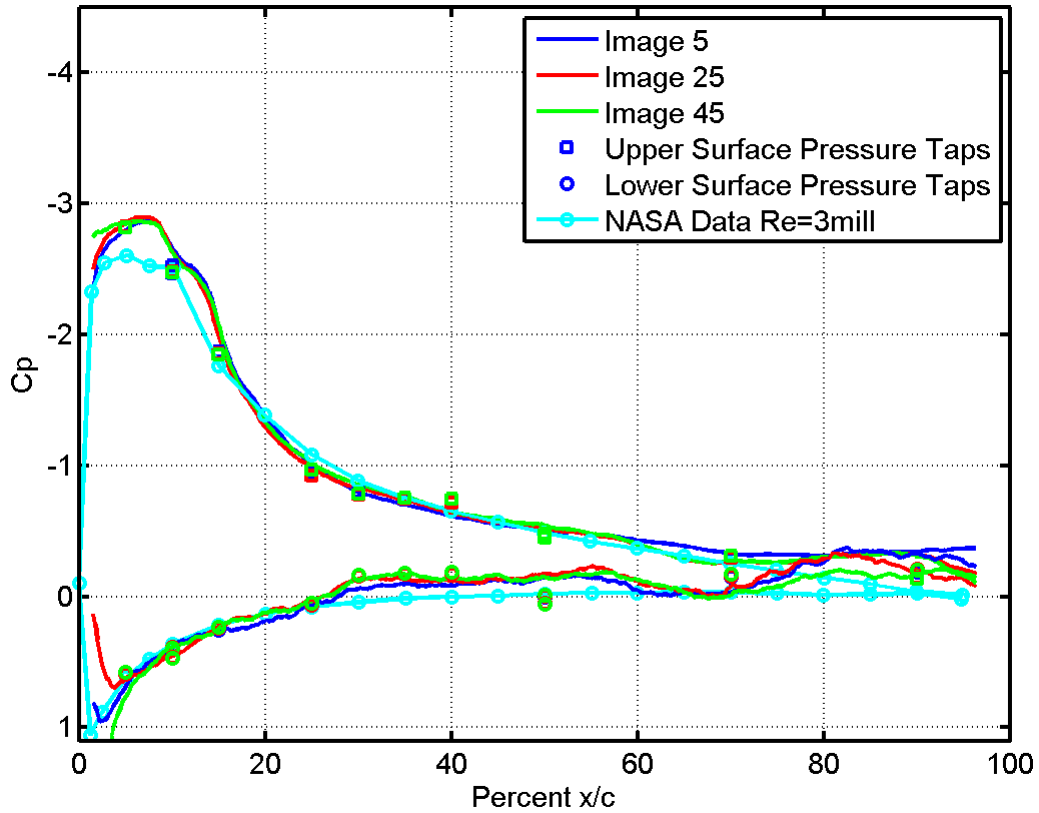


Figure 37: Three C_p profiles from calibrated PSP data of the NACA 0012 airfoil at $M = 0.6$, $\alpha = 9^\circ$ and $Re = 3.8$ million shown with a C_p profile of a NACA 0012 $M = 0.6$, $\alpha = 9^\circ$ and $Re = 3$ million

Section 6.5: Experimental Uncertainty

Several factors contribute to the PSP experimental uncertainty such as the pressure tap accuracy, model movement and deformations. PSP is also susceptible to variations in the illumination field which can occur from model movement through a non-uniform excitation light. This is minimized by rigidly affixing the cameras, beam

splitter, airfoil and LED arrays to the tunnel. Another source of illumination error is caused by variations in broad spectral noise from changes in ambient illumination intensities; these unwanted background illuminations are minimized by limiting the light entering through the tunnel windows by turning off the room lights or covering the window with a blackout curtain. However, due to the tunnel exhausting to the outdoors, some daylight enters the tunnel. This background illumination field, typically called the dark image, is recorded and subtracted from the wind-on and wind-off images. Only one set of background images is taken for each run and it is assumed that the ambient light does not change from the wind-on to wind-off images. Image registration between the green wind-on, green wind-off, red wind-on and red wind-off images is also a source of error due to the non-uniform pressure, temperature, luminophore thickness, and illumination. By incorrectly aligning all of the images these error effects can be exacerbated.

Section 6.6: Shock Location Measurement Techniques

PSP, TSP and PIV images have been acquired for different azimuthal locations, angles of attack (α), and Mach oscillation frequencies. Each image was interrogated to find the location of the shock. With the high spatial resolution of the pressure sensitive paint the shock location is found by taking the derivative of C_p with respect to x/c , $\frac{dC_p}{dx/c}$, and likewise the derivative of temperature with respect to x/c , $\frac{dT_f}{dx/c}$. The shock location

for PSP, PIV and TSP is thus found by locating the derivative extremum within the bounded neighborhood where a shock is expected, $3 < x/c < 30\%$, as expressed in Equation 9 and visualized in Figure 38.¹⁷ The reported shock position is the location where the shock strength was found to be at a minimum, though multiple pixels were found to be within the shock. In each case, a peak in the derivative is identified as the location of the shock. The automated data reduction techniques necessary to obtain meaningful shock location results for large data sets are presented in Appendices A through E.

Equation 9: Shock location equation.

$$Shock_Location = \min\left(\frac{dC_p}{dx/c}\right)$$

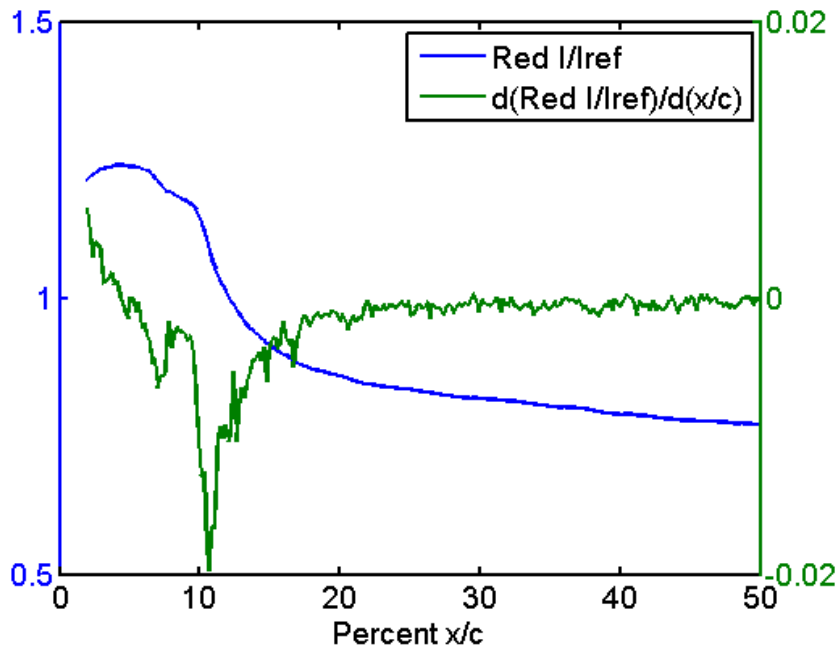


Figure 38: Example upper surface C_p profile and derivative of the C_p with respect to x/c

Figure 39 shows a representative suction-surface C_p distribution acquired using the single-shot, two-camera, temperature corrected, intensity-based PSP method; the shock location can be seen as the abrupt jump in C_p between -4 and -3 at $x/c = 13\%$. The shock location of the PSP and TSP images were analyzed along the centerline location, in order to match the PIV laser plane. Figure 39 shows a representative surface contour C_p map with the interrogation location seen as a black line. Figure 40 shows one phase of ensemble-averaged phase-locked PIV images. Note the PSP and PIV representative images are at two different test conditions. The black line marks the line of interrogation for the shock location; this measurement is made approximately 4 mm above the airfoil due to reflected laser light off the airfoil, giving erroneous vector fields close to the surface.³²

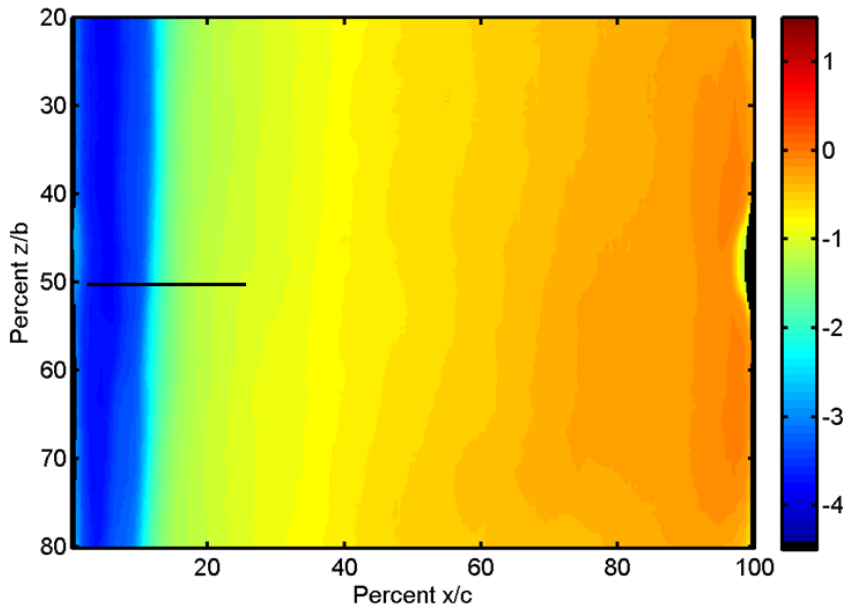


Figure 39: A representative suction surface C_p distributions of a NACA 0012 at $\alpha = 9^\circ$, $M = 0.55$ and $Re = 3.6$ million, flow is from left to right. The black line is where the shock location was searched for

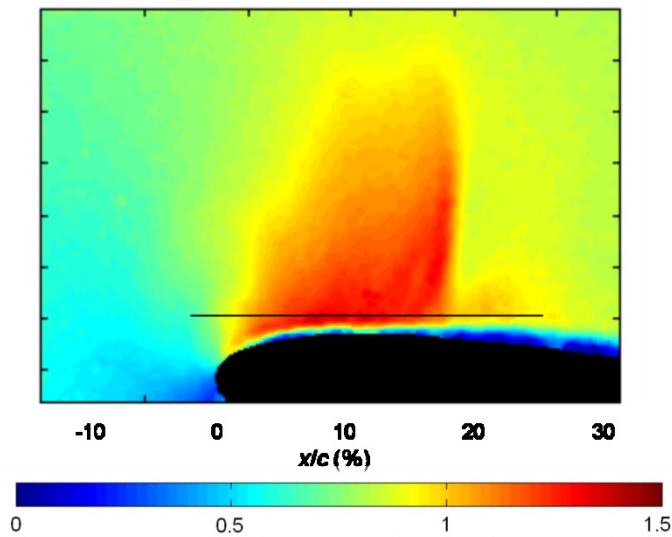


Figure 40: Contour of ensemble-averaged Mach number for one phase of a Mach oscillation period with $M = 0.6$, $\alpha = 9^\circ$ and $f = 9.5$ Hz. The black line is where the shock location was searched for³²

Chapter 7: Results

Section 7.1: Static Results

The NACA 0012 airfoil was tested at 9, 10 and 11 degrees angle of attack and at Mach numbers of 0.46, 0.55 and 0.61. These Mach numbers were selected to bound the unsteady data in order to make direct comparisons, while also at the same angles of attack. Additionally the $M = 0.61$ data at $\alpha = 10^\circ$ is in the buffeting regime and at an angle of attack of $= 11^\circ$ the airfoil is stalled. The corresponding Reynolds numbers varied between 3.4 and 4.4 million for the 0.127 m chord. The measurements from the bi-luminophore pressure- and temperature-sensitive paint were *in situ* calibrated to pressure and then converted into a coefficient of pressure using Equation 10. The C_p values were then converted to a normal (C_n) and axial force coefficients (C_a) by integrating along the airfoil chord as seen in Equation 11 and Equation 12. Further, the data was converted into sectional coefficient of lift (C_l), drag (C_d) and moment (C_m) by means of Equation 13 through Equation 15.⁵⁰ These calculations were performed only using the pressure forces and neglecting the friction forces on the airfoil. The results from these calculations are shown in Appendix F, Table 4.^{51, 52}

Equation 10: Coefficient of pressure

$$C_p = \frac{\left(\frac{p}{p_s} - 1\right)}{\frac{1}{2}\gamma M^2}$$

Equation 11: Normal force coefficient equation

$$C_n = \int_0^1 (C_{p,l} - C_{p,u}) d x/c$$

Equation 12: Axial force coefficient equation

$$C_a = \int_0^1 \left(C_{p,u} \frac{dy_u/c}{dx/c} - C_{p,l} \frac{dy_l/c}{dx/c} \right) d x/c$$

Equation 13: Sectional coefficient of lift equation

$$C_l = C_n \cos \alpha - C_a \sin \alpha$$

Equation 14: Sectional coefficient of drag equation

$$C_d = C_n \sin \alpha + C_a \cos \alpha$$

Equation 15: Sectional coefficient of moment equation about the quarter chord

$$C_m = \int_0^{0.25} (C_{p,l} - C_{p,u})(0.25 - x/c) dx/c - \int_{0.25}^1 (C_{p,l} - C_{p,u})(x/c - 0.25) dx/c$$

$$+ \int_0^1 \left(y_u/c C_{p,u} \frac{dy_u/c}{dx/c} - y_l/c C_{p,l} \frac{dy_l/c}{dx/c} \right) dx/c$$

Three representative C_p profiles are shown, Figure 41 through Figure 48, for each static test condition representing the data acquired at 10, 50, and 90% of the run duration. This effectively shows the C_p profile's insensitivity towards temperature, as the airfoil is cooled throughout the run. Pressure taps for all three C_p profiles are shown in the same color as the PSP data. The C_p data after the shock on the upper or suction surface should be trending in a straight line towards $C_p = 0$ as seen with the historical NASA data in Figure 37.

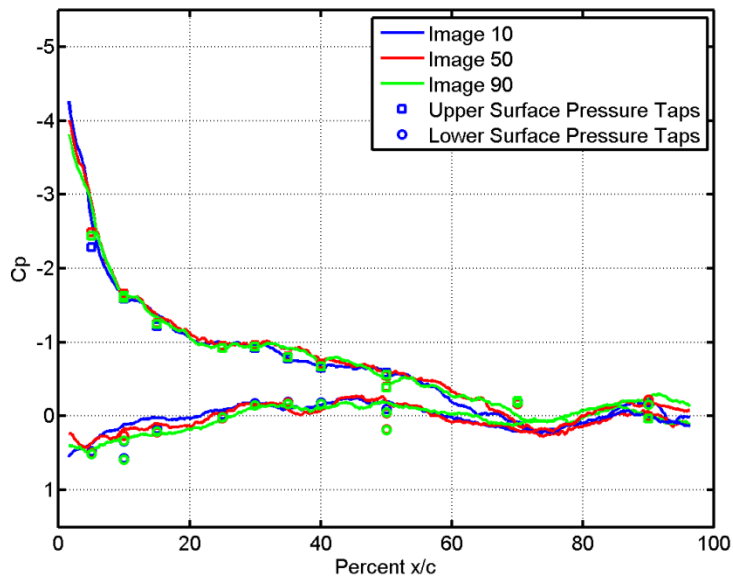


Figure 41: Three representative PSP C_p profiles of the NACA 0012 airfoil at $\alpha = 9^\circ$, $M = 0.46$ and $Re = 3.5$ million with pressure taps shown

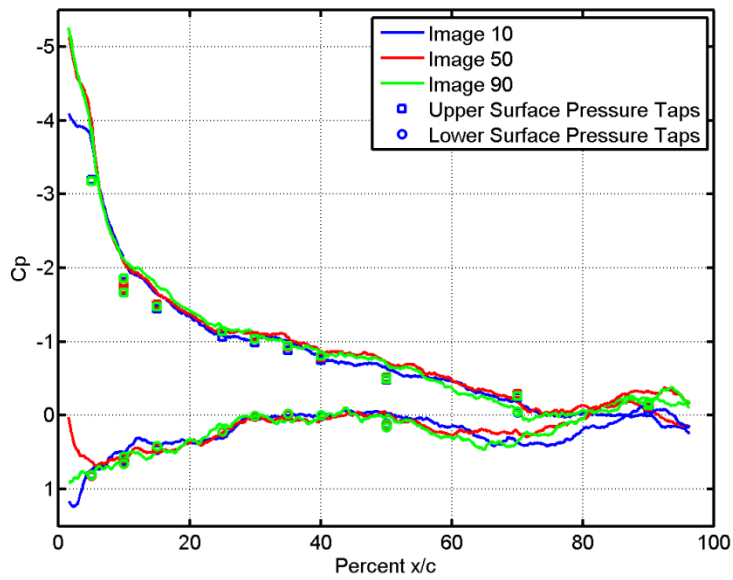


Figure 42: Three representative PSP C_p profiles of the NACA 0012 airfoil at $\alpha = 10^\circ$, $M = 0.45$ and $Re = 3.4$ million with pressure taps shown

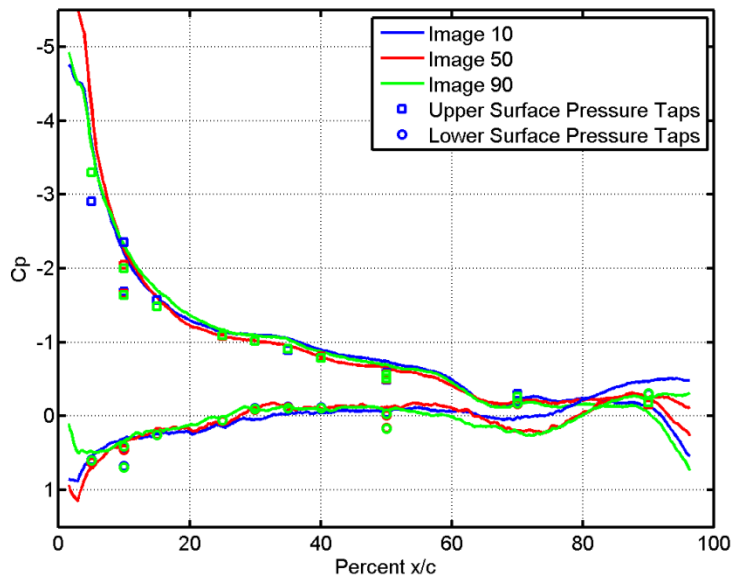


Figure 43: Three representative PSP C_p profiles of the NACA 0012 airfoil at $\alpha = 11^\circ$, $M = 0.45$ and $Re = 3.4$ million with pressure taps shown

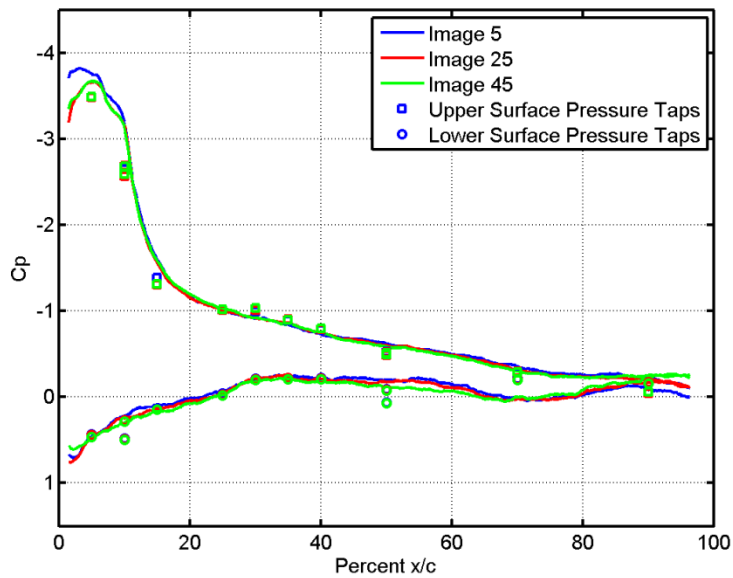


Figure 44: Three representative PSP C_p profiles of the NACA 0012 airfoil at $\alpha = 9^\circ$, $M = 0.55$ and $Re = 3.7$ million with pressure taps shown

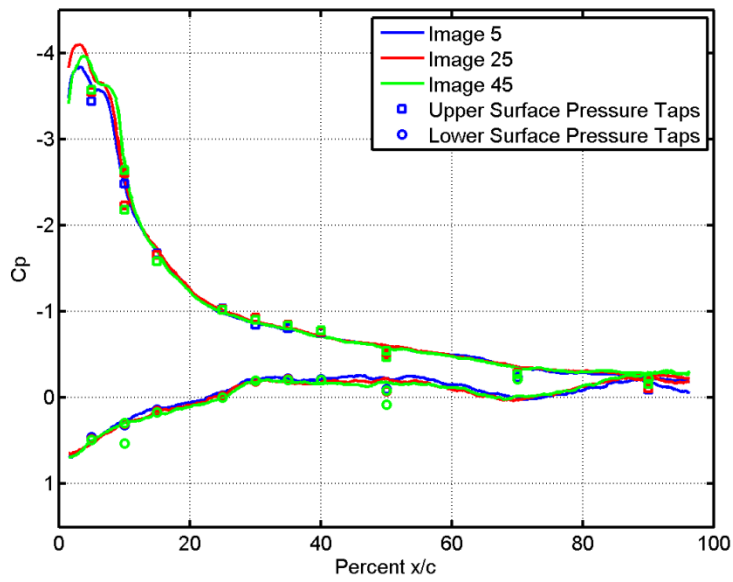


Figure 45: Three representative PSP C_p profiles of the NACA 0012 airfoil at $\alpha = 10^\circ$, $M = 0.55$ and $Re = 3.7$ million with pressure taps shown

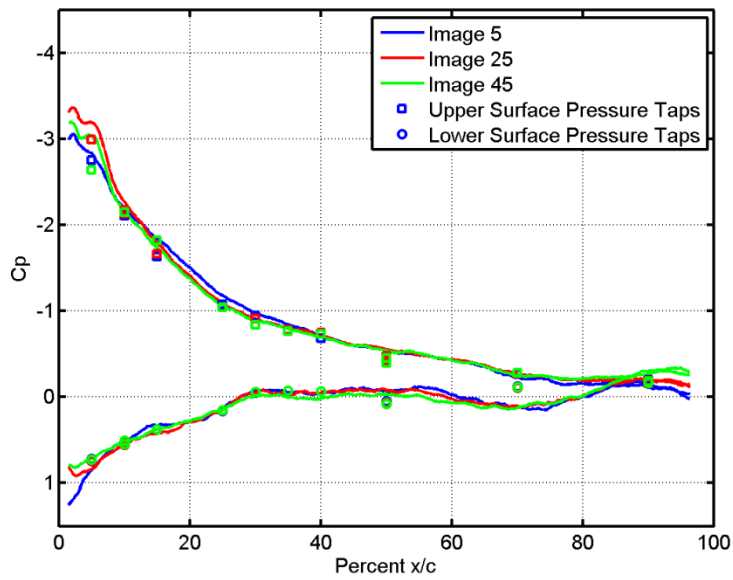


Figure 46: Three representative PSP C_p profiles of the NACA 0012 airfoil at $\alpha = 11^\circ$, $M = 0.55$ and $Re = 3.8$ million with pressure taps shown

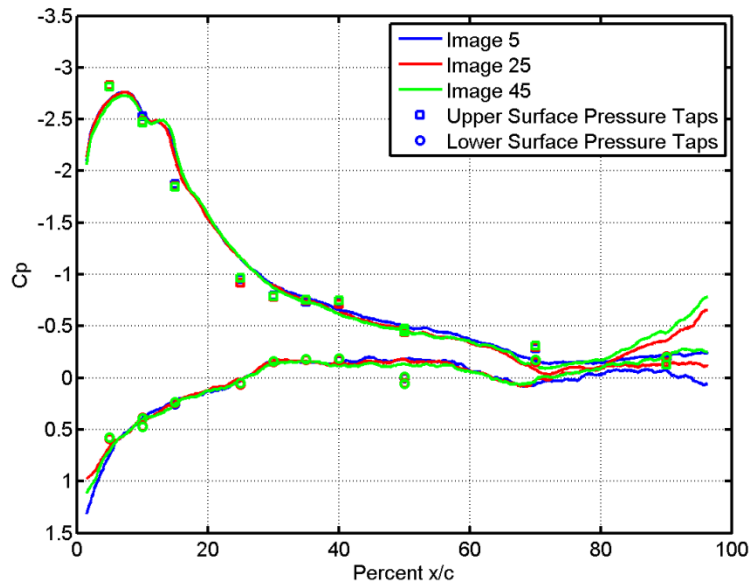


Figure 47: Three representative PSP C_p profiles of the NACA 0012 airfoil at $\alpha = 9^\circ$, $M = 0.61$ and $Re = 4.1$ million with pressure taps shown

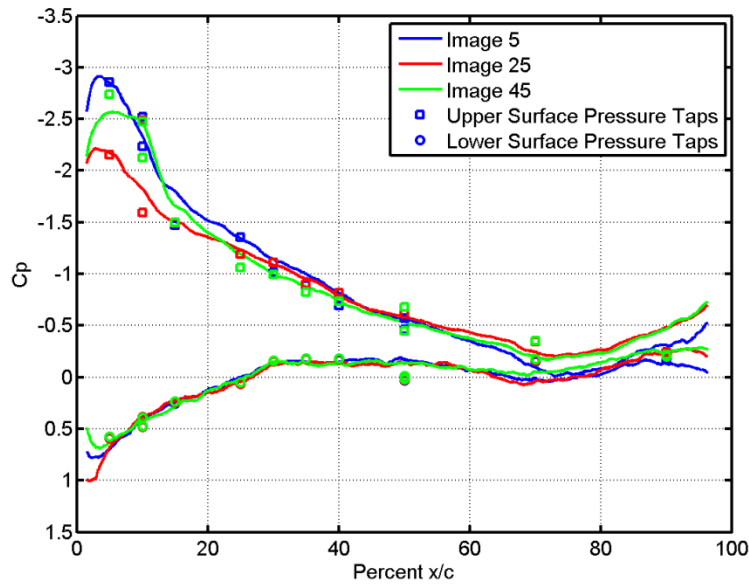


Figure 48: Three representative PSP C_p profiles of the NACA 0012 airfoil at $\alpha = 10^\circ$, $M = 0.61$ and $Re = 4.3$ million with pressure taps shown

The C_l , C_m , C_n and C_a were calculated for all 50 to 100 image pairs depending on the run. The standard deviation was then calculated for each set of data, in order to evaluate the precision error for each measurement technique. Similarly a direct comparison of the $M = 0.6$ PSP and NASA data is performed to evaluate the bias error in the measurement. At $M = 0.6$ and $\alpha = 9^\circ$, the PSP results give a $C_l = 0.882 \pm 0.022$ and $C_m = 0.015 \pm 0.012$ while the NASA data gives $C_l = 0.852$ and $C_m = 0.0232$. This results in a bias error of 3.5% and 89% for the C_l and C_m measurements respectively. The Coefficient of lift and moment vs. Mach number can be seen in Figure 50 and Figure 51 for all static test conditions, the raw data can be found in Appendix F as Table 4. It is expected that the coefficient of moment would have much higher errors than the coefficient of lift PSP measurements due to the error in trailing edge from lingering temperature effects and low SNR from ambient light. These effects can be seen in the C_p plots as waviness at $x/c > 70\%$. This waviness is due to the low illumination field at the trailing edge of the airfoil, as shown in Figure 49 where the ratio of background light to wind-off illumination reaches 14% at the trailing edge of the airfoil. Additionally the first few percent of the leading edge is difficult to measure measure/image for the negative angles of attack. The NASA Technical Memorandum data utilized a wake probe to calculate drag while the PSP data only accounts for pressure drag and not skin friction. Therefore it can be expected that the NASA and PSP values of C_d would differ substantially and as such are not presented.

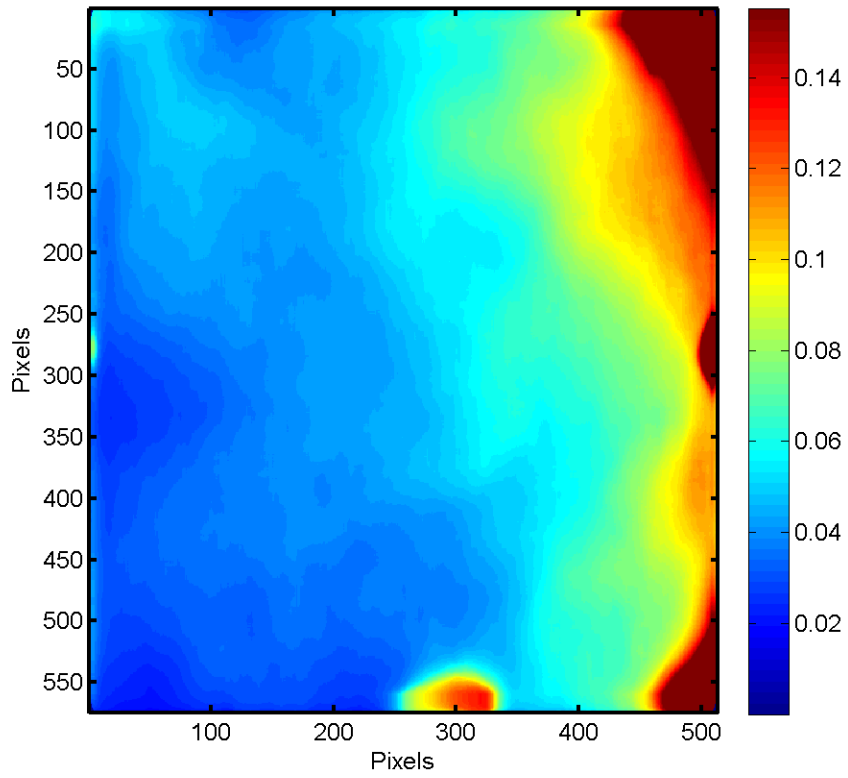


Figure 49: Dark image divided by wind-off, showing the large susceptibility to varying background illumination at the trailing edge

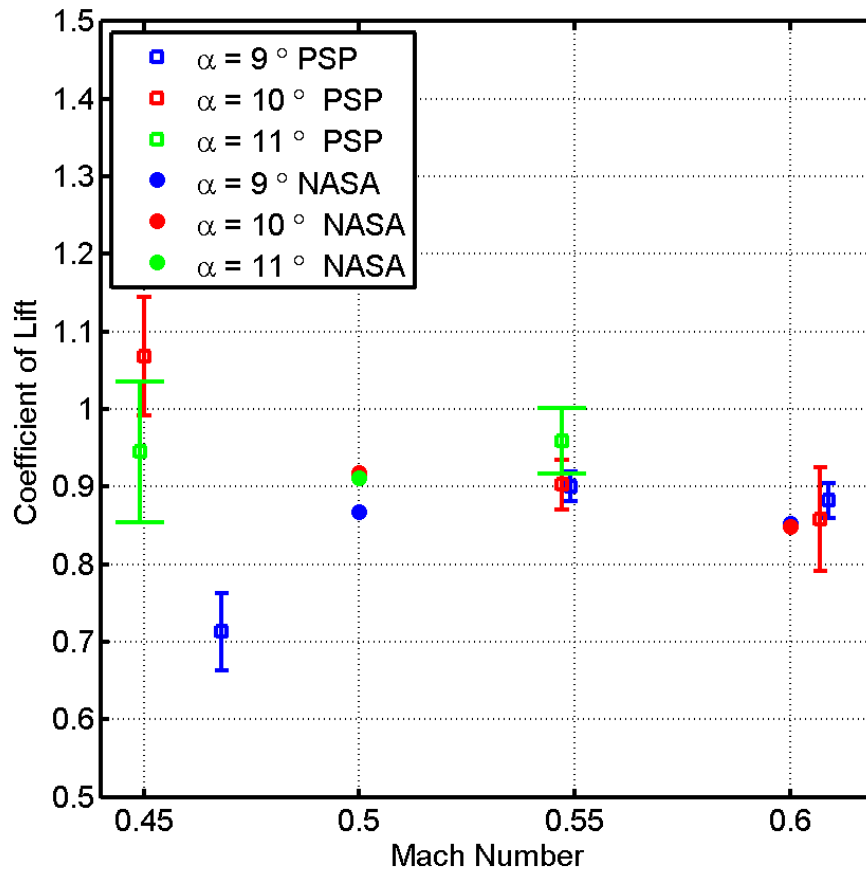


Figure 50: Coefficient of lift vs. Mach number for $\alpha = 9, 10$ and 11° , for both PSP and historical data

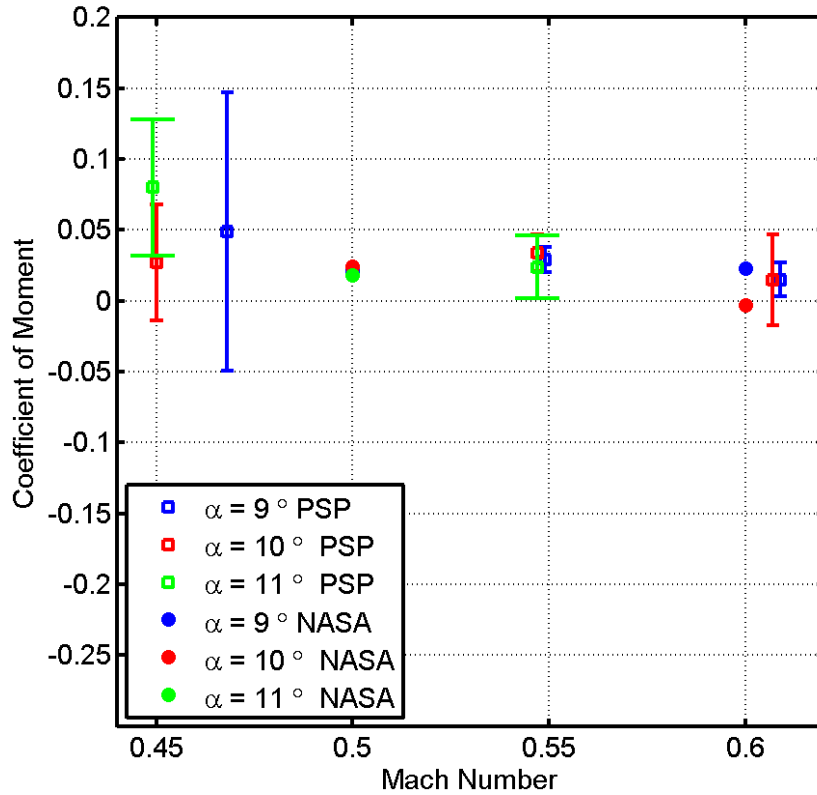


Figure 51: Coefficient of moment vs. Mach number for $\alpha = 9, 10$ and 11° , for both PSP and historical data

Section 7.2: Buffeting Results

The NACA 0012 airfoil is within the buffeting regime at the static tested condition of $\alpha = 10^\circ$ and $M = 0.61$, as seen earlier in Figure 48. This critical test condition demonstrates the utility of the bi-luminophore PSP to detect and track this highly unsteady, three-dimensional phenomenon. Figure 52 shows 9 representative upper surface C_p maps for $0\% < x/c < 60\%$ and $20\% < z/b < 80\%$. These successive images, left

to right and then top to bottom, show the highly 3D nature of the flow. These bi-luminophore images had an exposure time of 5.5 ms for both the green and red channels and were acquired at a rate of 28 Hz. While the PSP's frequency response has been characterized to be greater than 5 kHz, the technique is limited by the duration needed to adequately record the emission intensity signals. The single-shot unsteady PSP method is pivotal to measuring this highly dynamic phenomenon. Any non-phase-locked PSP techniques would have averaged out this fluid dynamic phenomenon, if the single-shot technique was not utilized.

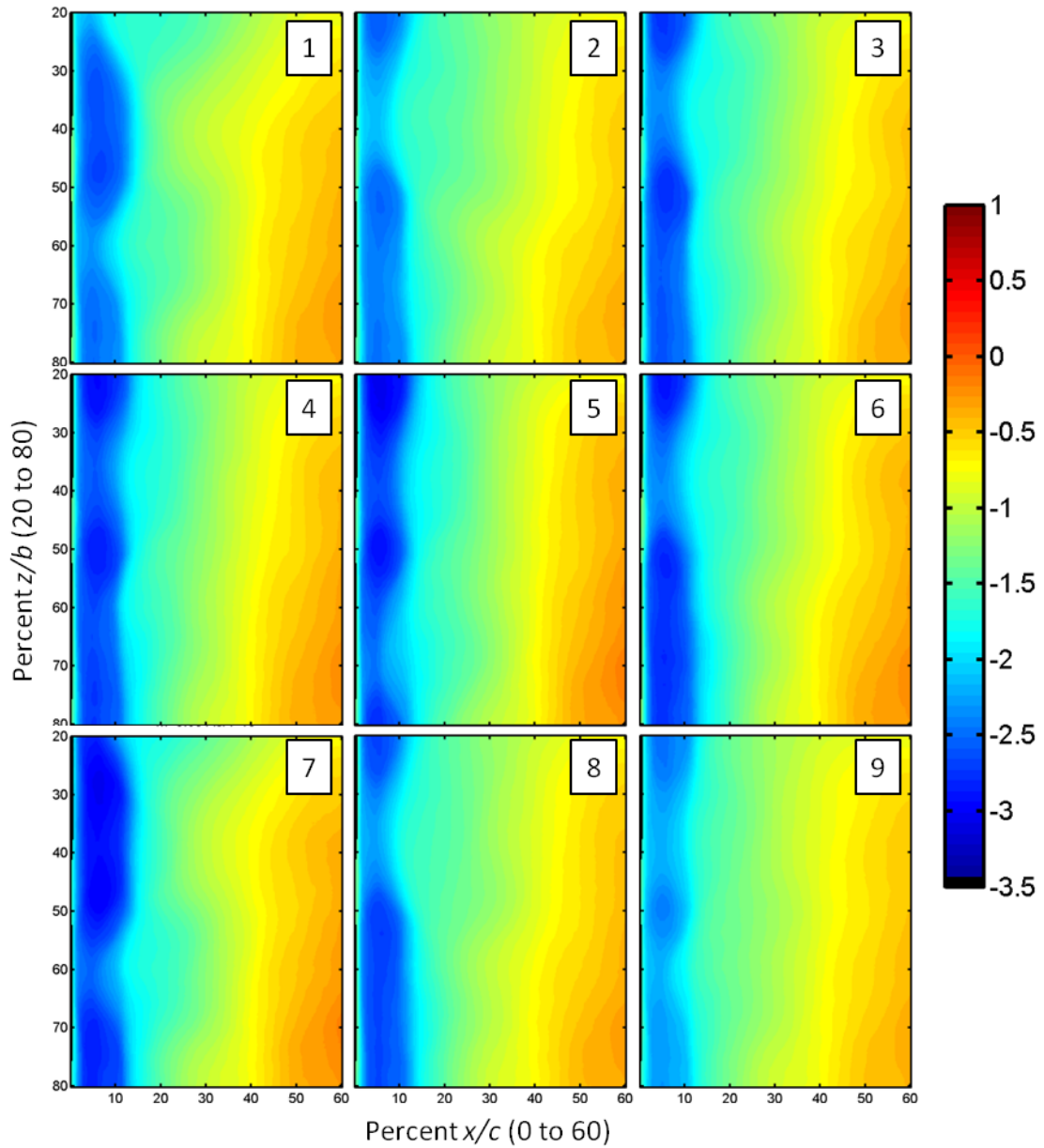


Figure 52: 9 upper surface Cp maps of the NACA 0012 airfoil at $\alpha = 10^\circ$, $M = 0.61$ and $Re = 4.2$ million for $0\% < x/c < 60\%$ and $20\% < z/b < 80\%$ during a steady run in the buffeting regime

Section 7.3: Dynamic Results

In addition to the static testing, the NACA 0012 airfoil was tested at a variety of low-reduced-frequency Mach oscillation rates and angles of attack, as seen in Table 3. The mean Mach number was utilized to find the reduced frequency for the unsteady data. The objective of this research was to evaluate the shock movement in conjunction with the coefficient of lift, moment and drag hysteresis curves for each angle of attack and frequency. It was not possible to obtain accurate pressure distributions on the airfoil due to the lack of unsteady pressure transducers for an adequate *in situ* calibration, in conjunction with the poor quality of the *a priori* calibration. Therefore, the unsteady data is limited to unsteady shock location determination between the PSP, TSP and PIV in addition to qualitative analysis of the fluid dynamic phenomenon.

Table 3: Unsteady test matrix

Oscillation Frequency (Hz)	Reduced Frequency	Angle of Attack (°)
21	0.050	9, 10 and 11
15.25	0.037	9, 10 and 11
9.5	0.023	9, 10 and 11
2.1	0.005	9, 10 and 11

The Mach oscillation waveforms were correlated to azimuthal angle by performing a cross correlation of the data to align with a sinusoidal waveform which has a maximum Mach number at $\Psi = 90^\circ$. This was done to enable a direct comparison between oscillation frequencies, due to the varying phase shift with frequency, as discussed in Section 3.2. The azimuthally aligned data can be seen in Figure 53 through

Figure 55 corresponding to $\alpha = 9, 10$ and 11° respectively, with each data point corresponding to the Mach number at each PSP image. The maximum frame rate for both cameras was 28 Hz for these tests, thus Figure 53 through Figure 61 are a compilation of multiple oscillations periods. Due to the addition of an airfoil in the tunnel the Mach oscillation waveform was shifted from the empty test section waveforms (see Section 3.2). This shift is due to the change in the cross sectional area in the test section, A_t . This effect can be seen in Figure 53 through Figure 55 as a bulk shift in the Mach oscillation waveforms due to the change in angle of attack from $\alpha = 9$ to 11° . The bulk shift was down which is counter-intuitive to the Mach - area equation, Equation 1. This is possibly due to the static pressure transducer being too close to the airfoil. Additionally with the pressure transducer being located upstream of the airfoil, the cross sectional area is slightly increased thereby emulated a lower Mach number.

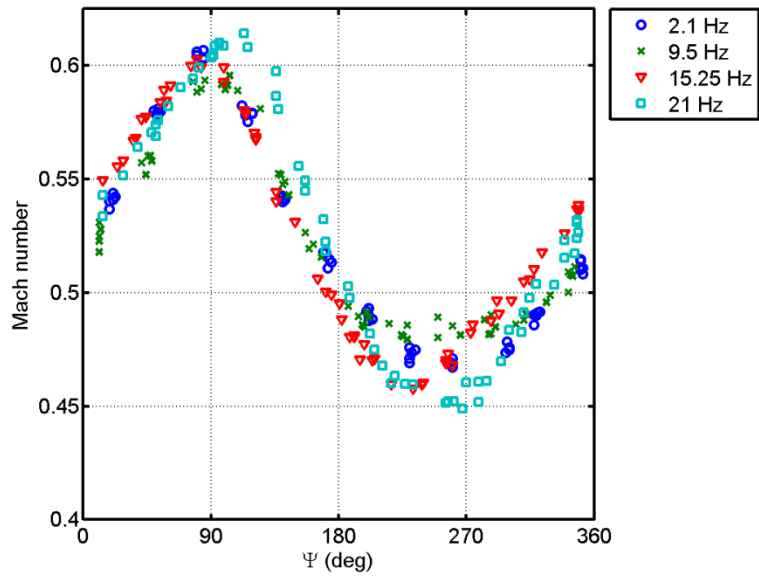


Figure 53: Mach number vs. Phase for the 4 frequencies at $\alpha = 9^\circ$

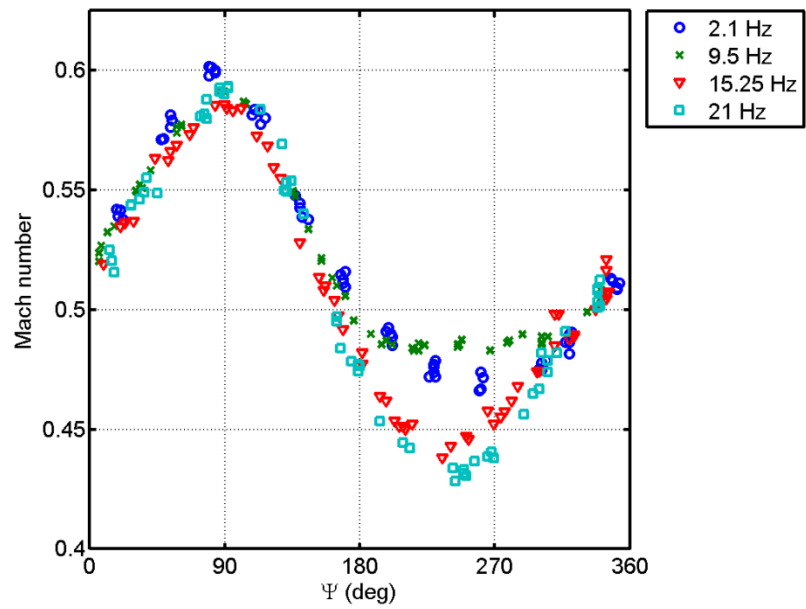


Figure 54: Mach number vs. Phase for the 4 frequencies at $\alpha = 10^\circ$

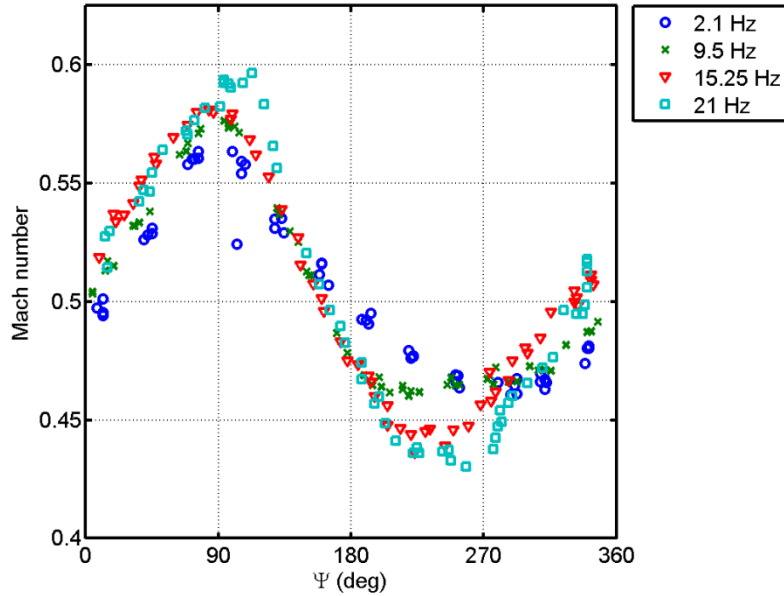


Figure 55: Mach number vs. Phase for the 4 frequencies at $\alpha = 11^\circ$

The Mach oscillation's effect on the shock location was found to have a significant phase delay associated with the frequency. This effect can be seen as a growth in hysteresis in Figure 56 with an increase in frequency. This phenomenon was also measured with unsteady Schlieren images by Fernie and Babinsky at similar low reduced frequencies on the NACA 0012.^{17, 18} For the high frequency Mach oscillations at $\alpha = 9^\circ$, the retreating shock is found to lag the advancing shock, Figure 56. The hysteresis effect is due to the instantaneous Mach number varying and the fluid dynamic phase lag of the shock location. The start of the schematic directional loops in this figure correspond to $\Psi = 0^\circ$ and represents the advancing blade through $\Psi = 180^\circ$ while $\Psi = 180^\circ$ through 360° correspond to the retreating blade. The $\alpha = 10^\circ$ data, Figure 57, is interesting when compared to the steady data, for which the $M = 0.61$ data was found to be buffeting while the $M = 0.55$ was steady attached flow. It can be seen that at all frequencies at and above

$M = 0.55$ the shock is buffeting, however as the frequency increases the steady-to-buffeting transition occurs at lower Mach number. It is hypothesized that the forced freestream flow causes the turbulent boundary layer to breakdown into a buffeting flow more rapidly. Figure 58 shows a continuation of this aperiodic trend with even the low Mach numbers exhibiting cycle-to-cycle variations in the shock location. Figure 59 through Figure 61 illustrate this phenomenon as shock location vs. azimuth angle, where it is seen that the shock location is very steady at the retreating blade angles around $\Psi = 270^\circ$, where the Mach number is lower.

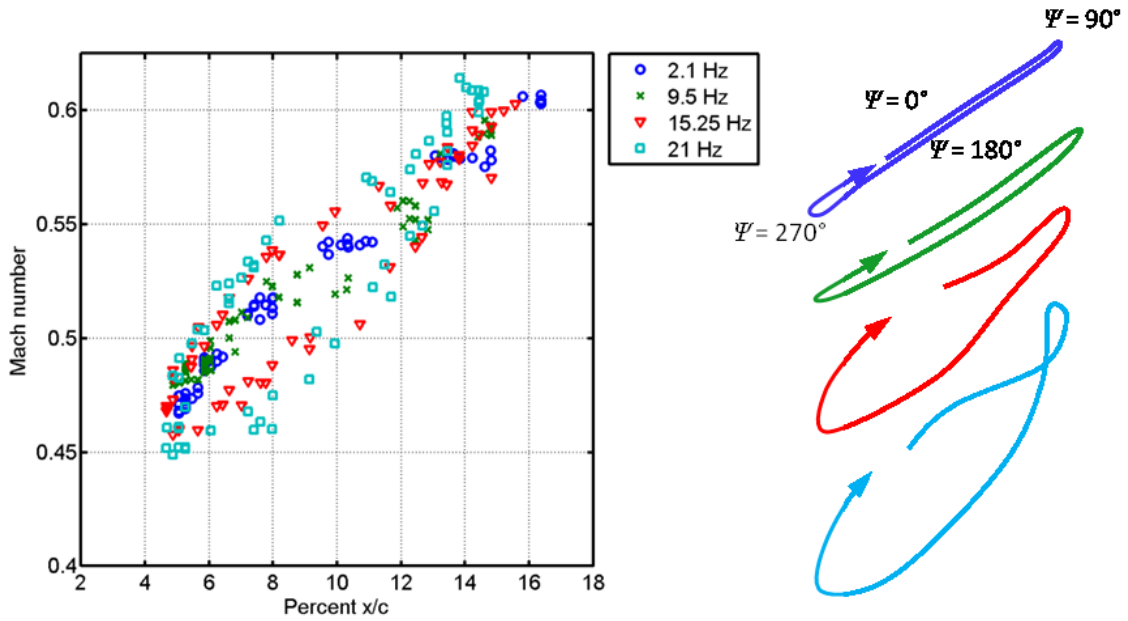


Figure 56: Mach number vs. Shock Location for the 4 frequencies at $\alpha = 9^\circ$, with hand drawn schematic directional loops of the oscillations starting at $\Psi = 0^\circ$

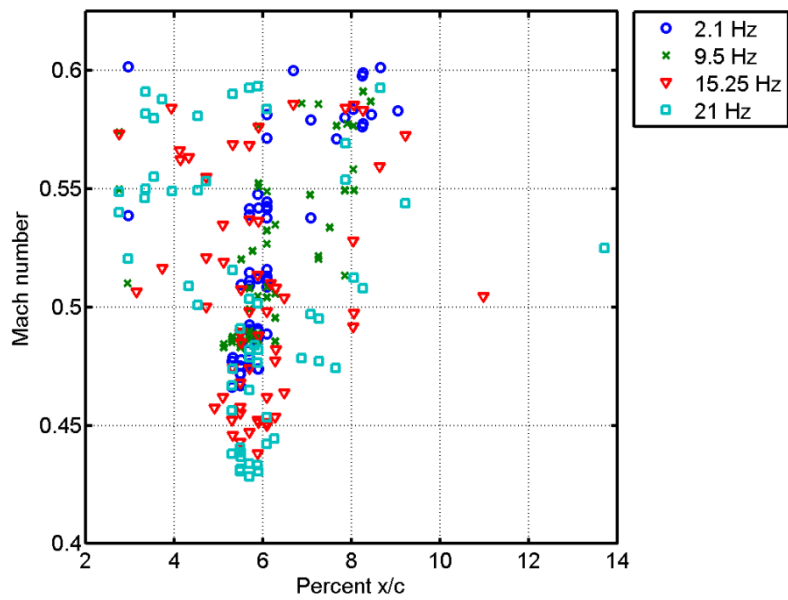


Figure 57: Mach number vs. Shock Location for the 4 frequencies at $\alpha = 10^\circ$

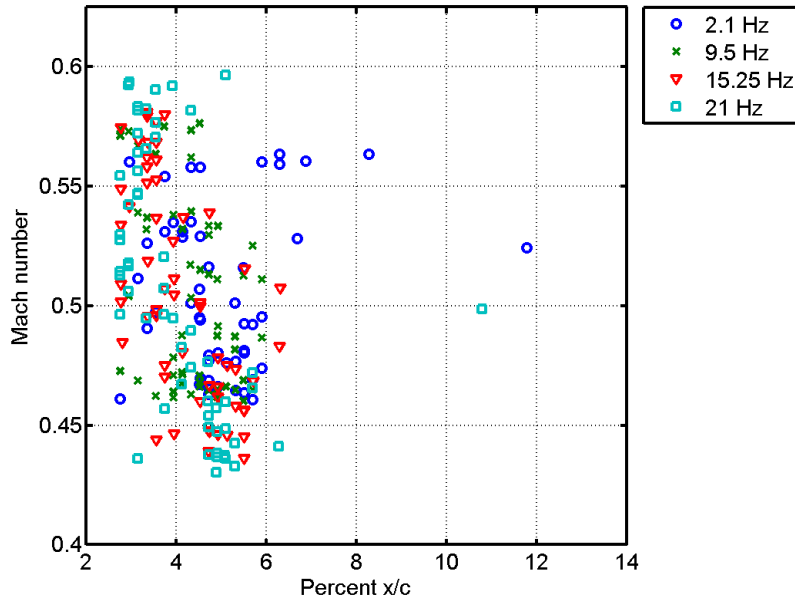


Figure 58: Mach number vs. Shock Location for the 4 frequencies at $\alpha = 11^\circ$

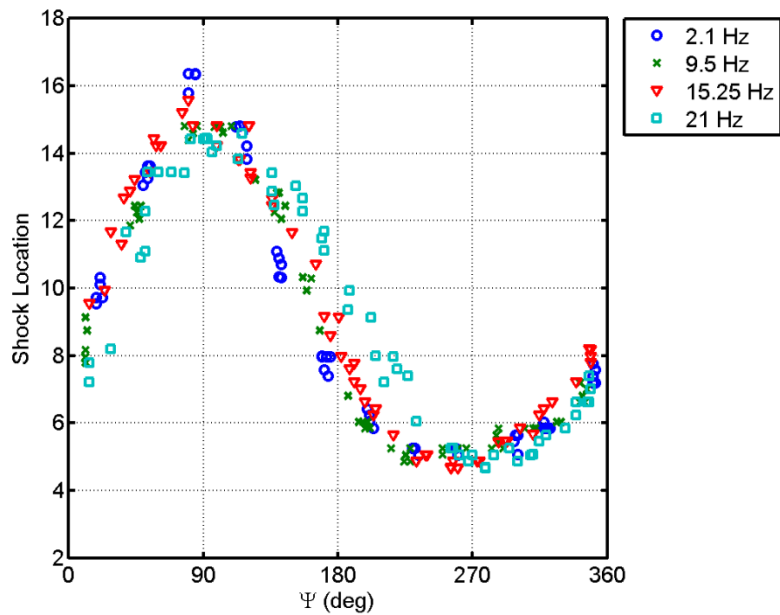


Figure 59: Shock Location vs. Phase for the 4 frequencies at $\alpha = 9^\circ$

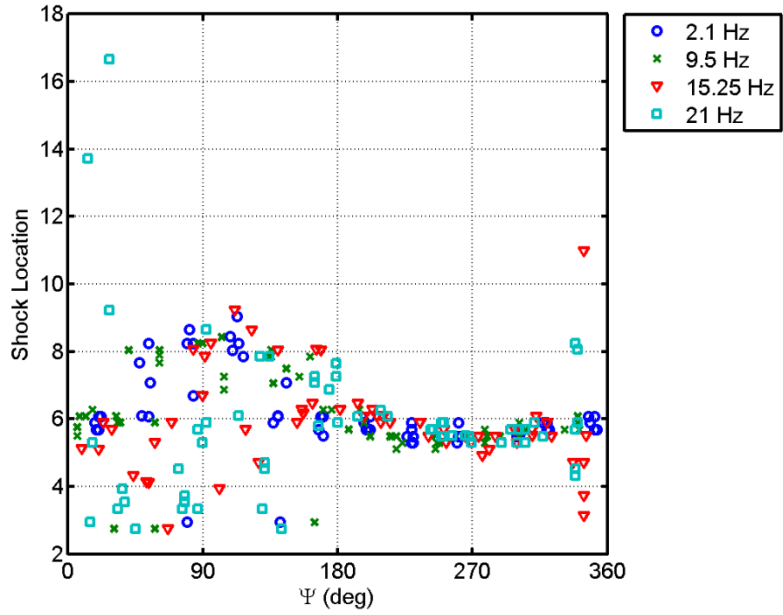


Figure 60: Shock Location vs. Phase for the 4 frequencies at $\alpha = 10^\circ$

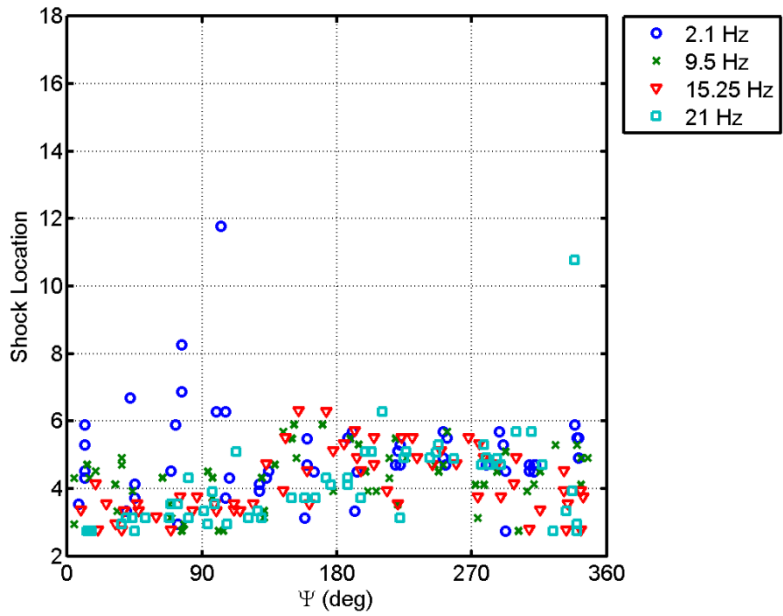


Figure 61: Shock Location vs. Phase for the 4 frequencies at $\alpha = 11^\circ$

The buffeting regime was further investigated for the oscillatory flow tests with PSP and PIV. Four phase-locked, $\Psi = 93^\circ$ and $f = 9.5$ Hz, PIV and PSP images are shown at $\alpha = 9^\circ$ in Figure 62, which is below the buffeting regime and in the buffeting regime at $\alpha = 10^\circ$ as seen in Figure 63. The PSP and PIV images are 4 representative images of the same tunnel conditions and azimuth position taken during different runs to show the periodic or aperiodic nature of the flow. It is shown that the $\alpha = 9^\circ$ results are highly repeatable with both the on- and off-body measurement techniques. The higher, $\alpha = 10^\circ$ images show an aperiodic phenomenon similar to that seen in the PSP buffeting results. The 2D PIV results exhibit variations in the shock strength and location while the PSP results show this phenomenon to be three dimensional in nature, similar to what was encountered in the steady-flow buffeting results.

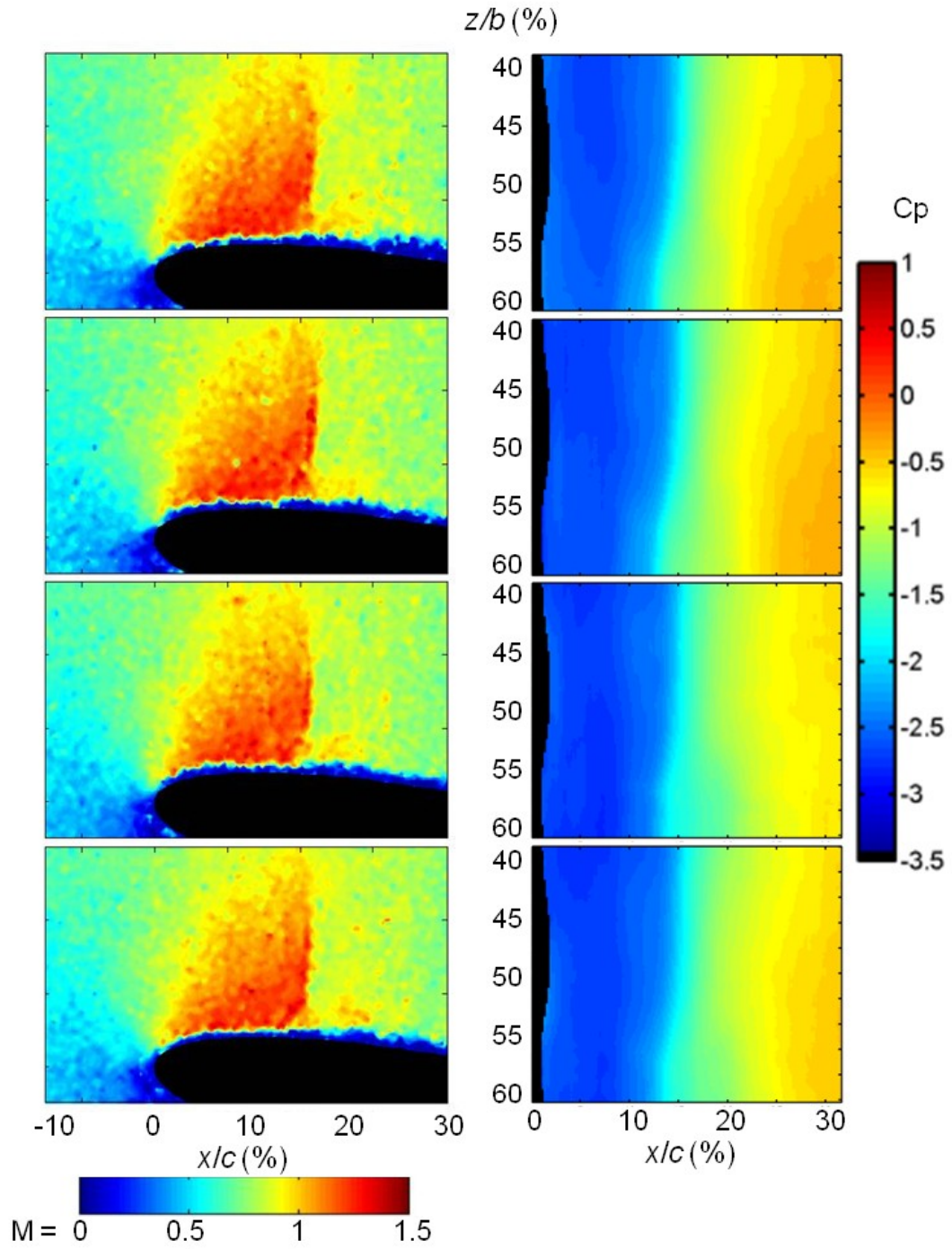


Figure 62: Four representative phase locked images, $\Psi = 93^\circ$, of PIV and PSP results at 9.5 Hz, $\alpha = 9^\circ$ and $M = 0.59$ showing a steady shock location⁴⁸

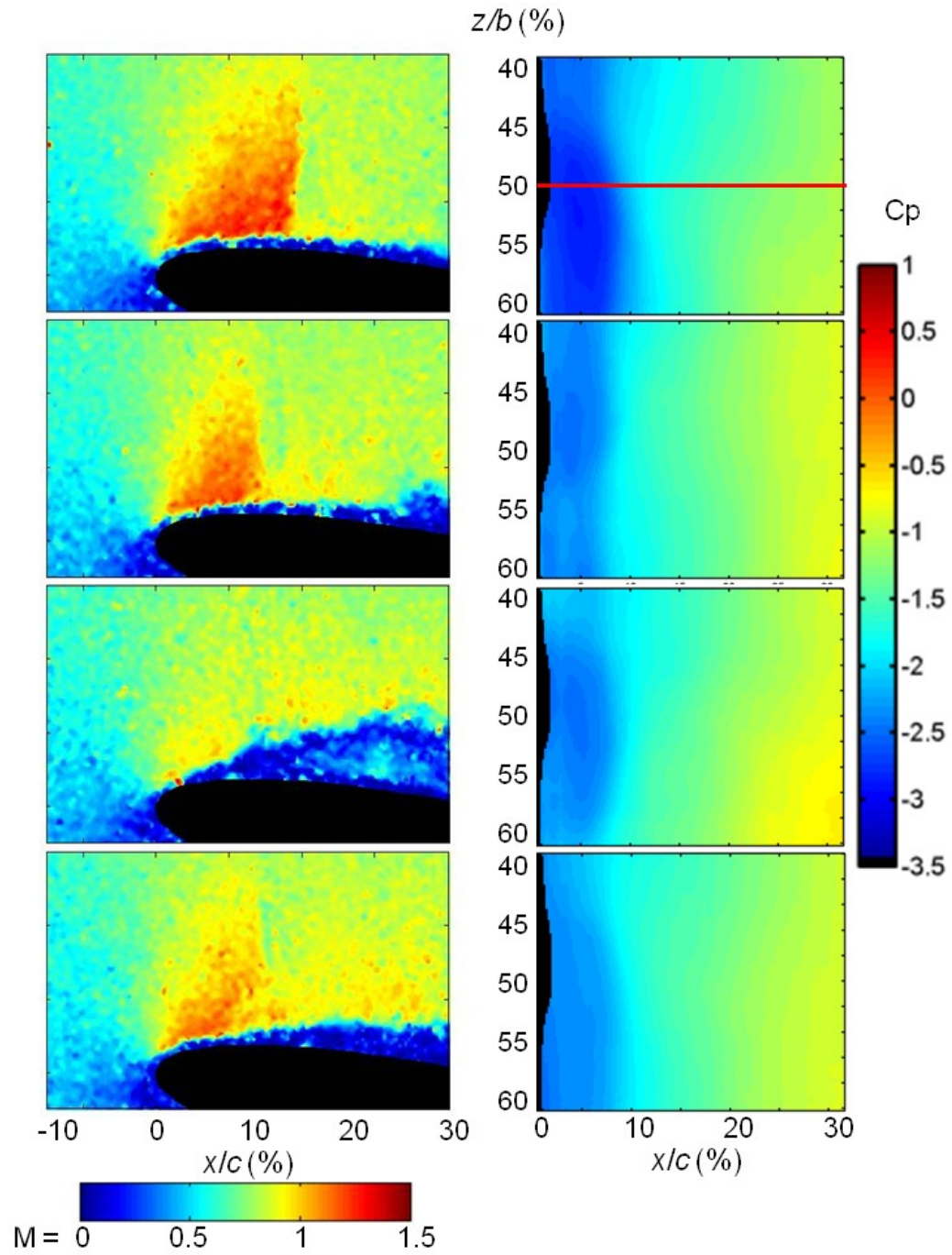


Figure 63: Four representative phase locked images, $\Psi = 90^\circ$, of PIV and PSP results at 9.5 Hz, $\alpha = 10^\circ$ and $M = 0.59$ showing an unsteady shock location⁴⁸

Due to the length and number of tunnel runs needed to obtain 100 images the PIV data has only been recorded for one full set of Mach oscillation phases at one frequency. This set of ensemble-averaged PIV images for 12 phases of a Mach oscillation was taken at $\alpha = 9^\circ$ and $f = 9.5$ Hz and can be seen in Figure 64. This shows the off-body forces of the Mach oscillation progressing from a strong to weak shock.

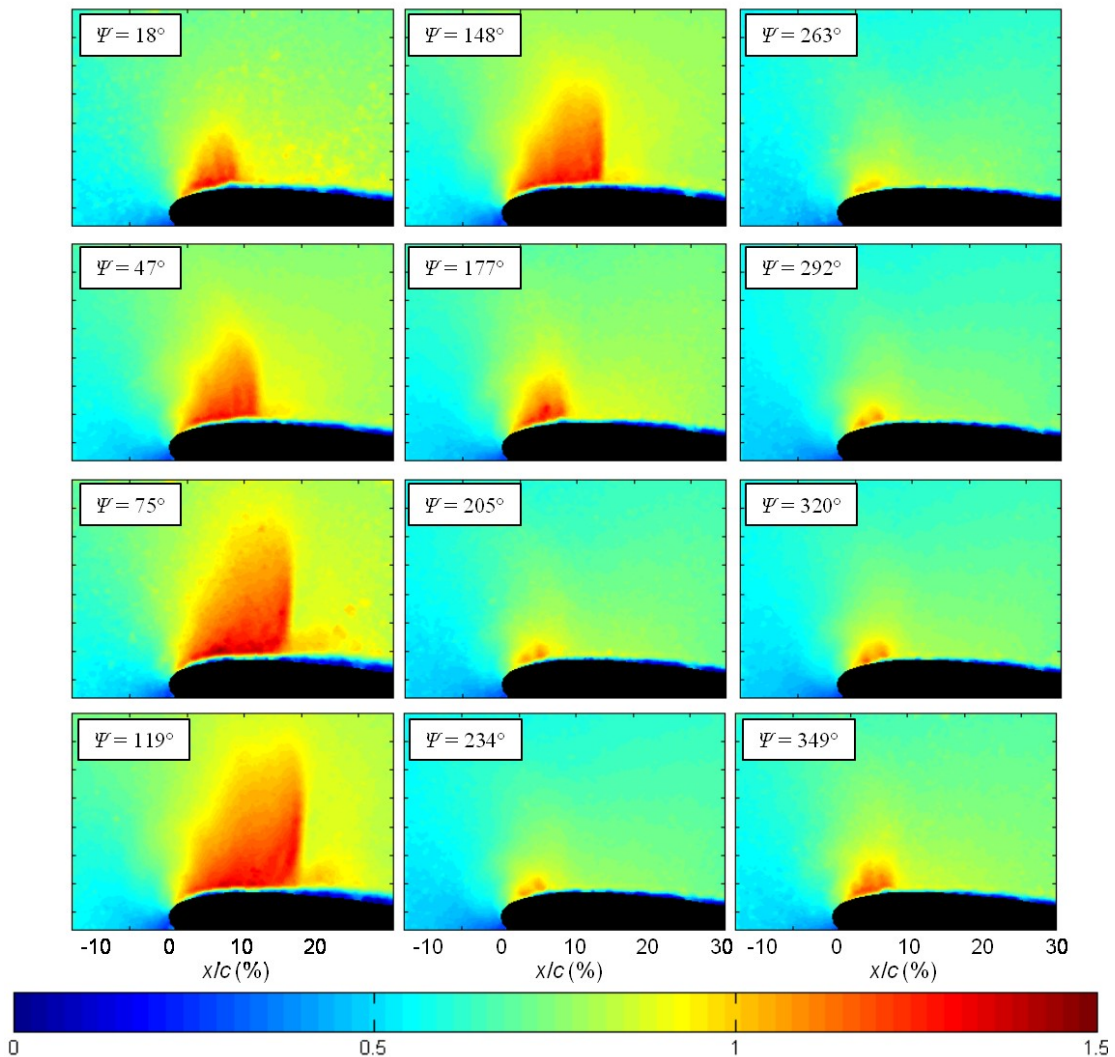


Figure 64: Contours of ensemble-averaged Mach number for 12 phases of a Mach oscillation period with $\alpha = 9^\circ$ and $f = 9.5$ Hz³²

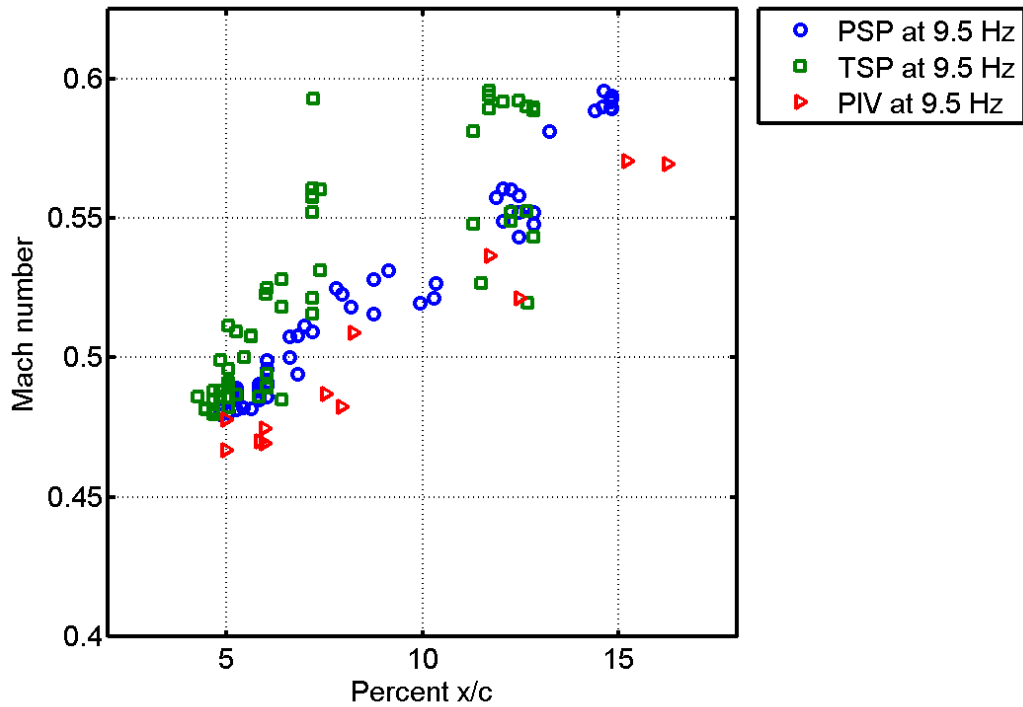


Figure 65: Mach number vs. Shock location for PSP, TSP and PIV at $f=9.5$ Hz and $\alpha=9^\circ$

The spatial resolution of the PSP and TSP measurements of shock location was $0.125\% x/c$ while PIV had a slightly lower resolution of $0.33\% x/c$. The TSP measurement was taken from the reference channel emission (Perylene and laser dye mixture) for the PSP temperature compensation. A direct comparison of the shock detection results are shown in Figure 65 for the one Mach oscillation frequency tested with all three measurement techniques (PIV, PSP, and TSP). It can be seen that the PSP and PIV both show the same trend while TSP is very erroneous in tracking the instantaneous shock location; the TSP measures the solid aluminum airfoil surface temperature and not the shock location which are tenuously linked due to the effects of heat conduction. The PIV measurement is seen to be shifted to a higher chordwise

location at higher Mach numbers due to the measurement taken at 4 mm above the airfoil surface along with the shock curving back to an aft position as it increases in height. Hysteresis effects are particularly evident where shock strength is shown to be dependent upon whether the freestream is accelerating or decelerating. This hysteresis is observed at a low value of reduced frequency (0.037), which is normally considered to be quasi-steady.³¹ This is possible due to the ability to measure the shock location with greater accuracy, thereby detecting smaller unsteady effects.

Chapter 8: Conclusions

Section 8.1: Summary of Experimental Results

A bi-luminophore unsteady-pressure- and temperature- sensitive paint was used in conjunction with a new two-camera technique to study the steady and unsteady characteristics of shock motion on the NACA 0012 airfoil. In an initial study a single-shot, lifetime-based, unsteady pressure-sensitive paint method was utilized to study the shock motion of a NACA 0021 airfoil. This method effectively resolved the unsteady standing shock wave on the airfoil. However, due to temperature non-uniformity in the wind-off images and temporal gradients in the wind-on images, the trailing edge C_p profile could not accurately be resolved. For this reason the single-shot intensity-based technique with a bi-luminophore fast pressure-paint was investigated for use in this tunnel. The high spatial resolution of PSP, TSP and PIV measurements allowed for high accuracy of shock location capture. The single-shot PSP technique allows high accuracy in the chordwise and spanwise direction allowing for the capture of aperiodic 3D fluid dynamic phenomenon, such as buffeting. If a phase averaged technique were implemented these aperiodic fluid dynamic features of the flow would have been lost to cyclic averaging. It was found that these perturbations in shock location are not 2D for a 2D airfoil section. Bi-luminophore pressure-sensitive paint has demonstrated the

capability to produce high-resolution data with the new two-camera single-shot intensity-based technique. Standard aerodynamic forces (C_n , C_a , C_l and C_m) were computed for only the steady runs, due to the lack of adequate calibration techniques for the unsteady results. Techniques and practices to alleviate these errors are discussed in Section 8.2. The steady forces were compared to similar NACA 0012 historical data. It was found that the PSP was able to measure the sectional coefficient of lift with high accuracy and precision. The errors of the PSP measurements were found to be 3.5% and 89% for the C_l and C_m measurements, respectively. Much higher errors were found with the coefficient of moment measurement due to the errors in the trailing and leading edges. The erroneous pressure forces at the leading and trailing edges were exacerbated by their large moment arm relative to the quarter chord location. Additionally, the error seems large due to the small values of C_m for a symmetric airfoil.

The airfoil was tested in the buffeting regime at one steady condition. The shutter of the camera was open for approximately one third of the buffeting period as compared to historical buffeting studies. Additionally the buffet frequency was higher than the Nyquist frequency of the pressure taps. In order to fully study the three dimensionality of this phenomenon an optimized in-depth study is needed. This would consist of shorter duration camera shutters through the use of more excitation illumination and a high frequency transducers surface mounted on the airfoil for accurate *in situ* pressure calibration. However, the bi-luminophore PSP single-shot technique is uniquely suited to make these 3D aperiodic measurements.

Section 8.2: Recommendations for Obtaining Accurate Unsteady Cp Data Using PSP

Several experimental setup techniques were employed to minimize error. Theoretically it is possible to perform and implement an *a priori* calibration to obtain the surface pressure data; however, in practice this calibration is done on a coupon and not the tested airfoil. This leads to variations in the illumination field, luminophore concentration and camera settings between the *a priori* calibration coupon and the tested airfoil. These effects are minimized by taking the ratio of the wind-off and wind-on images, but they are not eliminated entirely due to registration errors or model deformation and introduce errors into the measurement technique. Therefore, in practice *in situ* calibrations are almost always used, which require accurate pressure measurements at all testing conditions. It is due to the lack of unsteady surface mounted pressure transducers that unsteady coefficient of lift and moment plots cannot be presented in this work. For bi-luminophore paint the best calibration will arise from the thermistors and pressure taps being spread in the temperature and pressure regime tested, thus minimizing any extrapolation errors in the calibration implementation. It was found that the intensity of the ambient light changed between the wind-on and wind-off images due to variations in the light entering the exhaust of the wind tunnel. The changing dark or ambient illumination field could be accounted for by using a double-shutter CCD camera in conjunction with the intensity-based PSP measurement, using Gate 1 for the intensity-based PSP measurement and Gate 2 as a dark reference image. The dark image would thus be separated from the wind-on or wind-off image on the order of a millisecond instead of tens of seconds with the traditional technique.

The two-camera technique provided immense flexibility optimizing the intensities of both paints simultaneously. If a color camera was utilized, the quality of the PSP and TSP data suffered greatly due to the need for adequate emission signals in both channels at all operating conditions while also not maxing out the pixel intensity. Additionally, it was found that a typical Bayer RGB color camera filter did not adequately separate the green and red emission signals.

References

- 1 Tourtellotte, J., "A CBP Air Unit UH-60 Blackhawk Helicopter," <http://www.cbp.gov/xp/cgov/newsroom/multimedia/photo_gallery/afc/cbp_air_marine/amo_11.xml>. Accessed 12/01/2011.
- 2 Vlsergey, "Kamov Ka-52 Alligator," <http://en.wikipedia.org.proxy.lib.ohio-state.edu/wiki/File:Ka-52_at_MAKS-2009.jpg>. Accessed 12/01/2011.
- 3 Sheridan, J., "Fastest Helicopter in the World?" <<http://uavhelicopters.wordpress.com.proxy.lib.ohio-state.edu/>>. Accessed 12/01/2011.
- 4 McCroskey, W.J., "Unsteady Airfoils," *Annual Review of Fluid Mechanics*, Vol. 14, 1982, pp. 285-311.
- 5 McAlister, K.W., Pucci, S.L., McCroskey, W.J., and Carr, L.W., "An Experimental Study of Dynamic Stall on Advanced Airfoil Sections: Volumn 2. Pressure and Force Data," National Aeronautics and Space Administration, NASA-TM-84245, September, 1982.
- 6 Carr, L.W., McCroskey, W.J., McAlister, K.W., Pucci, S.L., and Lambert, O., "An Experimental Study of Dynamic Stall on Advanced Airfoil Sections: Volumn 3. Hot-Wire and Hot-Film Measurements," National Aeronautics and Space Administration, NASA-TM-84245, December, 1982.
- 7 McCroskey, W.J., McAlister, K.W., Carr, L.W., and Pucci, S.L., "An Experimental Study of Dynamic Stall on Advanced Airfoil Sections: Volumn 1. Summary of the Experiment," National Aeronautics and Space Administration, NASA-TM-84245, July, 1982.
- 8 Tijdeman, H., and Seebass, R., "Transonic Flow Past Oscillating Airfoils," *Annual Review of Fluid Mechanics*, Vol. 12, 1980, pp. 181-222.
- 9 Favier, D., Agnes, A., and Maresca, C., "Combined Translation/Pitch Motion: A New Airfoil Dynamic Stall Simulation," *Journal of Aircraft*, Vol. 25, No. 9, 1988, pp. 805-814.

- 10 Favier, D., Rebont, J., and Maresca, C., "Large-Amplitude Fluctuations of Velocity and Incidence of an Oscillating Airfoil," *AIAA Journal*, Vol. 17, 1979, pp. 1265-1267.
- 11 Maresca, C., Favier, D., and Rebont, J., "Experiments on an Aerofoil at High Angle of Incidence in Longitudinal Oscillations," *Journal of Fluid Mechanics*, Vol. 92, No. 4, 1979, pp. 671-690.
- 12 Saxena, L.S. "An Experimental Investigation of Oscillating Flows Over an Airfoil," Ph. D. Thesis, Illinois Institute of Technology, 1977.
- 13 Selerowicz, W.C., and Szumowski, A.P., "Airfoil flow instabilities induced by background flow oscillations," *Experiments in Fluids*, Vol. 32, 2002, pp. 441-446.
- 14 Szumowski, A.P., and Meier, G.E.A., "Forced oscillations of airfoil flows," *Experiments in Fluids*, Vol. 21, 1996, pp. 457-464.
- 15 Babinsky, H., and Fernie, R.M., "NACA0012 Aerofoil in an Oscillating Freestream," *40th AIAA Aerospace Sciences Meeting & Exhibit*, AIAA-2002-0115, American Institute of Aeronautics & Astronautics, Reno, NV, 2002
- 16 Fernie, R.M., and Babinsky, H., "Unsteady Shock Behaviour on a NACA0012 Aerofoil," *41st Aerospace Sciences Meeting and Exhibit*, AIAA 2003-226, American Institute of Aeronautics and Astronautics, Reno, Nevada, 2003
- 17 Fernie, R.M., and Babinsky, H., "Unsteady Shock Motion on a NACA0012 Aerofoil at Low Reduced Frequencies," *42nd AIAA Aerospace Sciences Meeting and Exhibit*, AIAA 2004-49, American Institute of Aeronautics and Astronautics, Reno, Nevada, 2004
- 18 Fernie, R.M., "Low Frequency Shock Motion on a NACA 0012 Aerofoil," *Kings College University of Cambridge, Doctor of Philosophy*, 2004
- 19 Bruce, P.J.K., Babinsky, H., Tartinville, B., and Hirsch, C., "Experimental and Numerical Study of Oscillating Transonic Shock Waves in Ducts," *AIAA Journal*, Vol. 49, No. 8, 2011, pp. 1710-1720.
- 20 Lee, B.K.H., "Oscillatory Shock Motion Caused by Transonic Shock Boundary-Layer Interaction," *AIAA Journal*, Vol. 28, 1990, pp. 942-944.
- 21 Crouch, J.D., Garbaruk, A., Magidov, D., and Travin, A., "Origin of Transonic Buffet on Aerofoils," *Journal of Fluid Mechanics*, Vol. 628, 2009, pp. 357-369.

- 22 Babinsky, H., "Visualisation of shock wave flowfields for comparison of experiment and CFD," *Symposium on Interdisciplinary Shock Wave Research*, Cambridge University, Engineering Department, Sendai, Japan, 2004
- 23 Shih, C., and Ho, C., "Vorticity balance and time scales of a two-dimensional airfoil in an unsteady free stream," *Physics of Fluids*, Vol. 6, No. 2, 1994, pp. 710-723.
- 24 Al-Asmi, K., and Castro, I.P., "Production of oscillatory flow in wind tunnels," *Experiments in Fluids*, Vol. 15, 1993, pp. 33-41.
- 25 Bur, R., Benay, R., Galli, A., and Berthouze, P., "Experimental and Numerical Study of Forced Shock-Wave Oscillations in a Transonic Channel," *Aerospace Science and Technology*, Vol. 10, 2006, pp. 265-278.
- 26 Nowinski, M. "Experimental Investigation of an Oscillating Airfoil in the Presence of Downstream-Generated Aerodynamic Gusts," Thesis de Génie Mécanique, École Polytechnique Fédérale de Lausanne, 1999.
- 27 Lee, J.D., Gregorek, G.M., and Korcan, K.D., "Testing Techniques and Interference Evaluation in the OSU Transonic Airfoil Facility," *American Institute of Aeronautics and Astronautics, 11th Fluid and Plasma Dynamics Conference*, AIAA 1978-1118, 1978
- 28 Gregorek, G.M., Hoffman, M.J., and Berchak, M.J., "Steady State and Oscillatory Aerodynamic Characteristics of a NACA 0015 Airfoil," Aeronautical and Astronautical Research Laboratory, The Ohio State University, Columbus, Ohio, 1989.
- 29 Gompertz, K., Kumar, P., Jensen, C.D., Peng, D., Gregory, J.W., and Bons, J.P., "Modification of a Transonic Blowdown Wind Tunnel to Produce Oscillating Freestream Mach Number," *48th AIAA Aerospace Sciences Meeting including the New Horizons Forum and Aerospace Exposition*, AIAA 2010-1484, American Institute of Aeronautics and Astronautics, 2010
- 30 Petrie, S.L., and Davis, J.A., "Unsteady Transonic Aerodynamics," *Symposium on Airfoils and Aviation, Proceedings of the Annual Conference for Engineers*, Department of Aeronautical and Astronautical Engineering, The Ohio State University,
- 31 Leishman, J.G., "Principles of Helicopter Aerodynamics," Cambridge University Press, 2006.
- 32 Gompertz, K.A., Jensen, C.D., Gregory, J.W., and Bons, J.P., "Compressible Dynamic Stall Mechanisms Due to Airfoil Pitching and Freestream Mach Oscillations," *68th*

American Helicopter Society Annual Forum & Technology Display, American Helicopter Society, Fort Worth, Texas, 2012

- 33 Gompertz, K., Jensen, C.D., Kumar, P., Peng, D., Gregory, J.W., and Bons, J.P., "Modification of Transonic Blowdown Wind Tunnel to Produce Oscillating Freestream Mach Number," *AIAA Journal*, Vol. 49, No. 11, 2011, pp. 2555-2580.
- 34 Liu, T., and Sullivan, J.P., "Pressure and Temperature Sensitive Paints," Springer, New York, 2005.
- 35 Bell, J.H., "Accuracy Limitations of Lifetime-Based Pressure-Sensitive Paint (PSP) Measurements," *19th International Congress on Instrumentation in Aerospace Simulation Facilities*, doi: 10.1109/ICIASF.2001.960231, Institute of Electrical and Electronics Engineers, 2001, pp. 5-16.
- 36 Bell, J.H., Schairer, E.T., Hand, L.A., and Mehta, R.D., "Surface Pressure Measurements Using Luminescent Coatings," *Annual Review of Fluid Mechanics*, Vol. 33, 2001, pp. 155-206.
- 37 Goss, L., Jones, G., Crafton, J., and Fonov, S., "Temperature Compensation in Time-Resolved Pressure Measurements," *International Symposium of Flow Visualization*, 2004
- 38 Goss, L., Jones, G., Crafton, J., and Fonov, S., "Temperature Compensation for Temporal (Lifetime) Pressure Sensitive Paint Measurements," *43rd Aerospace Sciences Meeting and Exhibit*, AIAA-2005-1027, American Institute of Aeronautics and Astronautics, 2005
- 39 Goss, L., Trump, D., Sarka, B., Lydick, L., and Baker, W., "Multi-Dimensional Time-Resolved Pressure-Sensitive Paint Techniques: A Numerical and Experimental Comparison," *37th Aerospace Sciences Meeting and Exhibit*, AIAA-2000-0832, American Institute of Aeronautics and Astronautics, 2000
- 40 Kumar, P. "Development of a Single-Shot Lifetime PSP Measurement Technique for Rotating Surfaces," M.S. Thesis, The Ohio State University, 2010.
- 41 Jensen, C.D., Gompertz, K., Peng, D., Juliano, T.J., Kumar, P., Gregory, J.W., and Bons, J.P., "Unsteady Compressible Flow on a NACA 0021 Airfoil," *49th AIAA Aerospace Sciences Meeting including the New Horizons Forum and Aerospace Exposition*, AIAA 2011-670, American Institute of Aeronautics and Astronautics, 2011
- 42 Scroggin, A.M., Slamovich, E.B., Crafton, J.W., Lachendo, N., and Sullivan, J.P., "Porous Polymer/Ceramic Composites for Luminescent-Based Temperature and

- Pressure Measurement," *Material Research Society Proceedings*, Vol. 560, 1999, pp. 347-352.
- 43 Gregory, J.W., "Porous Pressure-Sensitive Paint for Measurement of Unsteady Pressures in Turbomachinery," *42nd AIAA Aerospace Sciences Meeting and Exhibit*, AIAA 2004-0294, American Institute of Aeronautics and Astronautics, Reno, NV, 2004
- 44 Gregory, J.W., Asai, K., Kameda, M., Liu, T., and Sullivan, J.P., "A Review of Pressure-Sensitive Paint for High-Speed and Unsteady Aerodynamics," *Proceedings of the Institution of Mechanical Engineers, Part G: Journal of Aerospace Engineering*, Vol. 222, No. 2, 2008, pp. 249-290.
- 45 Fang, S., Disotell, K.J., Long, S.R., Gregory, J.W., Semmelmayr, F.C., and Guyton, R.W., "Application of fast-responding pressure-sensitive paint to a hemispherical dome in unsteady transonic flow," *Experiment in Fluids*, Vol. 50, No. 6, 2011
- 46 Peng, D., Gregory, J.W., Crafton, J., and Fonov, S., "Development of a Two Layer Dual-Luminophore Pressure Sensitive Paint for Unsteady Pressure Measurements," *27th AIAA Aerodynamic Measurement Technology and Ground Testing Conference*, AIAA 2010-4918, American Institute of Aeronautics and Astronautics, 2010
- 47 Peng, D., Jensen, C.D., Juliano, T.J., Gregory, J.W., Crafton, J.W., and Palluconi, S., "Temperature-Compensated Fast Pressure-Sensitive Paint," *50th AIAA Aerospace Sciences Meeting including the New Horizons Forum and Aerospace Exposition*, AIAA 2011-1186, American Institute of Aeronautics and Astronautics, 2012
- 48 Gompertz, K. A., Private Communications
- 49 Hollander, M., and Wolfe, D.A., "Nonparametric Statistical Methods," John Wiley & Sons, Inc., New York, 1999.
- 50 Anderson, J.D., "Fundamentals of Aerodynamics," McGraw-Hill, New York, 2007.
- 51 Ladson, C., Hill, A.S., and Johnson, W.G.J., "Pressure Distributions from High Reynolds Number Transonic Tests of an NACA 0012 Airfoil in the Langley 0.3-Meter Transonic Cryogenic Tunnel," *NASA Technical Memorandum 100526*, 1987
- 52 Ladson, C., and Hill, A.S., "High Reynolds Number Transonic Tests of an NACA 0012 Airfoil in the Langley 0.3-Meter Transonic Cryogenic Tunnel," *NASA Technical Memorandum 100527*, 1987

Appendix A: Data Acquisition Post Processing Code

```
%% Initialize Code
clc
close all
clear all
tic
for run=2%:28;
    Chord=0.127;% meters
    freqE=4000;% DAQ board frequency
    %% ATM
    Pa=[102400 102400 102400 102400 102400 102400 102400 102400 102400
102400 102300 102300 102300 102300 102300 102300 102300 102300 102300 102200
102200 102200 102200 102200 102200 102200 102300 102300 102300 ];% [Pa]
    Freq=[0 0 2.1 9.5 15.25 21 0 9.5 9.5 2.1 15.25 21 0 21 2.1 9.5
15.25 0 9.5 2.1 15.25 21 0 2.1 9.5 15.25 21 0]; % [Hz]
    ImageE=[0 100 59 59 59 59 100 59 59 59 59 59 100 59 59 59 59 100 59
59 59 59 100 59 59 59 59 100 0 0 0 0]; % Number of images per run
    Pa=Pa.*0.000145037738; % Pa to psi
    %% Import Data
    Patm=Pa(run);
    Pressure=importdata(strcat('\Run',int2str(run),'Pressure.txt'));
    Pressure=Pressure.data+Patm;
    Encoder=importdata(strcat('\Run',int2str(run),'Encoder.txt'));
    Encoder=Encoder.data;
    le=length(Encoder); lp=length(Pressure);
    %% Calculate the thermistor temperatures
    Vg1=Encoder(:,4);
    Vg2=Encoder(:,5);
    R1=wheatstone(47000,47000,27000,24,Vg1);
    T1 = 605.*R1.^(-0.1266)-154.2;
    R2=wheatstone(47000,47000,27000,24,Vg2);
    T2 = 605.*R2.^(-0.1266)-154.2;
    %% Name the encoder data and apply calibrations to the data
    po=Encoder(1:le,1).*9.98-.0266; ps=Encoder(1:le,2)*5.0442-0.1;
    [mpo,sI] = max(po);
    ze=Encoder(1:le,10); ae=Encoder(1:le,9); Shutter1=Encoder(1:le,6);
    Trig=Encoder(1:le,7);
    To=Encoder(1:le,8); Shutter2=Encoder(1:le,3);
    Et=(1:length(po))./freqE;
    x=1:le;
    %% low pass filter pressures
    [b,a] = cheby2(1,25,.5); % create filter
    po = filtfilt(b,a,po); % filter the total and static pressures
    ps = filtfilt(b,a,ps);
    %% calculate the phase shift for the unsteady Mach oscillation runs
    if Freq(run)==0
```

```

else
    [b,a] = cheby2(2,35,.06); % create filter
    pof = filtfilt(b,a,po); % use filter on Po and Ps
    psf = filtfilt(b,a,ps);
    nnn=3;
    tx=-1*(ceil(nnn/Freq(run)*freqE)):ceil(nnn/Freq(run)*freqE);

shifter=xcov(pof(sI:sI+ceil(nnn/Freq(run)*freqE)),psf(sI:sI+ceil(nnn/Freq(run)*freqE)));
    [mx,ix] = max(shifter);
    lag = tx(ix);
    po=circshift(po,-lag);
end
% add in the shift for the distance between the Ps and test section
po=circshift(po,-7); ps=circshift(ps,-7);
m=real(sqrt(5*((po./ps).^(2/7)-1)));% calculate Mach number
dm=(m-circshift(m,1))*4000;% calculate the rate of change of M
%% Calculate the time stamp for the pressure brick data
Pt=Pressure(1:lp,1)./1000;
Po=Pressure(1:lp,2); % total pressure
Ps=(Pressure(1:lp,3)+Pressure(1:lp,4))./2; % average for static
pressure
M=sqrt(5*((Po./Ps).^(2/7)-1)); M=real(M);% calculate mach number
from pressures
%% Calculate the angular encoder data from the once per rev signal
(ze)
% and 500 per rev signal (ae)
dze=ze-circshift(ze,1);dze(1)=0;
dae=ae-circshift(ae,1);dae(1)=0;
pulse=find(dze);
lpulse=length(pulse);
angle=zeros(size(ae));
for i=1:lpulse-1;
    angle(pulse(i):pulse(i+1)-1)=cumsum(dae(pulse(i):pulse(i+1)-1));
end
angle=angle.*360./250;% convert the signal to degrees
sse=find(m(pulse)>0.4,1,'first')
see=find(m(pulse)>0.4,1,'last')
mangle=0;
for i=1:see-sse-1
    [C,I1(i)]=max(m(pulse(sse+1):(pulse(sse+2)-pulse(sse+1))/2+pulse(sse+1)));
    mLi=pulse(sse+1)+I1(i);
    mangle(i)=angle(mLi);
end
shifter=median(mangle)-90
asmuth=angle-shifter;
lowasmuth=(asmuth < 0)*360;
highasmuth2=(asmuth > 360)*360;
asmuth=asmuth+lowasmuth-highasmuth2;
%% find camera pulses
cam=Shutter1>1;
Cs=(cam>0) & (circshift(cam,1)==0);
Ce=(cam==0) & (circshift(cam,1)>0);

```

```

numb=length(find(Ce));
eind(1:numb,1)=find(Cs);
length(find(Cs));
eind(1:numb,2)=find(Ce);
TimeS(1:numb)=Et(eind(1:numb,1));
TimeE(1:numb)=Et(eind(1:numb,2));
tleng=TimeE.*1000-TimeS.*1000;
Angle(1:numb,1)=angle(eind(:,1));
%% Caculate the velocity from Mach number
[b,a] = cheby2(1,50,.2);
To = filtfilt(b,a,To);
To=(To+273.1);%degK
R=287.1;
aa=(sqrt(1.4.*R.*To));
vel=m.*aa;
%% Find pressure index corisponding to camera pulse time stamp
for i=1:length(Times)
    pind(i,1)=find(Pt>TimeS(i),1);
    pind(i,2)=find(Pt>TimeE(i),1);
end
Cp=zeros(size(Pressure(1:lp,5:15)));
g=1.4;
for i=1:11
    Cp(:,i)=2.*(Pressure(:,i+4)-Ps(:,1))./(g.*M(:,1).*Ps(:,1));
end
toc
row=po./0.000145037738./(To)./R;
visc=1.458E-6.*To.^1.5./(110.4+To);
Re=0.127.*vel.*row./visc;
image=1:length(pind);
for i=1:length(pind)
    mOut(i)=median(m(eind(i,1):(eind(i,2))));
    dmOut(i)=median(dm(eind(i,1):(eind(i,2))));
    ToOut(i)=median(To(eind(i,1):(eind(i,2))));
    poOut(i)=median(po(eind(i,1):(eind(i,2))));
    psOut(i)=median(ps(eind(i,1):(eind(i,2))));
    EtOut(i)=median(Et(eind(i,1):(eind(i,2))));
    AngleOut(i)=median(angle(eind(i,1):(eind(i,2))));
    T1Out(i)=median(T1(eind(i,1):(eind(i,2))));
    T2Out(i)=median(T2(eind(i,1):(eind(i,2))));
    Shutter2Out(i)=median(Shutter2(eind(i,1):(eind(i,2))));
    asmuthOut(i)=median(asmuth(eind(i,1):(eind(i,2))));
    ReOut(i)=median(Re(eind(i,1):(eind(i,2))));
end
Pdata(1,:)={'Image','05','10','15','25','30','35','40','50','70','90','
-10','-50','Mach','To','Po','Ps','Time','Ang','T20','T85','2',
'dMach','asmuth'};
Pdata(2:numb+1,:)=[image' Pressure(pind(:,1),5:16) mOut' ToOut'
poOut' psOut' EtOut' AngleOut' T1Out' T2Out' Shutter2Out' dmOut'
asmuthOut' ReOut'];
xlswrite((strcat('Run',int2str(run),'PressureData')), Pdata)

PdataNames(1,:)={'Image','05','10','15','25','30','35','40','50','70','
90','-10','-'}

```

```

50', 'Mach', 'To', 'Po', 'Ps', 'Time', 'Ang', 'T20', 'T85', '2', 'dMach', 'asmuth'
, 'Re'}];
    xlswrite((strcat('Run',int2str(run),'PressureData')), PdataNames)
    pmean=[1 19 20 39 40 59];

Pmean12(1,:)= [mean(Pressure(pind(pmean(1),1):pind(pmean(2),1),5:16))
mean(m(eind(pmean(1),1):(eind(pmean(2),2))))
mean(To(eind(pmean(1),1):(eind(pmean(2),2))))
mean(po(eind(pmean(1),1):(eind(pmean(2),2))))
mean(ps(eind(pmean(1),1):(eind(pmean(2),2))))
mean(T1(eind(pmean(1),1):(eind(pmean(2),2))))
mean(T2(eind(pmean(1),1):(eind(pmean(2),2))))];

Pmean12(2,:)= [mean(Pressure(pind(pmean(3),1):pind(pmean(4),1),5:16))
mean(m(eind(pmean(3),1):(eind(pmean(4),2))))
mean(To(eind(pmean(3),1):(eind(pmean(4),2))))
mean(po(eind(pmean(3),1):(eind(pmean(4),2))))
mean(ps(eind(pmean(3),1):(eind(pmean(4),2))))
mean(T1(eind(pmean(3),1):(eind(pmean(4),2))))
mean(T2(eind(pmean(3),1):(eind(pmean(4),2))))];

Pmean12(3,:)= [mean(Pressure(pind(pmean(5),1):pind(pmean(6),1),5:16))
mean(m(eind(pmean(5),1):(eind(pmean(6),2))))
mean(To(eind(pmean(5),1):(eind(pmean(6),2))))
mean(po(eind(pmean(5),1):(eind(pmean(6),2))))
mean(ps(eind(pmean(5),1):(eind(pmean(6),2))))
mean(T1(eind(pmean(5),1):(eind(pmean(6),2))))
mean(T2(eind(pmean(5),1):(eind(pmean(6),2))))];
    save(['Run' int2str(run) '\Pmean12.mat'], 'Pmean12');
clear all
end

```

Appendix B: Image Registration Code

```

%% Start
clc
close all
clear all%
tic
%% for looping
for dateN= 1:2
    %% pick a date
    if dateN==1
        date='11.21.11'; runS=2; runE=28;
    else
        date='11.23.11'; runS=1; runE=32;
    end
    %% for looping
    for run=runS:runE
        %% Number of images per run
        ImageE=[0 100 59 59 59 59 100 59 59 59 59 100 59 59 59 59
100 59 59 59 59 100 59 59 59 59 100 0 0 0 0;100 59 59 59 59 59 100 59
59 59 59 100 500 500 500 500 500 500 50 50 50 50 50 50 50 50 50
50 50 50];
        disp([date ' Run ' int2str(run)])
        %% for looping
        for image=1:ImageE(dateN,run);%
            %% initialize
            Buffer=6;
            load PSPcolormap;
            fontsize = 13;
            if date=='11.21.11'
                A=[9 9 9 9 9 9 4.5 4.5 10 10 10 10 10 0 0 0 0 0 -9 -9 -
9 -9 -9 -10 -10 -10 -10];
                Freq=[0 0 2.1 9.5 15.25 21 0 9.5 9.5 2.1 15.25 21 0 21
2.1 9.5 15.25 0 9.5 2.1 15.25 21 0 2.1 9.5 15.25 21 0];
                Pa=[102400 102400 102400 102400 102400 102400 102400
102400 102400 102400 102300 102300 102300 102300 102300 102300 102300
102300 102200 102200 102200 102200 102200 102200 102200 102300 102300
102300];%Pa
                Ta=[7.2 7.2 7.2 7.2 7.2 7.2 7.2 7.2 7.2 7.2 7.2 7.8 7.8 7.8
7.8 7.8 7.8 7.8 7.8 7 7 7 7 7.2 7.2 7.2];%deg C
                Pa=Pa.*0.000145037738; %Pa to psi
            else
                A=[-4.5 -4.5 -11 -11 -11 -11 -11 11 11 11 11 11 11 11
10 10 9 9 9 10 11 -11 -10 -9 0 0 9 10 11 -11 -10 -9];
                Freq=[0 9.5 2.1 9.5 15.25 21 0 2.1 9.5 15.25 21 0 2 9.5
9.5 2 2 9.5 0 0 0 0 0 0 0 0 0 0 0 0];
            end
        end
    end
end

```

```

Pa=[101800 101800 101800 101800 101900 101900 101900
101900 101900 101900 101900 101900 101900 101900 101900 101900 101900
101900 102000 102000 102000 102000 102000 102000 102000 102000 102000
102000 102000 102000 102000 102100];%Pa
Ta=[5 5 5 5 6.1 6.1 6.1 6.1 6.7 6.7 6.7 8 8 8 8 8 8 9.4
9.4 9.4 9.4 10 10 10 10 10 10 10 10 10 8.9];%deg C
Pa=Pa.*0.000145037738; %Pa to psi
end
%% Importing the pressure data
Ai=A(run);

data=importdata([date,'\Run',int2str(run),'PressureData.xls']);
Pdata=data.data.Sheet1;
%% Import images
if image<10
    darkG = double(imread([date,'\Run',int2str(run),
'\Dark_000',int2str(image),'.tif']));
    onG    = double(imread([date,'\Run',int2str(run),
'\WindOn_000',int2str(image),'.tif']));
    offG   = double(imread([date,'\Run',int2str(run),
'\WindOff_000',int2str(image),'.tif']));
    darkR = double(imread([date,'\Run',int2str(run),
'Red\Dark_000',int2str(image),'.tif']));
    onR    = double(imread([date,'\Run',int2str(run),
'Red\WindOn_000',int2str(image),'.tif']));
    offR   =
double(imread([date,'\Run',int2str(run),'Red\WindOff_000',int2str(image)
, '.tif']));
elseif image<100
    darkG = double(imread([date,'\Run',int2str(run),
'\Dark_00',int2str(image),'.tif']));
    onG    = double(imread([date,'\Run',int2str(run),
'\WindOn_00',int2str(image),'.tif']));
    offG   = double(imread([date,'\Run',int2str(run),
'\WindOff_00',int2str(image),'.tif']));
    darkR = double(imread([date,'\Run',int2str(run),
'Red\Dark_00',int2str(image),'.tif']));
    onR    = double(imread([date,'\Run',int2str(run),
'Red\WindOn_00',int2str(image),'.tif']));
    offR   =
double(imread([date,'\Run',int2str(run),'Red\WindOff_00',int2str(image)
, '.tif']));
else
    darkG = double(imread([date,'\Run',int2str(run),
'\Dark_0',int2str(image),'.tif']));
    onG    = double(imread([date,'\Run',int2str(run),
'\WindOn_0',int2str(image),'.tif']));
    offG   = double(imread([date,'\Run',int2str(run),
'\WindOff_0',int2str(image),'.tif']));
    darkR = double(imread([date,'\Run',int2str(run),
'Red\Dark_0',int2str(image),'.tif']));
    onR    = double(imread([date,'\Run',int2str(run),
'Red\WindOn_0',int2str(image),'.tif']));

```

```

        offR =
double(imread([date, '\Run', int2str(run), 'Red\WindOff_0', int2str(image),
'.tif']));
end
%% dark correction and Resize to 600 x 800 pixels
onR=(onR-darkR);
offR=(offR-darkR);clear darkR;
onG=fliplr(onG-darkG);
offG=fliplr(offG-darkG);clear darkG;
onR = imresize(onR, [600 800], 'bilinear');
offR = imresize(offR, [600 800], 'bilinear');
onG = imresize(onG, [600 800], 'bilinear');
offG = imresize(offG, [600 800], 'bilinear');
[m, n] = size(onG);
%% Std and Image Rotation
onRStd=medfilt2(single(stdfilt(onR)));
offRStd=medfilt2(single(stdfilt(offR)));
onGStd=medfilt2(single(stdfilt(onG)));
offGStd=medfilt2(single(stdfilt(offG)));
SNRr=offR./stdfilt(offR);
SNRg=offG./stdfilt(offG);
maskOnG = zeros(m, n);
maskOnG(:, :) = single(onGStd(:, :) < max(max(onGStd))/4);
maskOffG = zeros(m, n);
maskOffG(:, :) = single(offGStd(:, :) <
max(max(offGStd))/4);
offGStd=offGStd.*maskOffG;
onGStd=onGStd.*maskOnG;
var=onRStd;
var=medfilt2(var, [5 5]);

angle(1)=atan((find(var(500, :)>max(var(500, 1:250))*0.9, 1, 'first')-
find(var(100, :))...
>max(var(100, 1:250))*0.9, 1, 'first'))/400);
onR=imrotate(onR, -1*angle(1)*180/pi(), 'bilinear', 'crop');
var=offRStd;
var=medfilt2(var, [5 5]);

angle(2)=atan((find(var(500, :)>max(var(500, 1:250))*0.9, 1, 'first')-
find(var(100, :))...
>max(var(100, 1:250))*0.9, 1, 'first'))/400);
offR=imrotate(offR, -1*angle(1)*180/pi(), 'bilinear', 'crop');
var=onGStd;
var=medfilt2(var, [5 5]);

angle(3)=atan((find(var(500, :)>max(var(500, 1:250))*0.9, 1, 'first')-
find(var(100, :))...
>max(var(100, 1:250))*0.9, 1, 'first'))/400);
onG=imrotate(onG, -1*angle(3)*180/pi(), 'bilinear', 'crop');
var=offGStd;
var=medfilt2(var, [5 5]);

angle(4)=atan((find(var(500, :)>max(var(500, 1:250))*0.9, 1, 'first')-
find(var(100, :))...
>max(var(100, 1:250))*0.9, 1, 'first'))/400);

```

```

offG=imrotate(offG,-1*angle(3)*180/pi(),'bilinear','crop');
clear onRStd
clear offRStd
clear onGStd
clear offGStd
clear SNRr
clear SNRg
%% Std with boader cropping
boarder=6; %Std while removing the extra data from the
rotation
onRStd=double(stdfilt(onR(boarder:m-boarder,boarder:n-
boarder)));
offRStd=double(stdfilt(offR(boarder:m-boarder,boarder:n-
boarder)));
onGStd=double(stdfilt(onG(boarder:m-boarder,boarder:n-
boarder)));
offGStd=double(stdfilt(offG(boarder:m-boarder,boarder:n-
boarder)));
offGStd=offGStd(1:530,:);
onGStd=onGStd(1:530,:);
offRStd=offRStd(1:530,:);
onRStd=onRStd(1:530,:);
%% Image Registration Translation
if image==1
    refImage= offRStd;
end
% Red off registration
[registration Shift] = dftregistration(fft2(refImage),
fft2(onRStd), 1);
shift(1:2) = registration(3:4);
onR = circshift(onR,shift);

% Red off registration
[registration Shift] = dftregistration(fft2(refImage),
fft2(offRStd), 1);
shift(1:2) = registration(3:4);
offR = circshift(offR,shift);

% Green On registration
[registration Shift] = dftregistration(fft2(refImage),
fft2(onGStd), 1);
shift(1:2) = registration(3:4);
onG = circshift(onG,shift);
% Green Off registration
[registration Shift] = dftregistration(fft2(refImage),
fft2(offGStd), 1);
shift(1:2) = registration(3:4);
offG = circshift(offG,shift);
clear onRStd
clear offRStd
clear onGStd
clear offGStd
%% RatioG + R
RatioR=onR./offR;

```

```

RatioG=(onG./offG);
%% Masking the background of the image
mask = zeros(m, n);
mask(:, :) = single(onR(:, :) > max(max(onR))*0.08);
mask = imresize(mask, [600 800], 'bilinear');
%% Find leading and trailing edges
lead = find(mask(250, :)>.5, 1, 'first');
trail = find(mask(250, :)>.5, 1, 'last');
%% Boarder Cropping using Buffer
RatioR=RatioR(Buffer+15:m-Buffer, lead:trail);
RatioG=RatioG(Buffer+15:m-Buffer, lead:trail);
%% file saving
save([date, '\Run' int2str(run) '\Image' int2str(image)
'RatioR.mat'], 'RatioRmf');
save([date, '\Run' int2str(run) '\Image' int2str(image)
'RatioG.mat'], 'RatioGmf');
    end
    toc
end
end
end

```

Appendix C: Averaging Ratio of Red and Green Code

```
%% Start
clc
clear all%
tic
for dateN=1
    if dateN==1
        %% for looping
        date='11.21.11'; runS=2; runE=28;
        ImageE=[0 100 59 59 59 59 100 59 59 59 59 59 100 59 59 59 59
100 59 59 59 59 100 59 59 59 59 100 0 0 0 0];
    else
        %% for looping
        date='11.23.11'; runS=19; runE=32;
        ImageE=[100 59 59 59 59 59 100 59 59 59 59 100 500 500 500 500
500 500 50 50 50 50 50 50 50 50 50 50 50 50];
    end
    for run=runS:runE
        MeanRatioR1=zeros(574,514);
        MeanRatioG1=zeros(574,514);
        MeanRatioR2=zeros(574,514);
        MeanRatioG2=zeros(574,514);
        MeanRatioR3=zeros(574,514);
        MeanRatioG3=zeros(574,514);
        Mask=ones(574,514);
        for image=1:ImageE(run);
            load([date, '\Run' int2str(run) '\Image' int2str(image)
'RatioR.mat']);
            load([date, '\Run' int2str(run) '\Image' int2str(image)
'RatioG.mat']);
            RatioR = imresize(RatioR, [574 514], 'bilinear');
            RatioG = imresize(RatioG, [574 514], 'bilinear');
            RatioGg= medfilt2(RatioG, [50 30]);
            GItherm(1, image)=RatioGg(564,111);
            GItherm(2, image)=RatioGg(553,445);
            i=0; j=0; k=0;
            if image<20
                i=i+1;
                MeanRatioR1=MeanRatioR1+RatioR;
                MeanRatioG1=MeanRatioG1+RatioG;
            elseif image<40
                j=j+1;
                MeanRatioR2=MeanRatioR2+RatioR;
                MeanRatioG2=MeanRatioG2+RatioG;
            elseif image<60
                k=k+1;
```

```

        MeanRatioR3=MeanRatioR3+RatioR;
        MeanRatioG3=MeanRatioG3+RatioG;
    else
    end
    RatioRstd=medfilt2(single(stdfilt(RatioR)));
    SNRr=RatioR./RatioRstd;
    SNRr= medfilt2(SNRr,[45 30]);
    MaskI=SNRr>25;
    Mask=Mask.*MaskI;
end
MeanRatioR1=MeanRatioR1./i;
MeanRatioG1=MeanRatioG1./i;
MeanRatioR2=MeanRatioR2./j;
MeanRatioG2=MeanRatioG2./j;
MeanRatioR3=MeanRatioR3./k;
MeanRatioG3=MeanRatioG3./k;
save([date, '\Run' int2str(run) '\Mask.mat'], 'Mask');
save([date, '\Run' int2str(run) '\MeanRatioR1.mat'],
'MeanRatioR1');
save([date, '\Run' int2str(run) '\MeanRatioG1.mat'],
'MeanRatioG1');
save([date, '\Run' int2str(run) '\MeanRatioR2.mat'],
'MeanRatioR2');
save([date, '\Run' int2str(run) '\MeanRatioG2.mat'],
'MeanRatioG2');
save([date, '\Run' int2str(run) '\MeanRatioR3.mat'],
'MeanRatioR3');
save([date, '\Run' int2str(run) '\MeanRatioG3.mat'],
'MeanRatioG3');
save([date, '\Run' int2str(run) '\GItherm.mat'], 'GItherm');
toc
end

```

Appendix D: *In situ* Calibration and Implementation Code

```
%% Start
clc
close all
clear all%
tic
font_size=14;
line_width=2;
set(0,'DefaultAxesBox','on','DefaultAxesLineWidth',line_width,'DefaultAxesFontSize',font_size);
set(0,'DefaultLineLineWidth',line_width);
%% for loop that
for dateN=1
    if dateN==1
        %% for looping
        date='11.21.11'; runS=2; runE=28;
        Pa=[102400 102400 102400 102400 102400 102400 102400 102400
102400 102400 102300 102300 102300 102300 102300 102300 102300 102300
102200 102200 102200 102200 102200 102200 102200 102300 102300 102300
];%Pa
        Ta=[7.2 7.2 7.2 7.2 7.2 7.2 7.2 7.2 7.2 7.2 7.2 7.8 7.8 7.8 7.8 7.8
7.8 7.8 7.8 7.8 7.8 7 7 7 7 7.2 7.2 7.2];%deg C
        Pa=Pa.*0.000145037738; %Pa to psi
        A=[9 9 9 9 9 9 4.5 4.5 10 10 10 10 10 0 0 0 0 0 -9 -9 -9 -9 -9
-10 -10 -10 -10 -10];
    else
        %% for looping
        date='11.23.11'; runE=32; runs=[24];
        Pa=[101800 101800 101800 101800 101900 101900 101900 101900
101900 101900 101900 101900 101900 101900 101900 101900 101900 101900
102000 102000 102000 102000 102000 102000 102000 102000 102000 102000
102000 102000 102000 102100];%Pa
        Ta=[5 5 5 5 6.1 6.1 6.1 6.1 6.7 6.7 6.7 8 8 8 8 8 8 9.4 9.4 9.4
9.4 10 10 10 10 10 10 10 10 10 10 8.9];%deg C
        Pa=Pa.*0.000145037738; %Pa to psi
        A=[-4.5 -4.5 -11 -11 -11 -11 -11 11 11 11 11 11 11 11 10 10 9 9
9 10 11 -11 -10 -9 0 0 9 10 11 -11 -10 -9];
    end
    for run=runs;%runS:runE
        %% Pressure Data importing and naming
        ImageE=[0 100 59 59 59 59 100 59 59 59 59 100 59 59 59 59
100 59 59 59 100 59 59 59 59 100 0 0 0 0;100 59 59 59 59 59 100 59
59 59 59 100 500 500 500 500 500 500 50 50 50 50 50 50 50 50 50
50 50 50];
        image=1:ImageE(dateN,run);
        data=importdata([date,'\Run',int2str(run),'PressureData.xls']);
    end
end
```

```

Pdata=data.data.Sheet1;
M =Pdata(image+1,14);
Patm=Pa(run);
po =Pdata(image+1,16);
ps = Pdata(image+1,17);
%% calibration mean ratios
load([date, '\Run' int2str(run) '\MeanRatioR1.mat'])
load([date, '\Run' int2str(run) '\MeanRatioG1.mat']);
MeanRatioG1 = imresize(MeanRatioG1, [574 514], 'bilinear');
MeanRatioR1 = imresize(MeanRatioR1, [574 514], 'bilinear');
MeanRatioR1= medfilt2(MeanRatioR1,[50 30]);
MeanRatioG1= medfilt2(MeanRatioG1,[50 30]);

load([date, '\Run' int2str(run) '\MeanRatioR2.mat'])
load([date, '\Run' int2str(run) '\MeanRatioG2.mat']);
MeanRatioG2 = imresize(MeanRatioG2, [574 514], 'bilinear');
MeanRatioR2 = imresize(MeanRatioR2, [574 514], 'bilinear');
MeanRatioR2= medfilt2(MeanRatioR2,[50 30]);
MeanRatioG2= medfilt2(MeanRatioG2,[50 30]);

load([date, '\Run' int2str(run) '\MeanRatioR3.mat'])
load([date, '\Run' int2str(run) '\MeanRatioG3.mat']);
MeanRatioG3 = imresize(MeanRatioG3, [574 514], 'bilinear');
MeanRatioR3 = imresize(MeanRatioR3, [574 514], 'bilinear');
MeanRatioR3= medfilt2(MeanRatioR3,[50 30]);
MeanRatioG3= medfilt2(MeanRatioG3,[50 30]);

[m n]=size(MeanRatioG3);
%% load in the mean pressures
load([date '\Run' int2str(run) '\Pmean12.mat'])%'Pmean'
ptM=Pmean12(1:3,1:12);
mM=Pmean12(1:3,13);
toM=Pmean12(1:3,14);
poM=Pmean12(1:3,15);
psM=Pmean12(1:3,16);

load([date, '\Run' int2str(run) '\Mask.mat'])
disp([date ' Run ' int2str(run)])
load PSPcolormap;
xoc=(1:n)./n.*100;
%% x and I locations
x(1) = find(xoc>5,1,'first');
x(2) = find(xoc>10,1,'first');
x(3) = find(xoc>15,1,'first');
x(4) = find(xoc>25,1,'first');
x(5) = find(xoc>30,1,'first');
x(6) = find(xoc>35,1,'first');
x(7) = find(xoc>40,1,'first');
x(8) = find(xoc>50,1,'first');
x(9) = find(xoc>70,1,'first');
x(10) = find(xoc>90,1,'first');
z([1:3 5 8:10])=338;
z(4)=283;
z(6)=390;

```

```

z(7)=444;
for i=1:10
    I(i) = mean(MeanRatioR1(z(i),x(i)));
    IT(i)=MeanRatioG1(z(i),x(i));
    I(i+10) = mean(MeanRatioR2(z(i),x(i)));
    IT(i+10)= MeanRatioG2(z(i),x(i));
    I(i+20) = mean(MeanRatioR3(z(i),x(i)));
    IT(i+20)=MeanRatioG3(z(i),x(i));
    Iptap(i)=ptM(1,i);
    Iptap(i+10)=ptM(2,i);
    Iptap(i+20)=ptM(3,i);
end
%% fitting
ft = fittype( 'poly12' );
opts = fitoptions( ft );
[fit25, gof25] = fit( [IT', I'], Iptap', ft, opts );
gof25
fit25
for image=[31 44]%1:ImageE(dateN,run);
    load([date, '\Run' int2str(run) '\Image' int2str(image)
'RatioR.mat']);
    load([date, '\Run' int2str(run) '\Image' int2str(image)
'RatioG.mat']);
    RatioR = imresize(RatioR, [574 514], 'bilinear');
    RatioG = imresize(RatioG, [574 514], 'bilinear');
    RatioGmf= medfilt2(RatioG, [50 30]);
    RatioRmf= medfilt2(RatioR, [50 10]);
    %% full insitu calibration
    Pressure=fit25(RatioGmf,RatioRmf);
    Cp=(Pressure.*Mask./ps(image)-1)./(0.5.*1.4.*M(image).^2);
    xu=[0 xoc(8:495)];
    for i=1:length(Cp(3,:))
        Cp(i)=mean(Cp(325:345,i));
    end
    yu=[-2 Cp
(8:495)];
    CpData(1,:,image)=xu;
    CpData(2,:,image)=yu;
    pdatax=[5 10 15 25 30 35 40 50 70 90];
    CpPt=(pt(image,1:10)./ps(image)-
1)./(0.5.*1.4.*M(image).^2);%.*Mask;
    %% plotting
    figure
    hold on
    plot(xu,yu,'b')
    plot(pdatax,CpPt(1:10),'bs')
    set(gca,'YDir','rev')
    xlabel('Percent x/c')
    ylabel('Cp')
    axis([0 100 -3.75 1.1])
    grid on
    hold off
    toc
    save([date, '\Run' int2str(run) '\Image' int2str(image)
'Cp.mat'], 'Cp');

```

```
end
save([date, '\Run' int2str(run) 'CpData.mat'], 'CpData');
toc
end
end
```

Appendix E: Shock Location Capture Code

```

%% Start
clc
close all
clear all%
tic
for dateN=1:2
    if dateN==1
        %% for looping
        date='11.21.11'; runS=14; runE=28;
        Pa=[102400 102400 102400 102400 102400 102400 102400 102400
102400 102400 102300 102300 102300 102300 102300 102300 102300 102300 102300 102300
102200 102200 102200 102200 102200 102200 102200 102300 102300 102300
];%Pa
        Ta=[7.2 7.2 7.2 7.2 7.2 7.2 7.2 7.2 7.2 7.2 7.2 7.8 7.8 7.8 7.8 7.8
7.8 7.8 7.8 7.8 7.8 7.8 7 7 7 7 7.2 7.2 7.2];%deg C
        Pa=Pa.*0.000145037738; %Pa to psi
    else
        %% for looping
        date='11.23.11'; runS=1; runE=32;
        Pa=[101800 101800 101800 101800 101800 101900 101900 101900 101900
101900 101900 101900 101900 101900 101900 101900 101900 101900 101900 101900
102000 102000 102000 102000 102000 102000 102000 102000 102000 102000 102000
102000 102000 102000 102100];%Pa
        Ta=[5 5 5 5 6.1 6.1 6.1 6.1 6.7 6.7 6.7 8 8 8 8 8 8 9.4 9.4 9.4
9.4 10 10 10 10 10 10 10 10 10 10 8.9];%deg C
        Pa=Pa.*0.000145037738; %Pa to psi
    end
    for run=runS:runE
        ImageE=[0 100 59 59 59 59 100 59 59 59 59 59 100 59 59 59 59
100 59 59 59 59 100 59 59 59 59 100 0 0 0 0;100 59 59 59 59 59 100 59
59 59 59 100 500 500 500 500 500 500 50 50 50 50 50 50 50 50 50
50 50 50];
        disp([date ' Run ' int2str(run)])
        for image=1:ImageE(dateN,run);
            load([date, '\Run' int2str(run) '\Image' int2str(image)
'RatioG.mat']);
            load([date, '\Run' int2str(run) '\Image' int2str(image)
'RatioR.mat']);
            RatioGmf= medfilt2(RatioG,[40 10]);
            RatioRmf= medfilt2(RatioR,[40 10]);
            RatioGcp=RatioG(335,:);clear RatioG
            RatioRcp=RatioR(335,:);clear RatioR
            RatioGcpMf=RatioGmf(335,:);clear RatioGmf
            RatioRcpMf=RatioRmf(335,:);
            RatioRcpMfs(1,:)=RatioRmf(100,:);
        end
    end
end

```

```

RatioRcpMfs(2,:) = RatioRmf(150,:);
RatioRcpMfs(3,:) = RatioRmf(200,:);
RatioRcpMfs(4,:) = RatioRmf(250,:);
RatioRcpMfs(5,:) = RatioRmf(350,:);
RatioRcpMfs(6,:) = RatioRmf(400,:);
RatioRcpMfs(7,:) = RatioRmf(450,:);
[n] = length(RatioGcp);
xoc = (1:n)/n*100;
dRatioRcpMf = RatioRcpMf(:) - circshift(RatioRcpMf(:), 1);
dRatioGcpMf = RatioGcpMf(:) - circshift(RatioGcpMf(:), 1);
[mv ml] = min(dRatioRcpMf(13:floor(n/5)));
SL(image, 1) = xoc(ml+13); %Shock Location for Pressure
[mv ml] = max(dRatioGcpMf(13:floor(n/5)));
SL(image, 2) = xoc(ml+13); %Slock Location for Temperature
for s=1:7
    dRatioRcpMfs(s,:) = RatioRcpMfs(s,:) -
circshift(RatioRcpMfs(s,:)', 1);
    [mv ml] = min(dRatioRcpMfs(s, 13:floor(n/5)));
    SL(image, s+2) = xoc(ml+13);
end
clear dRatioRcpMfs RatioRcpMfs RatioRcpMf RatioGcpMf
end
xlswrite([date '\Run' int2str(run) '\ShockLocation'], SL)
toc
end
end

```

Appendix F: Tabulated C_n , C_a , C_l and C_m Data

Table 4: Coefficient of lift, moment and normal force for the steady runs with two standard deviation shown for each PSP measurement

α	M	C_n	C_a	C_l	C_m
9	0.468 ± 0.004	0.699 ± 0.051	-0.144 ± 0.019	0.713 ± 0.050	0.049 ± 0.098
10	0.450 ± 0.005	1.053 ± 0.076	-0.179 ± 0.027	1.068 ± 0.076	0.027 ± 0.041
11	0.449 ± 0.003	0.923 ± 0.090	-0.205 ± 0.024	0.945 ± 0.091	0.080 ± 0.048
9	0.5 (NASA)	0.862	-0.104	0.868	0.0209
10	0.5 (NASA)	0.913	-0.111	0.918	0.0244
11	0.5 (NASA)	0.91	-0.0995	0.912	0.0179
9	0.549 ± 0.003	0.886 ± 0.018	-0.159 ± 0.006	0.900 ± 0.019	0.029 ± 0.009
10	0.547 ± 0.002	0.888 ± 0.032	-0.165 ± 0.009	0.903 ± 0.032	0.034 ± 0.013
11	0.546 ± 0.002	0.946 ± 0.042	-0.156 ± 0.012	0.959 ± 0.042	0.024 ± 0.022
9	0.609 ± 0.003	0.872 ± 0.022	-0.133 ± 0.008	0.882 ± 0.022	0.015 ± 0.012
10	0.607 ± 0.002	0.849 ± 0.068	-0.126 ± 0.014	0.858 ± 0.067	0.015 ± 0.032
11	0.606 ± 0.002	1.571 ± 0.575	-0.093 ± 0.042	1.560 ± 0.557	-0.208 ± 0.216
9	0.6 (NASA)	0.852	-0.0702	0.852	0.0232
10	0.6 (NASA)	0.852	-0.0517	0.848	-0.0026